9-18-2014

Hyperfine Interactions in the Electron Paramagnetic Resonance Spectra of Point Defects in Wide-Band-Gap Semiconductors

Eric M. Golden

Recommended Citation

Golden, Eric M., "Hyperfine Interactions in the Electron Paramagnetic Resonance Spectra of Point Defects in Wide-Band-Gap Semiconductors" (2014). *Theses and Dissertations*. 546.
https://scholar.afit.edu/etd/546

HYPERFINE INTERACTIONS IN THE ELECTRON PARAMAGNETIC RESONANCE SPECTRA OF POINT DEFECTS IN WIDE-BAND-GAP SEMICONDUCTORS

DISSERTATION

Eric M. Golden, Major, USAF

AFIT-ENP-DS-14-S-07

DEPARTMENT OF THE AIR FORCE
AIR UNIVERSITY

AIR FORCE INSTITUTE OF TECHNOLOGY

Wright-Patterson Air Force Base, Ohio

DISTRIBUTION STATEMENT A.
APPROVED FOR PUBLIC RELEASE; DISTRIBUTION UNLIMITED.

AFIT-ENP-DS-14-S-07

HYPERFINE INTERACTIONS IN THE ELECTRON PARAMAGNETIC RESONANCE SPECTRA OF POINT DEFECTS IN WIDE-BAND-GAP SEMICONDUCTORS

DISSERTATION

Presented to the Faculty
Department of Engineering Physics
Graduate School of Engineering and Management
Air Force Institute of Technology
Air University
Air Education and Training Command
In Partial Fulfillment of the Requirements for the
Degree of Doctor of Philosophy

Eric M. Golden, B.S., M.S.
Major, USAF

18 September 2014

AFIT-ENP-DS-14-S-07

HYPERFINE INTERACTIONS IN THE ELECTRON PARAMAGNETIC RESONANCE SPECTRA OF POINT DEFECTS IN WIDE-BAND-GAP SEMICONDUCTORS

Eric M. Golden, B.S., M.S.
Major, USAF

Approved:

//signed//
Dr. Nancy C. Giles (Chair)

8 August 2014
Date

//signed//
Dr. Larry E. Halliburton (Member)

8 August 2014
Date

//signed//
Dr. Derrick Langley (Member)

8 August 2014
Date

//signed//
Dr. John W. McClory (Member)

8 August 2014
Date

Accepted:

//signed//
Dr. Adedeji B. Badiru
Dean, Graduate School of Engineering and
Management

14 August 2014
Date

Abstract

The focus of this research was to acquire definitive experimental data on predominant point defects in three important wide-band-gap semiconductors. Hyperfine interactions in electron paramagnetic resonance spectra were used to characterize the neutral nitrogen acceptor in zinc oxide, to identify a silicon interstitial impurity in titanium dioxide, and to determine the electronic structure of the singly ionized sulfur vacancy in stannous hexathiohypodiphosphate (SPS). Research on the basic properties of these technologically important materials plays a crucial role in the development of advanced optical and electronic systems.

Zinc oxide is an electro-optic material with the potential to produce high-performance electronics and also ultraviolet detectors and emitters. The angular dependencies of axial and basal ^{67}Zn hyperfine lines were used to extract ^{67}Zn hyperfine interaction parameters for the neutral nitrogen acceptor in zinc oxide. These data establish the exact nature of the ground-state wave function associated with this important acceptor. The experimental information obtained in this study about the ground-state wave function will allow computational theorists to model the nitrogen acceptor and determine whether it can successfully lead to p-type conduction in zinc oxide. The search for p-type zinc oxide is one of the most important basic questions in present-day research on wide-band-gap semiconductors.

Titanium dioxide is an energy-conversion material being developed for hydrogen generation and use as an electrode in lithium-ion batteries. The angular dependencies of an $I = 0$ line and two sets of ^{29}Si hyperfine lines were used to calculate g parameters and ^{29}Si hyperfine interaction parameters for a silicon-related $S = \frac{1}{2}$ defect in rutile titanium dioxide. These data were used to identify the defect as a deep donor composed of two silicons, with one silicon at a titanium site and the other silicon at a neighboring tetrahedral site. The model established in this study for silicon in rutile titanium dioxide is unique and confirms that silicon is an ubiquitous impurity in this material. Its presence may have a critical effect in photocatalytic applications.

SPS is a high-speed photorefractive material that is being developed for use as a protective element in visible and infrared sensor systems to guard against laser induced damage and/or jamming. The angular dependencies of two sets of ^{117}Sn and ^{119}Sn hyperfine lines, and two sets of ^{31}P hyperfine lines were used to determine g parameters and hyperfine interaction parameters for an intrinsic $S = \frac{1}{2}$ defect in SPS. These data were used to identify the defect as a singly ionized sulfur vacancy. This identification establishes the singly ionized sulfur vacancy as the dominant intrinsic defect (i.e., donor) in SPS and has direct implications for enhancing the photorefractive properties of this emerging material.

Acknowledgements

I would like to thank Dr. Nancy Giles and Dr. Larry Halliburton for the opportunity to work on some very interesting research. I am very thankful for Dr. Giles's willingness to be my research advisor when it seemed that my future as a student was in peril. I am thankful for Dr. Halliburton's instruction on the operation of the laboratory and his insights into science, research, and academic career development through our many conversations. Their encouragement and trust in my abilities, along with those of my wife and daughters, were primary factors that sustained me throughout this process. I would also like to thank Dr. Derrick Langley and Dr. John McClory for allowing me to borrow some of their time to serve on my research committee. Finally, I would like to acknowledge the previous works of Dr. Adam Brant, Dr. Sean Evans, and Dr. Shan Yang, which laid the foundation for the research in this dissertation.

Table of Contents

List of Figures

List of Tables

HYPERFINE INTERACTIONS IN THE ELECTRON PARAMAGNETIC RESONANCE SPECTRA OF POINT DEFECTS IN WIDE-BAND-GAP SEMICONDUCTORS

I. Introduction

The origins of magnetic resonance date back to the Nobel-prize-winning Stern-Gerlach experiment [1]. In this experiment, neutral silver atoms from a furnace are directed through a static magnetic field and captured on a screen to measure their deflection angle. The axis of the magnetic field is normal to the initial path of the silver atoms. If the silver atom has a magnetic moment, then it will deflect according to the orientation of the magnetic moment when it enters the magnetic field. If the magnetic moment of the silver atom is due to a classical angular momentum and thus zero, then the angular distribution of the silver atoms will have only one centroid elongated along the axis of the magnetic field. The silver atom was observed to have a magnetic moment, and the angular distribution was observed to have two centroids displaced along the axis of the magnetic field. This result was explained by Uhlenbeck and Goudsmit [2] as a quantum interaction between the unpaired electron in the 5*s* orbital of the silver atom and the magnetic field. This quantum interaction only allows for the magnetic moment of the electron to align parallel or antiparallel to the magnetic field. Since an electron in an *s* orbital has no orbital angular momentum, the magnetic moment is entirely[1] due to an angular momentum that is intrinsic to the electron. Because of this, the Stern-Gerlach experiment established the concept of intrinsic

---

[1] Silver has two isotopes with $I = \frac{1}{2}$ that make up 100% of all naturally occurring silver atoms [3, 4]. Therefore, the magnetic moment of a neutral silver atom is not entirely due to the 5*s* electron. As seen in Section 2.1, the magnetic moment of the silver nucleus is much weaker than that of the electron. The Stern-Gerlach experiment lacked the resolution necessary to detect the hyperfine interaction between the 5*s* electron and the silver nucleus. Breit and Rabi [5] described this hyperfine interaction in the context of the Stern-Gerlach experiment, and Rabi *et al.* [6] were the first to directly measure nuclear magnetic moments with this beam technique [7].

quantum angular momentum or spin angular momentum. A discussion of classical and quantum angular momentum is included in Appendix A. This establishment of spin angular momentum gave rise to a variety of magnetic resonance techniques, including electron paramagnetic resonance, nuclear magnetic resonance, and electron-nuclear double resonance. Both pulsed and continuous-wave magnetic resonance techniques have been developed. The experimental technique used in the present dissertation is cw electron paramagnetic resonance spectroscopy.

Electron paramagnetic resonance was first observed by Zavoisky in 1944 [7]. After this discovery, significant contributions by Abragam, Bleaney, Pryce, and Van Vleck in the early 1950s led to well-developed theories of electron paramagnetic resonance and well-developed techniques of electron paramagnetic resonance spectroscopy [7]. Electron paramagnetic resonance is observed when defects or impurities with one or more electrons that do not share a wave function with another electron of opposite spin are present. These electrons are called unpaired electrons or unpaired spins. As discussed in Chapter II, these unpaired electrons interact with an applied magnetic field creating magnetic-field-dependent energy levels. Electron paramagnetic resonance spectroscopy is a collection of experimental techniques used for detecting transitions between these energy levels in insulating and semiconducting crystals, amorphous materials, and free radicals. As discussed in Chapter III, the technique used in this dissertation research involves the observation of magnetic-field-dependent absorptions of microwaves in a resonant cavity containing the sample. The energy of the microwaves (i.e., their frequency) is held constant while an applied magnetic field splits the energy levels. An absorption occurs whenever the energy of the microwaves equals the energy difference between two energy levels of an allowed transition. An electron paramagnetic resonance spectrum in this case is a recording of the reflected power from the cavity as the magnetic field is swept across a specified range. With this technique, the observation of hyperfine interactions is particularly useful in the identification of paramagnetic defects.

As discussed in Section 2.4, the hyperfine interaction is dependent upon the ground-state wave function of an unpaired electron or unpaired electrons in the presence of nuclei that possess a magnetic moment. Because of this, hyperfine interactions provide information about the local physical environment of the defect, and contain information about the ground-state electronic structure of the defect in its paramagnetic state. In this dissertation, observations of hyperfine interactions are used to further characterize or identify point defects in three wide-band-gap semiconductors of particular military and commercial importance. These wide-band-gap semiconductors are zinc oxide (ZnO), titanium dioxide (TiO_2), and stannous hexathiohypodiphosphate ($Sn_2P_2S_6$). All of these materials have properties that are dependent on the presence of point defects. Therefore, it is essential to identify and characterize these point defects in order to understand the processes that give rise to the desired material properties.

1.1 Point Defects

A point defect is an interruption in the periodicity of a crystal lattice that is localized within a few lattice sites. A crystal lattice is composed of a Bravais lattice which is a periodic set of sites defined by a set of three vectors. At each Bravais lattice site, there is a basis which is an arrangement of atoms about the site. Because of this, a crystal lattice is composed of sublattices which are Bravais lattices formed by each atom in the basis. The simplest point defects are characterized as intrinsic or extrinsic and substitutional or interstitial. An intrinsic point defect involves atoms that are native to the crystal, while extrinsic point defects involve atoms that are not native to the crystal. A substitutional point defect is located at a crystal lattice site, while an interstitial point defect is not located at a crystal lattice site. Intrinsic substitutional point defects include vacancies and antisites. A vacancy is the absence of an atom at a crystal lattice site, and an antisite is a native atom that is located at a sublattice site to which it does not belong. Intrinsic interstitial point defects are called self-interstitials, and are native atoms that are not located at a crystal lattice site. Extrinsic substitutional point defects are called substitutional impurities, and are atoms that are not native to the crystal and are located at a crystal lattice site. Extrinsic interstitial point defects are called interstitial impurities, and are atoms that are not native to the crystal and not located at a crystal lattice site. These simple point defects can couple to form complex point defects. The point at which a complex point defect becomes an extended defect can be ambiguous. At some point as the complex gets larger, it will take on its own physical properties that are separate from that of the crystal, i.e., an inclusion is formed. As the defect concentration gets even larger, all the point defects will couple changing the physical properties of the entire crystal, with the result being an alloy.

A characteristic of any semiconductor crystal is the existence of a band gap between two broad electronic energy bands. For a flawless semiconductor crystal at a temperature of 0 K, one band called the conduction band is unoccupied by electrons and the other called the valence band is completely occupied with electrons. In this flawless frozen state, the semiconductor crystal is not electronically conductive. At higher temperatures, electrons can become thermally excited into the conduction band, thus creating two current-carrying particles and becoming electronically conductive. One current-carrying particle is the electron in the conduction band and the other is a pseudo-particle called a hole in the valence band. This happens at room temperature for narrow-band-gap semiconductors such as silicon and germanium. For wide-band-gap semiconductors, this effect is minuscule at room temperature. However, point defects in wide-band-gap semiconductor crystals can create either conduction-band electrons or valence-band holes when ionized by thermal excitation, electromagnetic irradiation, or particle irradiation.

A point defect that can supply a conduction-band electron when ionized is called a donor. An example of a donor is a Group III atom such as gallium substituting for zinc in zinc oxide. Gallium which has valence electrons in a $4s^24p$ configuration has one additional valence electron than zinc which has valence electrons in a $4s^2$ configuration. When gallium is substituted into the zinc sublattice as a neutral donor, this additional unpaired electron occupies a state with a highly diffuse wave function that is centered on the gallium. This is often referred to as an effective-mass or hydrogenic state. Evidence for this behavior is found in the electron paramagnetic resonance spectrum of the neutral shallow donor in zinc oxide. The spectrum consists of a single nearly isotropic electron paramagnetic resonance line with principal values of the g matrix around 1.96 [8, 9, 10]. Since both naturally occurring isotopes of gallium have $I = \frac{3}{2}$ [3, 4], the unresolved and weak hyperfine interaction suggests that the electron is not localized at the gallium, but is spread out (i.e., shared) over many shells of ions around the gallium impurity.

A point defect that can capture a valence-band electron creating a hole is called an acceptor. An example of an acceptor is a Group V atom such as nitrogen substituting for oxygen in zinc oxide. Nitrogen which has valence electrons in a $2s^2 2p^3$ configuration has one less valence electron than oxygen which has valence electrons in a $2s^2 2p^4$ configuration. When nitrogen is substituted into the oxygen sublattice as a neutral acceptor, this lack of an electron leaves an unpaired electron in a state that is highly localized about the nitrogen. Evidence for this is given in Chapter IV. In general, the wave functions of shallow acceptors are more localized than the wave functions of shallow donors.

1.2 Zinc Oxide

Zinc oxide is a versatile material that has been used for centuries in paints, pharmaceuticals, and ceramics and since the middle of the previous century, it has been investigated for use as a semiconductor. Its refractive properties and fine particle size when produced by the “American” or “French” methods give paints and pharmaceuticals such as sunscreen and cosmetics high “covering power” and give ceramic glazes “brilliance” [11]. By the 1930s, some physical and optical properties of zinc oxide were being explored [12]. By the 1960s it was being investigated for its semiconductor properties [13]. Properties of interest include a wide direct band gap and the possibility of band-gap engineering by alloying with cadmium and magnesium.

The band gap of zinc oxide is about 3.3 eV [14] which classifies it as a wide-band-gap semiconductor. This property is useful in high-voltage electronics, since wide-band-gap semiconductors are less susceptible to breakdown where high voltages can cause charge carriers to create electron-hole pairs through impact ionization or to tunnel through p-n junctions. A wide band gap also reduces the requirement that circuits be insulated from exposure to light because visible photons lack enough energy to create electron-hole pairs. Since silicon-based devices have a band gap of about 1.1 eV [15], visible and infrared photons can produce excess electron-hole pairs in the device which can significantly affect device performance. Due to its wide band gap, zinc oxide is transmissive to visible and infrared photons making it useful as a transparent conducting window for use in solar cells and displays, and absorptive to ultraviolet photons making it useful as an ultraviolet photodiode for use in ultraviolet detectors. Another aspect of the band gap in zinc oxide is that it is direct where the conduction-band minimum and the valence-band maximum appear at the same location in momentum space. This makes luminescent transitions more probable and with proper band-gap engineering, zinc oxide is suitable for ultraviolet light emitting devices such as light emitting diodes and laser diodes.

Since zinc oxide is a II-VI semiconductor, band-gap engineering is possible by alloying with Group IIA and IIB metals, and Group VI nonmetals and metalloids. The most promising elements for band-gap engineering are magnesium and cadmium [12, 13, 16]. Magnesium oxide has a band gap of about 8.7 eV [17], so the incorporation of magnesium increases the band gap of zinc oxide [18]. Cadmium oxide has a band gap of about 2.3 eV [19], so the incorporation of cadmium decreases the band gap of zinc oxide [18]. This ability to engineer the band gap is essential to the successful production of zinc oxide based heterostructures which are the building blocks of light emitting diodes, laser diodes, transistors, and many other electronic and photonic devices.

1.3 Titanium Dioxide

Like zinc oxide, titanium dioxide has found many uses in low-tech and high-tech applications. Titanium dioxide has been used as a white pigment in paints since the early part of the 20^{th} century because of its high refractive index [20]. It is also nontoxic making it a replacement for lead-based "white lead" paints [20]. It has also found a use as a diamond simulant in jewelry [11]. Recently, research on titanium dioxide has focused on its photocatalytic [21, 22] and ferromagnetic [23, 24] properties, and use as a memristor [25] and battery terminal [26].

Of particular use to the military are the photocatalytic properties of titanium dioxide and use as a battery terminal in lithium ion batteries. Joint terminal air controllers, combat controllers, and combat weathermen rely on compact and lightweight power systems to operate essential equipment such as radios, designators, sensors, and beacons. These operators routinely find themselves in remote and difficult terrain where they must carry their equipment and the power sources to operate them. Therefore, any improvement in the capacity or efficiency of these power sources will increase the operators ability to complete their mission. As a photocatalyst, titanium dioxide has the ability to hydrolyze water in the presence of ultraviolet light [21]. Hydrogen gas produced by this method can provide power through a fuel cell, thus increasing capacity as long as there is water and sunlight to fuel the process. Since titanium dioxide has better lithium-transport properties than current carbon-based materials, efficiency gains can be made by replacing the carbon electrodes in lithium ion batteries with titanium dioxide electrodes [26].

1.4 Stannous Hexathiohypodiphosphate

Recent studies of stannous hexathiohypodiphosphate (SPS) have focused on its ferroelectric [27] and photorefractive [28, 29, 30] properties. Although these properties have been well established in SPS, the point defects participating in these effects are not well established. Therefore, experimental techniques such as electron paramagnetic resonance spectroscopy are needed to identify the point defects and correlate their presence and properties to ferroelectric and photorefractive effects in the material. This information is subsequently used to monitor these defects for production of material with the desired properties.

Of particular use to the military are the high-speed photorefractive properties of SPS. High-sensitivity visible and infrared sensor systems have become an essential component in most weapons platforms. These sensors are used for missions such as surveillance, reconnaissance, targeting, tracking, and guidance. Because these sensor systems are composed of highly photosensitive components, they are prone to laser-induced damage and jamming. The proliferation of highly portable high-power visible and infrared laser systems has led to the need to protect these sensor systems. One method of protection is to direct the damaging/jamming laser radiation away from the photosensitive components. This is accomplished with photorefractive materials, because the refractive index of these materials is dependent upon the intensity of light illuminating them. An intensity pattern created by the interference between the damaging/jamming laser and a local laser "writes" a diffraction grating into the photorefractive material. This diffraction grating then deflects the damaging/jamming laser radiation away from the photosensitive components of the sensor system, thus protecting the photosensitive components from damage, and/or eliminating the jamming signal.

II. Principles of Electron Paramagnetic Resonance Spectroscopy

In general, spectroscopy is the detection of discrete transitions between energy levels present within a material. These transitions, or resonances, are detected by exposing the material to a source of photons (e.g., ultraviolet light, visible light, infrared light, or microwaves) and measuring either a reflection or absorption of these photons in the material. Electron paramagnetic resonance spectroscopy involves transitions between energy levels created by the interactions of one or more unpaired electrons with a magnetic field and any other magnetic moments present in the material. These interactions are described by a spin Hamiltonian and each interaction adds its own component to the spin Hamiltonian. With a knowledge of the specific interactions present in a particular spin system, a total spin Hamiltonian is constructed as a sum of each interaction's contribution to the spin-dependent energy.

2.1 Magnetic Moments

For a classical electrodynamic system [31], the magnetic field created by a general current distribution is

$$\mathbf{B}(\mathbf{r}) = \frac{\mu_0}{4\pi}\nabla \times \int \frac{\mathbf{J}(\mathbf{r}')}{|\mathbf{r}-\mathbf{r}'|}d^3\mathbf{r}' \tag{1}$$

where μ_0 is the permeability of free space, $\mathbf{J}$ is the current density, $\mathbf{r}$ is the position vector of the magnetic field, $\mathbf{r}'$ is the position vector of the current density, and $d^3\mathbf{r}'$ indicates integration over the volume containing the current density. For a system of localized current density placed about the origin, the denominator of Equation (1) is expanded in a Maclauren series with respect to the primed coordinates to approximate the magnetic field when $|\mathbf{r}| >> |\mathbf{r}'|$,

$$\frac{1}{|\mathbf{r}-\mathbf{r}'|} = \frac{1}{|\mathbf{r}|} + \frac{\mathbf{r}\cdot\mathbf{r}'}{|\mathbf{r}|^3} + \ldots \tag{2}$$

Substituting this expansion into Equation (1) results in

$$\mathbf{B}(\mathbf{r}) = \frac{\mu_0}{4\pi}\nabla \times \left(\frac{1}{|\mathbf{r}|}\int \mathbf{J}(\mathbf{r}')d^3\mathbf{r}' + \frac{1}{|\mathbf{r}|^3}\int \mathbf{J}(\mathbf{r}')(\mathbf{r}\cdot\mathbf{r}')d^3\mathbf{r}' + \dots \right). \tag{3}$$

The first term in this equation is called the monopole term and the second is called the dipole term. Since the current density is assumed to be localized with no divergence, the monopole term is zero and the dipole term can be written as

$$\frac{1}{|\mathbf{r}|^3}\int \mathbf{J}(\mathbf{r}')(\mathbf{r}\cdot\mathbf{r}')d^3\mathbf{r}' = \frac{\mathbf{m}\times\mathbf{r}}{|\mathbf{r}|^3} \tag{4}$$

where

$$\mathbf{m} = \frac{1}{2}\int \mathbf{r}' \times \mathbf{J}(\mathbf{r}')d^3\mathbf{r}' \tag{5}$$

is called the magnetic moment. With these transformations, the magnetic field outside of a localized current density is approximated as

$$\begin{aligned} \mathbf{B}(\mathbf{r}) &= \frac{\mu_0}{4\pi}\nabla \times \frac{\mathbf{m}\times\mathbf{r}}{|\mathbf{r}|^3} \\ &= \frac{\mu_0}{4\pi|\mathbf{r}|^3}\left(2\mathbf{m} - 3\frac{\mathbf{r}\times\mathbf{m}\times\mathbf{r}}{|\mathbf{r}|^2}\right) \\ &= \frac{\mu_0}{4\pi|\mathbf{r}|^3}\left(3\frac{(\mathbf{r}\cdot\mathbf{m})\mathbf{r}}{|\mathbf{r}|^2} - \mathbf{m}\right). \end{aligned} \tag{6}$$

An example of a simple magnetic moment is that of a charged particle in a circular orbit. The current generated by the orbiting particle is

$$\mathbf{I} = \frac{q\mathbf{v}}{2\pi|\mathbf{r}|} \tag{7}$$

and the orbital angular momentum is

$$\mathbf{L} = \mathbf{r} \times m\mathbf{v} \tag{8}$$

where q is the charge of the particle, $\mathbf{v}$ is the velocity of the particle, $\mathbf{r}$ is the orbital position of the particle, and m is the mass of the particle. Since

$$\mathbf{J}(\mathbf{r}')d^3\mathbf{r}' \to \mathbf{I}(\mathbf{r}')d\mathbf{r}' \tag{9}$$

for filamental currents in a closed circuit, substituting Equations (7) and (8) into Equation (5) results in

$$\mathbf{m} = \frac{1}{2}\left(\mathbf{r} \times \mathbf{I}\right) 2\pi|\mathbf{r}| = \frac{q}{2m}\mathbf{L}. \tag{10}$$

This is the classical relation between magnetic moment and orbital angular momentum.

When this concept is applied to quantum mechanical systems, the magnetic moment is viewed as a magnetic moment operator,

$$\hat{\mathbf{m}} = \frac{q\hbar}{2m}\hat{\mathbf{L}}. \tag{11}$$

The magnetic moment due to spin angular momentum can differ from that of the classical result. This is due to other quantum mechanical and relativistic effects not discussed here. These effects are accounted for with a g factor,

$$\hat{\mathbf{m}} = g\frac{q\hbar}{2m}\hat{\mathbf{S}}. \tag{12}$$

For a free electron, the magnetic moment operator is

$$\hat{\mathbf{m}} = -g_e\frac{e\hbar}{2m_e}\hat{\mathbf{S}} = -g_e\mu_B\hat{\mathbf{S}} \tag{13}$$

where g_e is the free electron g factor and is known to be 2.0023 [32], e is the elementary charge, m_e is the electron mass, and μ_B is the Bohr magneton and is known to be $9.2740 \times 10^{-24}\ J/T$ [32]. For a nucleus, the magnetic moment operator is

$$\hat{\mathbf{m}} = g_n\frac{e\hbar}{2m_p}\hat{\mathbf{I}} = g_n\mu_N\hat{\mathbf{I}} \tag{14}$$

where g_n is the g factor of a particular nucleus and is on the order of unity, m_p is the proton mass, and μ_N is the nuclear magneton and is known to be 5.0508×10^{-27} J/T [32]. Since the order of the nuclear g factor is unity and the nuclear magneton is three orders of magnitude less than the Bohr magneton, the electron has a magnetic moment that is significantly greater than all known nuclei. The nuclear g factor typically carries the sign of the magnetic moment because neutral particles, like the neutron, have a magnetic moment even though they carry no charge and some nuclei have a magnetic moment that is in opposition to its spin even though they carry only positive charge.

2.2 Spin Hamiltonian

A quantum mechanical system can be in any number of quantum mechanical states represented by the kets $|\psi_n\rangle$ with the requirement that the kets obey the time independent Schrödinger equation.

$$\hat{H}\,|\psi_n\rangle = E_n\,|\psi_n\rangle \tag{15}$$

where $\hat{H}$ is the Hamiltonian operator and E_n is the energy of the state. The Hamiltonian includes terms that account for the kinetic energy of the system and the potential energy of the system.

$$\hat{H} = \hat{T} + \hat{U}. \tag{16}$$

In this equation, $\hat{T}$ accounts for kinetic energy and $\hat{U}$ accounts for potential energy. The potential energy can be further separated into parts that account for potentials that are purely a function of spatial coordinates and potentials that are dependent on the spin angular momenta of the particles that make up the system.

$$\hat{H} = \hat{T} + \hat{U}_r + \hat{U}_s = \hat{H}_r + \hat{U}_s \tag{17}$$

where $\hat{U}_r$ is the spatial potential and only contains purely spatial contributions to the potential energy, $\hat{U}_s$ is the spin potential and only contains potentials that are dependent on spin, and $\hat{H}_r$ is the spatial Hamiltonian and only contains purely spatial contributions to the total energy.

The spin potential can be treated as a perturbation to the ground state of the spatial Hamiltonian. The first-order perturbation to the ground-state energy is

$$E_0 = E_0^{(r)} + \left\langle \psi_0^{(r)} \middle| \hat{U}_s \middle| \psi_0^{(r)} \right\rangle \tag{18}$$

where $\left|\psi_0^{(r)}\right\rangle$ represents the ground state of the spatial Hamiltonian and $E_0^{(r)}$ is the ground-state energy of the spatial Hamiltonian such that

$$\hat{H}_r \left|\psi_0^{(r)}\right\rangle = E_0^{(r)} \left|\psi_0^{(r)}\right\rangle . \tag{19}$$

Since the spin of a particle is an intrinsic characteristic, it is reasonable to assume that the spin operators commute with the spatial Hamiltonian, therefore sharing a common set of eigenstates. Because of this, the ground state can be represented by the kets $\left|m_{S_i}, \psi_0^{(r)}\right\rangle$, and the spatial part of the ground state can be treated separately from the spin part of the ground state.

To illustrate this concept, suppose that a spin-dependent potential has the form

$$\hat{U}_s = f(\mathbf{r})\hat{S}_z. \tag{20}$$

The first-order perturbation of this operator to the ground-state energy is

$$\left\langle m_S, \psi_0^{(r)} \middle| \hat{S}_z f(\mathbf{r}) \middle| m_S, \psi_0^{(r)} \right\rangle = m_S \int \psi_0^{(r)*}(\mathbf{r}) f(\mathbf{r}) \psi_0^{(r)}(\mathbf{r}) d^3\mathbf{r}. \tag{21}$$

Since the spatial part of the ground state can be considered separately from the spin part, the spin Hamiltonian for this operator is defined as

$$\hat{H}_s = \hat{S}_z \int \psi_0^{(r)*}(\mathbf{r}) f(\mathbf{r}) \psi_0^{(r)}(\mathbf{r}) d^3\mathbf{r} \tag{22}$$

which is the original operator with the spatial parts averaged. Therefore, the spin Hamiltonian is defined as the spin-dependent potentials of the Hamiltonian with the spatial parts averaged according to the ground state of the spatial Hamiltonian.

The spin Hamiltonian represents perturbations to the ground state of the system. In most cases, differences in energy (resonances) are measured in an experiment. Because of this, the ground-state energy can be ignored and the spin Hamiltonian can be used to explain transitions between energy levels in a spin system. These phenomena include but are not limited to the Zeeman effect, fine interactions, hyperfine interactions, and nuclear electric quadrupole interactions. All of these phenomena are appropriate for describing energy transitions in a spin system with a single unpaired electron (i.e., an $S = \frac{1}{2}$ system), and are described in the following sections.

2.3 Zeeman Effect

The Zeeman effect is caused by a change in the potential energy of a magnetic moment due to the presence of a magnetic field. It is a quantum mechanical effect, and gives rise to electron paramagnetic resonance phenomena when applied to electrons and to nuclear magnetic resonance phenomena when applied to nuclei. For a classical electrodynamic system [31], the potential energy of a magnetic moment in a magnetic field is

$$U = -\mathbf{m} \cdot \mathbf{B}. \tag{23}$$

The magnetic moment in this equation is replaced with the magnetic moment operator of an electron or nucleus to arrive at the spin Hamiltonian.

The spin Hamiltonian of a free electron is

$$\hat{H}_s = g_e \mu_B \hat{\mathbf{S}} \cdot \mathbf{B}. \tag{24}$$

Since the electron is a half-spin particle, the eigenstates of this spin Hamiltonian are represented by the kets $|m_S\rangle$ where $m_S \in \{+\frac{1}{2}, -\frac{1}{2}\}$. Selection of the projection axis of the spin operator is arbitrary, therefore it is common to place the projection axis along the magnetic field to simplify the equation. Doing this results in

$$\hat{H}_s = g_e \mu_B B \hat{S}_z \tag{25}$$

where B is the magnitude of the magnetic field. The action of the spin Hamiltonian on the eigenstates results in

$$\begin{aligned} \hat{H}_s \left|+\frac{1}{2}\right\rangle &= g_e \mu_B B \hat{S}_z \left|+\frac{1}{2}\right\rangle = +\frac{g_e \mu_B B}{2} \left|+\frac{1}{2}\right\rangle = E_{+\frac{1}{2}} \left|+\frac{1}{2}\right\rangle \quad \text{and} \\ \hat{H}_s \left|-\frac{1}{2}\right\rangle &= g_e \mu_B B \hat{S}_z \left|-\frac{1}{2}\right\rangle = -\frac{g_e \mu_B B}{2} \left|-\frac{1}{2}\right\rangle = E_{-\frac{1}{2}} \left|-\frac{1}{2}\right\rangle \end{aligned} \tag{26}$$

where $E_{+\frac{1}{2}}$ and $E_{-\frac{1}{2}}$ are the two energy levels of the system. Electron paramagnetic resonance is observed by detecting the absorption of photons due to a transition from the lower energy $\left|-\frac{1}{2}\right\rangle$ state to the higher energy $\left|+\frac{1}{2}\right\rangle$ state. The energy of this transition is

$$E = E_{+\frac{1}{2}} - E_{-\frac{1}{2}} = g_e \mu_B B = h\nu_r \tag{27}$$

where ν_r is the frequency of the photon necessary for absorption. The energy levels as a function of magnetic field are presented in Figure 1 for a free electron.

The spin Hamiltonian of a nucleus is

$$\hat{H}_s = -g_n \mu_N \hat{\mathbf{I}} \cdot \mathbf{B}. \tag{28}$$

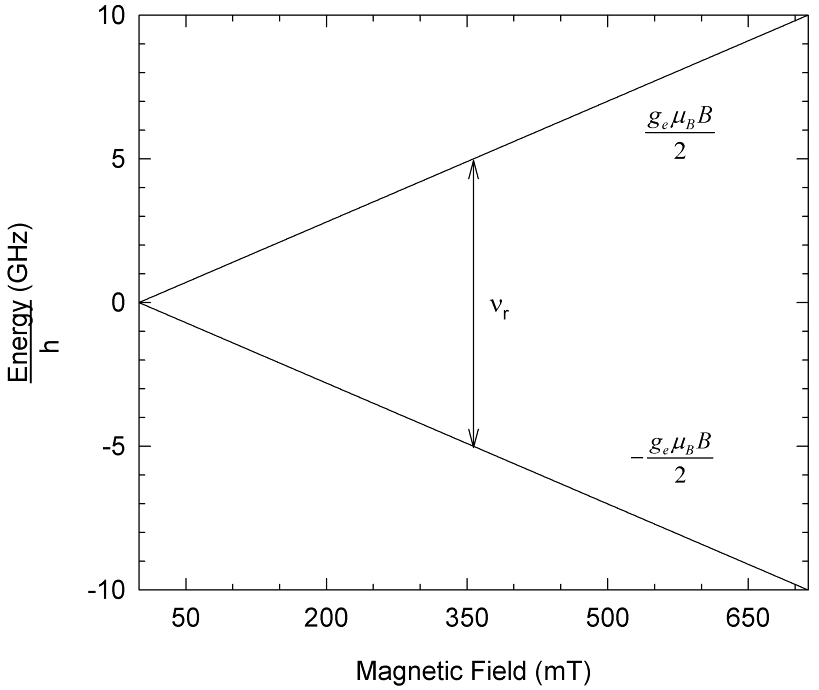

Figure 1. Energy levels due to the Zeeman effect for a free electron as a function of magnetic field. The vertical double arrow line corresponds to an electron paramagnetic resonance of 10 GHz.

Selection of the projection axis along the magnetic field results in

$$\hat{H}_s = -g_n \mu_N B \hat{I}_z. \tag{29}$$

The eigenstates of this spin Hamiltonian are represented by kets $|m_I\rangle$ where $m_I \in \{-I, -I+1, \ldots, I-1, I\}$ and $I \in \left\{0, \frac{1}{2}, 1, \frac{3}{2}, \ldots\right\}$. Since a nucleus can have a spin quantum number greater than one, there are $2I + 1$ energy levels with values of

$$E_{m_I} = -g_n \mu_N B m_I. \tag{30}$$

Nuclear magnetic resonance is observed by detecting the absorption of photons due to a transition from a lower energy state to a higher energy state. The selection rule for this process is that the absolute value of the difference between the spin projection quantum number of the final state and the spin projection quantum number of the initial state must equal one. Because of the selection rule, the energy of this transition is

$$E = |E_{m_I+1} - E_{m_I}| = |g_n|\mu_N B = h\nu_r. \tag{31}$$

In general, the electron is not free and can be bound within an atom, molecule, or point defect. In this case, the electron can have orbital angular momentum in addition to spin angular momentum. The spin Hamiltonian becomes

$$\hat{H}_s = \mu_B(g_e\hat{\mathbf{S}} + \hat{\mathbf{L}}) \cdot \mathbf{B} + \lambda\hat{\mathbf{S}} \cdot \hat{\mathbf{L}} = g_e\mu_B\hat{\mathbf{S}} \cdot \mathbf{B} + \left(\mu_B\mathbf{B} + \lambda\hat{\mathbf{S}}\right) \cdot \hat{\mathbf{L}} \tag{32}$$

where λ is a spin-orbit coupling coefficient. It is necessary to write this spin Hamiltonian in terms of the spin operator alone. This is accomplished by applying a second-order perturbation [7]. Doing this results in

$$\hat{H}_s = g_e\mu_B\hat{\mathbf{S}} \cdot \mathbf{B} + (\mu_B)^2\,\mathbf{B} \cdot \mathbf{\Lambda} \cdot \mathbf{B} + 2\lambda\mu_B\hat{\mathbf{S}} \cdot \mathbf{\Lambda} \cdot \mathbf{B} + \lambda^2\hat{\mathbf{S}} \cdot \mathbf{\Lambda} \cdot \hat{\mathbf{S}}. \tag{33}$$

The elements of the $\mathbf{\Lambda}$ matrix are

$$\Lambda_{ij} = -\sum_{n=1}^{\infty}\sum_{i}\sum_{j} \frac{\left\langle \psi_0^{(r)} \right| \hat{L}_i \left| \psi_n^{(r)} \right\rangle \left\langle \psi_n^{(r)} \right| \hat{L}_j \left| \psi_0^{(r)} \right\rangle}{E_n^{(r)} - E_0^{(r)}} \tag{34}$$

where $i, j \in \{x, y, z\}$, $\psi_0^{(r)}$ is the ground state of the spatial Hamiltonian, $E_0^{(r)}$ is the ground-state energy of the spatial Hamiltonian, $\psi_n^{(r)}$ is an excited state of the spatial Hamiltonian, and $E_n^{(r)}$ is an excited-state energy of the spatial Hamiltonian. The second term in Equation (33) adds the same amount of energy to all energy levels. Because of this, it can be ignored when observing energy transitions. The last term in Equation (33) adds the same amount of energy to all energy levels whenever the spin quantum number is equal to $\frac{1}{2}$. Because of this, it can be ignored when observing energy transitions in a half-spin system. Taking this into consideration, the spin Hamiltonian becomes

$$\hat{H}_s = \mu_B\hat{\mathbf{S}} \cdot \mathbf{g} \cdot \mathbf{B} + \hat{\mathbf{S}} \cdot \mathbf{D} \cdot \hat{\mathbf{S}} \tag{35}$$

where

$$\mathbf{g} = g_e\mathbf{1} + 2\lambda\mathbf{\Lambda}, \quad \text{and} \quad \mathbf{D} = \lambda^2\mathbf{\Lambda}. \tag{36}$$

Matrix **g** is called a *g* matrix, matrix **D** is called a fine interaction matrix, and matrix **1** is the identity matrix.

2.4 Hyperfine Interaction

The hyperfine interaction is an interaction between magnetic moments and the magnetic fields that they generate. It is a quantum mechanical effect, and is observed in electron paramagnetic resonance spectroscopy when the magnetic moment of an electron interacts with that of a nucleus. When the magnetic field is generated by another magnetic moment placed at some origin, Equation (6) is substituted into Equation (23) to arrive at

$$U = \frac{\mu_0}{4\pi|\mathbf{r}|^3}\left(\mathbf{m}_r \cdot \mathbf{m}_o - 3\frac{(\mathbf{r}\cdot\mathbf{m}_o)(\mathbf{m}_r\cdot\mathbf{r})}{|\mathbf{r}|^2}\right) \tag{37}$$

where **r** is the position vector of magnetic moment $\mathbf{m}_r$, and $\mathbf{m}_o$ is the magnetic moment at the origin. Since the hyperfine interation is between the magnetic moments of an electron and a nucleus, the magnetic moment at the origin is replaced with the magnetic moment operator of a nucleus, and the magnetic moment at **r** is replaced with the magnetic moment operator of an electron to arrive at

$$\hat{U} = \frac{\mu_0 g_e \mu_B g_n \mu_N}{4\pi}\left(3\frac{(\mathbf{r}\cdot\hat{\mathbf{I}})(\hat{\mathbf{S}}\cdot\mathbf{r})}{|\mathbf{r}|^5} - \frac{\hat{\mathbf{S}}\cdot\hat{\mathbf{I}}}{|\mathbf{r}|^3}\right). \tag{38}$$

It is convenient to place the nucleus at the origin and the electron at **r**, since in most cases the nucleus is relatively stationary while the electron can be at many other positions with a probability defined by its ground-state spatial wave function. Expanding Equation (38) results in

$$\hat{U} = \frac{\mu_0 g_e \mu_B g_n \mu_N}{4\pi}\sum_i\sum_j\left(3\frac{r_i r_j}{|\mathbf{r}|^5} - \frac{\delta_{ij}}{|\mathbf{r}|^3}\right)\hat{S}_i\hat{I}_j \tag{39}$$

where $i, j \in \{x, y, z\}$, and δ_{ij} is a Kronecker delta. In order to arrive at the spin Hamiltonian, the parenthetical expression in Equation (39) must be replaced by

$$\left(3\frac{r_i r_j}{|\mathbf{r}|^5} - \frac{\delta_{ij}}{|\mathbf{r}|^3}\right) \rightarrow \int \psi_0^{(r)*}(\mathbf{r}) \left(3\frac{r_i r_j}{|\mathbf{r}|^5} - \frac{\delta_{ij}}{|\mathbf{r}|^3}\right) \psi_0^{(r)}(\mathbf{r}) d^3\mathbf{r} \tag{40}$$

where $\psi_0^{(r)}$ is the ground-state spatial wave function of the electron. After accomplishing this, the spin Hamiltonian becomes

$$\hat{H}_s = \hat{\mathbf{S}} \cdot \mathbf{A} \cdot \hat{\mathbf{I}} \tag{41}$$

where $\mathbf{A}$ is called the hyperfine interaction matrix and its elements are

$$A_{ij} = \frac{\mu_0 g_e \mu_B g_n \mu_N}{4\pi} \int \psi_0^{(r)*}(\mathbf{r}) \left(3\frac{r_i r_j}{|\mathbf{r}|^5} - \frac{\delta_{ij}}{|\mathbf{r}|^3}\right) \psi_0^{(r)}(\mathbf{r}) d^3\mathbf{r}. \tag{42}$$

Equation (40) becomes problematic whenever $\mathbf{r}$ is a null vector. This occurs whenever the electron occupies an s orbital about a nucleus. Because of this, the hyperfine interaction requires the addition of a contact interaction to account for an electron in an s orbital. The potential energy of this interaction is

$$U = -\frac{2}{3}\mu_0 |\psi_0^{(r)}(0)|^2 \mathbf{m}_e \cdot \mathbf{m}_n \tag{43}$$

where $|\psi_0^{(r)}(0)|^2$ is the probability that the electron is at the nucleus, $\mathbf{m}_e$ is the magnetic moment of the electron, and $\mathbf{m}_n$ is the magnetic moment of the nucleus [33]. Replacing the magnetic moments with their appropriate quantum expressions results in the spin Hamiltonian

$$\hat{H}_s = \frac{2}{3}\mu_0 g_e \mu_B g_n \mu_N |\psi_0^{(r)}(0)|^2 \hat{\mathbf{S}} \cdot \hat{\mathbf{I}} = A\hat{\mathbf{S}} \cdot \hat{\mathbf{I}}. \tag{44}$$

The coefficient A is called the isotropic hyperfine interaction parameter or the Fermi

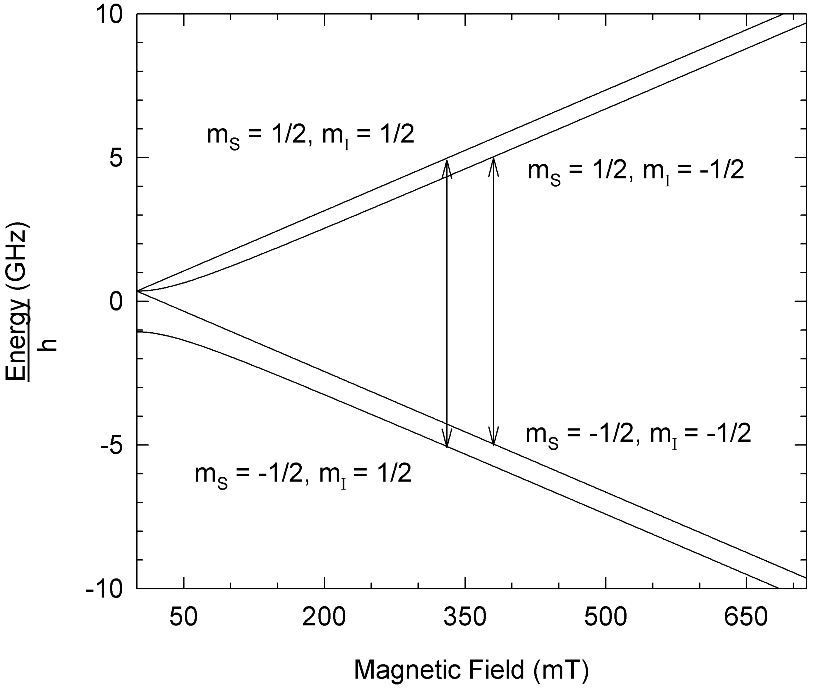

Figure 2. Energy levels due to magnetic interactions between an electron and a proton in a hydrogen atom as a function of magnetic field. The vertical double arrow lines correspond to electron paramagnetic resonances of 10 GHz. The two high-energy levels are more closely spaced than the two low-energy levels due in part to the nuclear Zeeman effect. The two high-energy levels will eventually cross at about 16.655 T where the nuclear Zeeman effect becomes equivalent to the hyperfine interaction.

contact term. Addition of Equation (44) to the spin Hamiltonian results in

$$\hat{H}_s = A\hat{\mathbf{S}}\cdot\hat{\mathbf{I}} + \hat{\mathbf{S}}\cdot\mathbf{A}\cdot\hat{\mathbf{I}} = \hat{\mathbf{S}}\cdot[A\mathbf{1}+\mathbf{A}]\cdot\hat{\mathbf{I}} \rightarrow \hat{\mathbf{S}}\cdot\mathbf{A}\cdot\hat{\mathbf{I}} \tag{45}$$

where $A\mathbf{1}$ is the isotropic hyperfine interaction matrix.

An example of a spin system with a hyperfine interaction is the hydrogen atom. The spin Hamiltoniam for this spin system is

$$\hat{H}_s = g_e\mu_B\hat{\mathbf{S}}\cdot\mathbf{B} + A\hat{\mathbf{S}}\cdot\hat{\mathbf{I}} - g_p\mu_N\hat{\mathbf{I}}\cdot\mathbf{B} \tag{46}$$

where g_p is the free proton g factor and is known to be 5.5857 [32] and A is the isotropic hyperfine interaction parameter of hydrogen and is known to be 1420.4 MHz

[34]. The eigenstates of the spin operators are represented by kets $|m_S, m_I\rangle$ where $m_S, m_I \in \{-\frac{1}{2}, +\frac{1}{2}\}$. The spin Hamiltonian is represented in this spin basis as a 4×4 matrix. This spin Hamiltonian matrix is diagonalized to extract the four energy levels and four eigenstates. A plot of the energy levels as a function of magnetic field is presented in Figure 2.

2.5 Nuclear Electric Quadrupole Interaction

Since all nuclei except for ^{1}H are composed of multiple protons and neutrons, these nuclei will have a definitive charge density. If this charge density is not spherically symmetric, then the electric potential is dependent on the orientation of the nucleus. This orientation is defined by the spin angular momentum of the nucleus. This gives rise to a spin dependent potential that must be included in the spin Hamiltonian. The electric potential in terms of the spherical harmonics is

$$V = \frac{1}{\epsilon_0} \sum_{l=0}^{\infty} \sum_{m=-l}^{l} \frac{Y_{lm}(\mathbf{r})}{(2l+1)|\mathbf{r}|^{l+1}} \int Y_{lm}^*(\mathbf{r}')|\mathbf{r}'|^l \rho(\mathbf{r}') d^3\mathbf{r}' \tag{47}$$

where Y_{lm} is a spherical harmonic and ρ is the charge density [31]. Due to symmetry rules in the standard model of particle physics, only potentials with even values of l that satisfy $l \leq 2I$ are nonvanishing [35]. The $l = 0$ term is called the monopole term and gives rise to a spherically symmetric potential that is independent of the spin angular momentum. Because of this, the monopole term is not included in the spin Hamiltonian. Therefore, the most significant terms in the electric potential that contribute to the spin Hamiltonian are the $l = 2$ terms. These terms are called quadrupole terms. The quadrupole potential can be put into terms of the spin angular momentum operators by evoking the Wigner-Eckart theorem [35]. This results in

$$\hat{H}_s = \hat{\mathbf{I}} \cdot \mathbf{Q} \cdot \hat{\mathbf{I}} \tag{48}$$

where in the principal axis basis of the matrix

$$\mathbf{Q} \rightarrow \frac{e^2 qQ}{2I(2I-1)} \begin{bmatrix} -1 & 0 & 0 \\ 0 & -1 & 0 \\ 0 & 0 & 2 \end{bmatrix} + F \begin{bmatrix} 1 & 0 & 0 \\ 0 & -1 & 0 \\ 0 & 0 & 0 \end{bmatrix}. \tag{49}$$

In this equation, F is an anisotropy factor, eq is the electric-field gradient at the nucleus, and

$$eQ = 2\sqrt{\frac{4\pi}{5}} \int Y_{20}^{*}(\mathbf{r}')|\mathbf{r}'|^2 \rho(\mathbf{r}') d^3\mathbf{r}' \tag{50}$$

where Q is called the nuclear electric quadrupole moment and is usually given in barns (10^{-28} m^2).

III. Instrumentation of Electron Paramagnetic Resonance Spectrometers

An electron paramagnetic resonance spectrometer is designed to detect energy transitions in a spin system. It consists of a source of microwaves, a microwave detector, and a large electromagnet. Typical water-cooled electromagnets can create magnetic fields of up to 1.5 T. For a free electron, this electromagnet can produce splittings in the energy levels corresponding to frequencies of up to 42 GHz. Electromagnetic radiation with frequencies of $1 - 100$ GHz covers the L, S, X, Q, and W microwave bands of the electromagnetic spectrum [36]. Transitions within a spin system caused by microwaves can be measured by absorption where a material is placed within a waveguide that connects the microwave source and detector, or by reflection where a material is placed within a resonant cavity that reflects microwave radiation whenever the resonant frequency or the Q of the cavity is changed by absorption in the material.

The instrument used in the present dissertation research is a Bruker EMX spectrometer with an Oxford Instruments helium gas flow cryostat for temperature control down to 4.2 K. This electron paramagnetic resonance spectrometer operates in the microwave X band ($8 - 12$ GHz), and detects transitions via reflections from a resonant microwave cavity. These reflections are detected and recorded while sweeping the magnitude of an applied magnetic field across a specified range to generate electron paramagnetic resonance spectra.

3.1 Microwave Bridge and Cavity

Microwaves are produced, detected, and controlled by a collection of components referred to as the microwave bridge. A schematic of a microwave bridge is shown in Figure 3. The source is a solid-state Gunn diode which excites resonant microwave frequencies within a tunable source cavity. The microwaves are coupled into a wave-guide which guides the microwaves to a splitter. At this point, part of the microwave radiation is guided along a reference arm, and part is guided to the microwave cavity. The reference arm is composed of an attenuator and a phase shifter and serves as a means to bias the detector diode. Biasing the detector diode is necessary to ensure that it operates in a linear mode (i.e., a relative change in microwave power leads to the same relative change in signal). The attenuator in the reference arm is adjusted to create the desired amount of bias in the detector diode and the phase shifter is adjusted to match the phase of the reference arm microwaves to the phase of the microwaves reflected from the cavity.

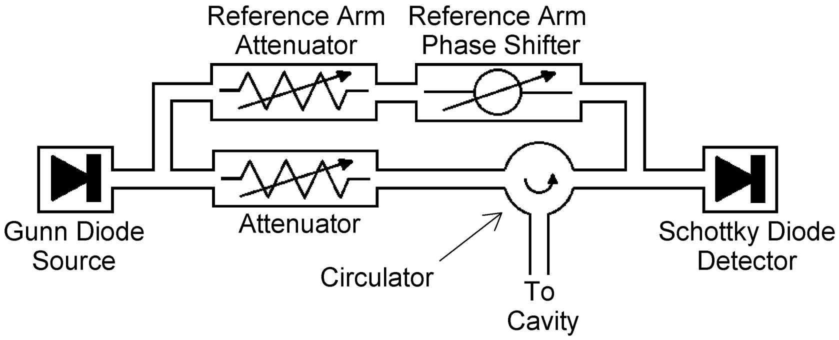

Figure 3. Schematic of a microwave bridge.

Microwaves that are directed to the cavity first go through an attenuator which varies the power of the microwaves according to the needs of the experiment, then to a circulator which guides the microwaves to the cavity. To achieve maximum sensitivity, the microwaves are critically coupled into the cavity. This means that almost all of the microwave energy enters the cavity independent of the incident amount of energy. This critical coupling is achieved by inserting or withdrawing a teflon screw with a small piece of metal on the tip in front of the cavity's iris (Figure 4). Once inside the cavity, the microwaves form a standing wave pattern. Figure 5 shows the magnetic and electric fields of the standing wave pattern in a circular cavity. Since magnetic moments in the sample interact with the magnetic field of the standing wave, the cavity is designed to place the magnetic field maximum of the microwaves at the location of the sample. In Figure 5, the sample is inserted into the cavity through an access hole in the top. The cavity is positioned within the gap of the electromagnet such that the magnetic field of the microwaves is normal to the applied magnetic field generated by the electromagnet.

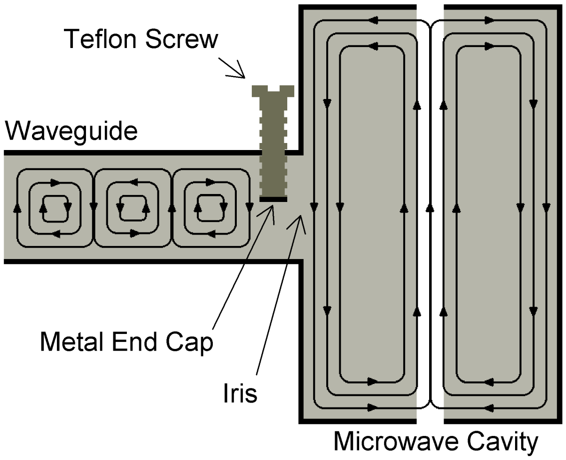

Figure 4. Schematic of microwave energy coupling into a resonant cavity.

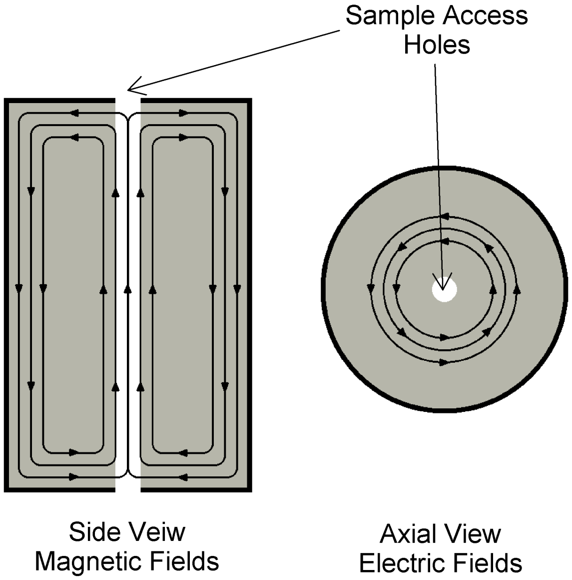

Figure 5. Schematic showing magnetic fields in a side view and electric fields in an axial view within a cylindrical resonant cavity.

Microwaves are reflected from the cavity whenever the resonant frequency or the Q of the cavity is changed by absorption of microwaves in the sample under study. Reflected microwaves go back to the circulator which guides these microwaves to the detector diode. The detector is a Schottky diode that generates a signal when microwaves are incident. This detector signal is measured by a lock-in amplifier which requires the signal to be modulated. Since the intensity of the reflected microwaves is a function of magnetic field, modulation of the detector signal is accomplished by adding a small modulation to the applied magnetic field. This modulates the intensity of the microwaves incident upon the detector diode creating a modulated signal. The small modulation in the applied magnetic field is generated by a set of coils that are embedded in the sides of the microwave cavity. The modulation frequency is typically 100 kHz. The lock-in amplifier mixes and averages the detector signal with a single-frequency reference signal to produce another signal that is proportional to the modulation amplitude of the detector signal. This signal is at a maximum whenever the diode signal and reference signal have the same phase. This method filters out noise that has a frequency or phase that differs from that of the reference signal. This "filtered" signal and the averaging increase the signal-to-noise ratio of the spectrometer. Since the detector signal is modulated by applying a small modulation to the applied magnetic field and the microwave power reflected by the microwave cavity is a function of applied magnetic field, the signal produced by the lock-in amplifier is proportional to the first derivative (slope) of the microwave power reflected from the microwave cavity (Figure 6).

The electron paramagnetic resonance spectrometer at the Air Force Institute of Technology is capable of detecting as few as 5×10^{10} unpaired spins at 10 K [37]. Knowing this sensitivity, the concentration of paramagnetic defects present in the sample can be estimated with

$$(5 \times 10^{10})(\Delta B)^2(SN)(NL)(T/10)(1/V) \tag{51}$$

where ΔB is the line-width of the spectrum in Gauss, SN is the signal to noise ratio, NL is the number of lines associated with the resonance, T is the temperature in Kelvin, and V is the volume of the sample in cm^3 [37].

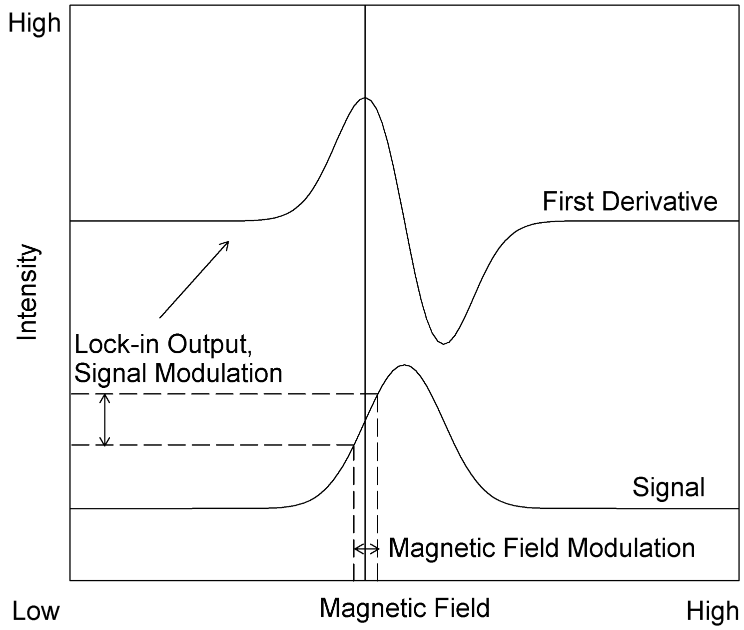

Figure 6. Figure illustrating the effects of modulating the magnetic field of a magnetic-field-dependent signal. The modulation amplitude of a magnetic-field-dependent signal is proportional to the slope of the signal. When this modulation is measured by a lock-in amplifier, the output is proportional to the first derivative of the signal.

3.2 Magnetic Field Measurements and Calibration

The applied magnetic field from the electromagnet is measured with a Hall probe when collecting a spectrum, and with a teslameter and calibration sample when performing precise measurements of the magnetic field at an electron paramagnetic resonance line. The Hall probe has a quick response time, but is prone to direct-current drift, since it relies on an applied voltage, and is dependent on the magnetic field direction. Therefore, it is more suitable for controlling the applied magnetic field when sweeping the applied magnetic field during the measurement of a spectrum. The teslameter is a more precise instrument since it relies on the principles of nuclear magnetic resonance, but has a slow response time. It's measurement of the magnetic field is independent of the magnetic field direction. Therefore, it is more suitable for precise measurement of the magnetic field when measuring the magnetic field necessary to observe an electron paramagnetic resonance line.

The Hall probe makes use of the Hall effect to measure the applied magnetic field. The Hall effect is the creation of an electric potential in an electrically conducting material due to the presence of applied electric and magnetic fields. This electric potential is proportional to the product of the applied electric field, applied magnetic field, and the sine of the angle between them. The proportionality constant is a function of several variables including the conductivity and shape of the electrically conducting material. If the applied electric field is held constant, the magnitude of the applied magnetic field can be measured. The Hall probe is mounted on one side of the electromagnet's gap. Because of this, the difference between the magnetic field measured by the Hall probe and the magnetic field at the sample can be on the order of 1 mT.

After completing a sweep, the Hall probe is used to set the electromagnet at a magnetic field where a resonance was detected. The teslameter is then used to make a precise measurement of the magnetic field. The teslameter measures the transition energy of the nuclear magnetic resonance of protons. As seen in Section 2.3, this energy is proportional to the magnitude of the magnetic field. The teslameter probe is in the form of a long rod. Within the tip of the rod is a material that contains protons and a radio frequency coil for excitation and detection of the nuclear magnetic resonance. The tip of this rod can be placed next to the cavity to get a closer measurement of the magnetic field at the sample, but can still differ on the order of 0.01 mT. Because of this, a calibration sample with a known electron paramagnetic resonance line is used to correct the magnetic field measurement.

Assuming that the teslameter will measure a magnetic field of zero when the magnetic field at the sample is zero and that the correlation is linear, the calibrated magnetic field is

$$\frac{h\nu_{cal}}{g_{cal}\mu_B B_{cal}}B \tag{52}$$

where ν_{cal} is the microwave frequency and B_{cal} is the magnetic field at which the calibration sample's known electron paramagnetic resonance line is detected, g_{cal} is the g factor of the calibration sample's known electron paramagnetic resonance line, and B is the uncorrected magnetic field. Both of the magnetic fields in this equation are measured with the teslameter, and with the calibration sample and experimental sample in the same physical setup. The calibration sample used in this research is a single crystal of magnesium oxide that has been doped with chromium. Chromium Cr^{3+} substitutes for magnesium Mg^{2+} and creates a paramagnetic defect that has an isotropic g matrix with a principal value of 1.9800 [38].

IV. Nitrogen Substitutional Impurity in Zinc Oxide (ZnO)

Nitrogen substitutes for oxygen in zinc oxide and forms an optically active acceptor. Figure 7 shows a nitrogen ion substituting for an oxygen ion in the zinc oxide structure (see Appendix B). The nitrogen has four nearest-neighbor zinc ions (one axial and three basal) and twelve neighboring oxygen ions (divided into three sets of 3, 6 and 3 with the middle set of 6 sightly more distant from the nitrogen than the upper and lower sets of 3). In n-type material, nitrogen acceptors are normally in the singly ionized charge state with no unpaired electrons and no electron paramagnetic resonance signal. However, when these samples are illuminated at low temperature with near-band-edge laser light, a portion of the singly ionized nitrogens are converted to the neutral charge state, and thus become paramagnetic. Using bulk n-type zinc oxide crystals, Carlos *et al.* [39] and Garces *et al.* [40] were the first to identify the photoinduced electron paramagnetic resonance spectrum from neutral nitrogen acceptors. As expected, the spectrum is uniquely distinguished by a well-resolved three-line ^{14}N hyperfine pattern. This neutral nitrogen acceptor spectrum is also seen in powder and polycrystalline zinc oxide [41, 42]. Recent investigations [42, 43, 44] show that prominent forbidden lines appearing in the electron paramagnetic resonance spectrum are due to a ^{14}N nuclear electric quadrupole interaction.

The question as to whether an isolated nitrogen is a deep or shallow acceptor in zinc oxide has received considerable attention in recent years. Advanced first-principles calculations [45, 46, 47, 48] have suggested that nitrogen is a deep acceptor with an ionization energy approaching 1.3 eV. On the experimental side, the wavelength dependence of the photo-conversion of singly ionized nitrogen acceptors to the neutral charge state has an onset near 2.0 eV and provides evidence that nitrogen is a deep acceptor in zinc oxide [44]. Additional support for the deep acceptor model of nitrogen comes from the observation of a broad photoluminescence band peaking near 730 nm in nitrogen-doped bulk crystals [49]. In contrast, a donor-acceptor pair peak is observed in photoluminescence studies of nitrogen-doped zinc oxide epitaxial layers and is assigned to a shallow-donor to shallow-acceptor transition with an acceptor

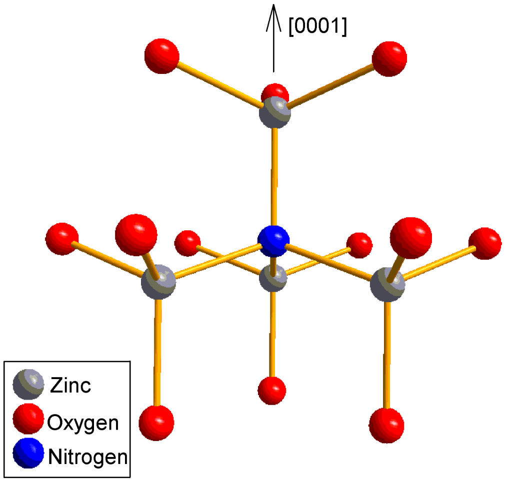

Figure 7. Schematic of the crystal structure of zinc oxide as seen along the $[10\bar{1}0]$ direction. A nitrogen substitutes for an oxygen and has four neighboring zinc cations and twelve neighboring oxygen anions.

binding energy of around 160 meV and a donor binding energy near 60 meV [50]. It is not known if the participating shallow acceptor is an isolated nitrogen or a larger complex involving one or more nitrogen ions. The important point, however, is that these donor-acceptor pair results [50] show shallow acceptors are formed in zinc oxide by nitrogen doping. The conflicting nature of the reports thus far suggests a need for additional fundamental studies of nitrogen-doped zinc oxide.

In this dissertation, electron paramagnetic resonance spectroscopy is used to investigate the ^{67}Zn hyperfine interactions associated with the neutral nitrogen acceptor in zinc oxide. These results have been recently published in the Journal of Applied Physics [51]. Sets of less intense ^{67}Zn (4.1% natural abundance [3]) hyperfine lines are observed around each of the primary ^{14}N (99.6% natural abundance [3]) hyperfine lines in the photoinduced spectra taken at 5 K (using 442 or 633 nm laser light). They are assigned to axial and basal ^{67}Zn nearest neighbors. Principal values and principal-axis directions of the ^{67}Zn hyperfine matrices are obtained from the angular dependence of the electron paramagnetic resonance spectra. These spin-Hamiltonian parameters provide information about the distribution of the unpaired spin at the zinc neighbors. Comparing the experimentally determined ^{67}Zn and ^{14}N

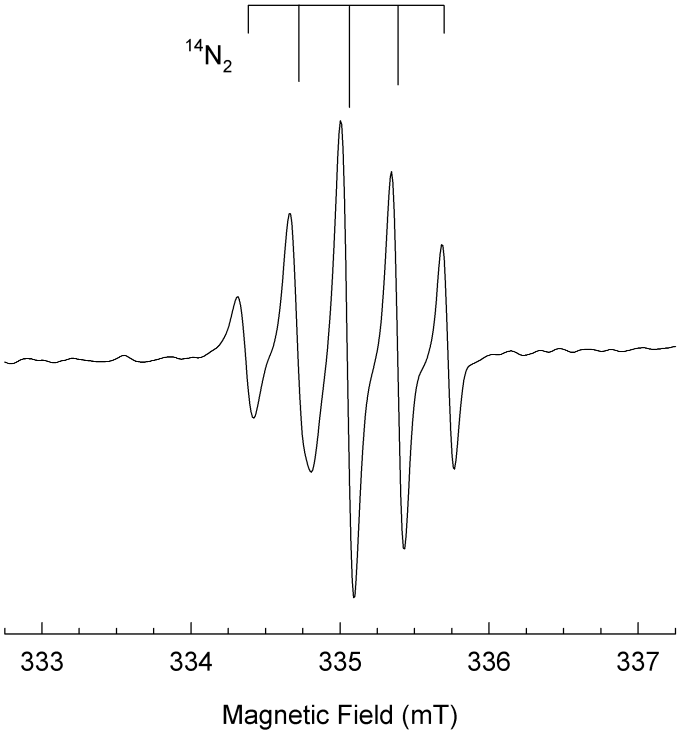

Figure 8. Electron paramagnetic resonance spectrum of the singly ionized molecular nitrogen acceptor N_2^- in zinc oxide with the magnetic field along the [0001] direction. The data were recorded from a nitrogen-doped sample at a microwave frequency of 9.3957 GHz and a temperature of 26 K.

hyperfine parameters with values predicted by density functional theory calculations is expected to provide a check on the validity of the deep acceptor model of nitrogen substituting for oxygen in zinc oxide with no nearby perturbations [42, 52, 53].

The bulk zinc oxide crystal used in the present investigation was cut from a larger boule grown at Eagle-Picher (Miami, OK) by the seeded chemical vapor transport method with nitrogen added to the gas stream. Material from this boule was used in a previous study [54] where the molecular nitrogen acceptor was studied. The electron paramagnetic resonance spectrum of the molecular nitrogen acceptor is detected in the sample used in this investigation and is shown in Figure 8. The as-grown boule appeared yellow and Hall measurements at room temperature verified that it was n-type. In addition to the usual shallow donor signal, electron paramagnetic resonance spectroscopy showed that Fe^{3+} ($3d^5$) ions were present before illumination

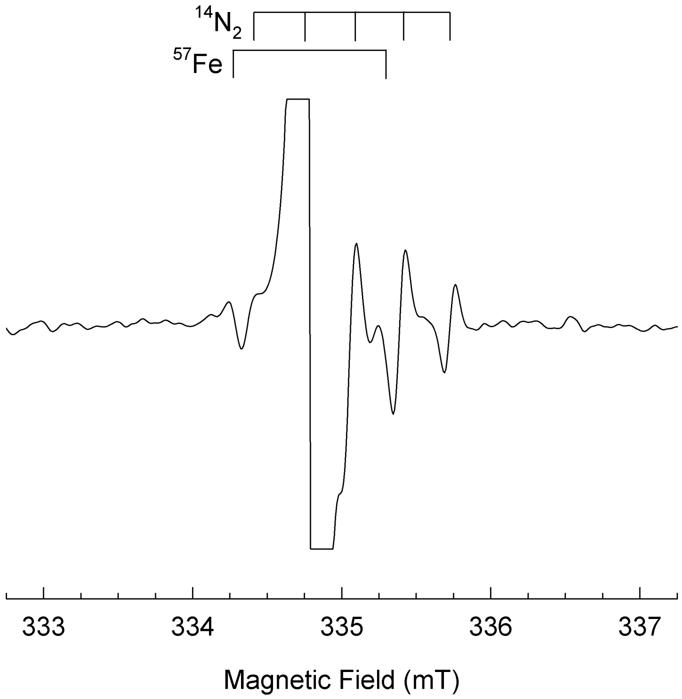

Figure 9. Electron paramagnetic resonance spectrum of the singly ionized iron donor Fe^{3+} ($3d^5$) in zinc oxide with the magnetic field along the [0001] direction. The data were recorded from a nitrogen-doped sample at a microwave frequency of 9.3957 GHz and a temperature of 26 K. The spectrum of the iron donor is detected when the phase of the lock-in amplifier is 90° from the phase necessary to detect the spectra of the nitrogen acceptors and the shallow donor.

at low temperature. The electron paramagnetic resonance spectrum of the iron donor is detected in the sample used in this investigation and is shown in Figure 9. These singly ionized iron donors act as electron traps when electrons are pumped away from the nitrogen acceptors by near-band-edge laser illumination. Dimensions of the sample are approximately $3 \times 3 \times 1$ mm^3.

Helium-cadmium (442 nm) and helium-neon (633 nm) lasers were separately used to successfully convert the nitrogen acceptors from the singly ionized charge state to the paramagnetic neutral charge state at low temperature. The laser light moves electrons from the valence band or singly ionized acceptors to shallow donors and deeper iron donors, where they remain stably trapped as long as the temperature is kept below about 100 K. From the intensities of the electron paramagnetic resonance signals, the largest concentration of neutral nitrogen acceptors photoinduced in the sample is estimated to be approximately 8.0×10^{15} cm^{-3}.

4.1 Results

Figure 10 shows the well-resolved and unique sets of three lines that characterize the electron paramagnetic resonance spectra from isolated neutral nitrogen acceptors in zinc oxide [39, 40, 41, 42, 43, 44]. The magnetic field is along the [0001] direction in Figure 10(a) and is in the basal plane along the $[10\bar{1}0]$ direction in Figure 10(b). Both spectra were taken at 5 K after exposure at this temperature to 442 nm laser light (633 nm laser light produced the same spectra). At temperatures above approximately 9 K, these electron paramagnetic resonance lines broaden beyond recognition because of short spin-lattice relaxation times. The set of three lines is the result of a hyperfine interaction between an unpaired electron and a ^{14}N nucleus (99.6% natural abundance [3] with $I = 1$ [4]).

Well-resolved hyperfine lines from ^{67}Zn nearest neighbors are easily observed in the electron paramagnetic resonance spectrum of the neutral nitrogen acceptor. These ^{67}Zn nuclei have a natural abundance of 4.1% [3] and have $I = \frac{5}{2}$ [4]. Because of this low natural abundance, the ^{67}Zn hyperfine lines are much smaller in intensity than the primary ^{14}N hyperfine lines in Figure 10 (the ^{67}Zn hyperfine lines are approximately 140 times smaller than the ^{14}N hyperfine lines). Figure 11 shows these weaker hyperfine lines in an electron paramagnetic resonance spectrum taken at 5 K after illuminating the sample at this temperature with 442 nm laser light. The magnetic field is along the [0001] direction and the microwave frequency is 9.3973 GHz. Compared to Figure 10(a) the vertical scale is expanded to show the symmetrical sets of hyperfine lines. A nitrogen substituting for an oxygen has one zinc neighbor along the c axis and three zinc neighbors forming a basal plane (see Appendix B). With the magnetic field along the [0001] direction, the axial zinc neighbor gives rise to a nondegenerate electron paramagnetic resonance spectrum, while the basal zinc neighbors give rise to a triply degenerate electron paramagnetic resonance spectrum.

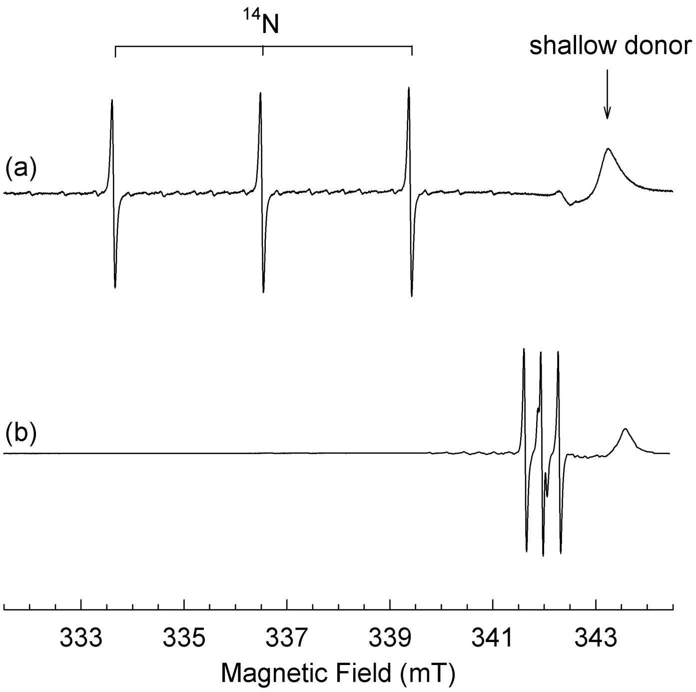

Figure 10. Electron paramagnetic resonance spectra of the neutral nitrogen acceptor N^0 in zinc oxide with the magnetic field (a) along the [0001] direction and (b) in the basal plane along the $[10\bar{1}0]$ direction. The spectra were recorded at a frequency of 9.3958 GHz and a temperature of 5 K. The spectra are photoinduced with 442 nm laser light from a cw HeCd laser.

This makes the basal ^{67}Zn hyperfine lines in the electron paramagnetic resonance spectrum three times more intense than the axial ^{67}Zn hyperfine lines. In Figure 11, the separation of adjacent axial lines is 1.3 mT and the separation of adjacent basal lines is 0.7 mT. Stick diagrams above the spectrum in Figure 11 identify the axial (red) and basal (blue) ^{67}Zn hyperfine lines that surround each of the three off-scale ^{14}N hyperfine lines.

The electron paramagnetic resonance lines in Figure 10(a) shift to higher field, but do not split, as the magnetic field is rotated from the [0001] direction to the basal plane. Forbidden transitions arising from the ^{14}N nuclear electric quadrupole interaction begin to appear between the allowed lines when the magnetic field is approximately 60° away from the [0001] direction [44]. These forbidden transitions are most intense when the field is about 86° from the [0001] direction (allowed and

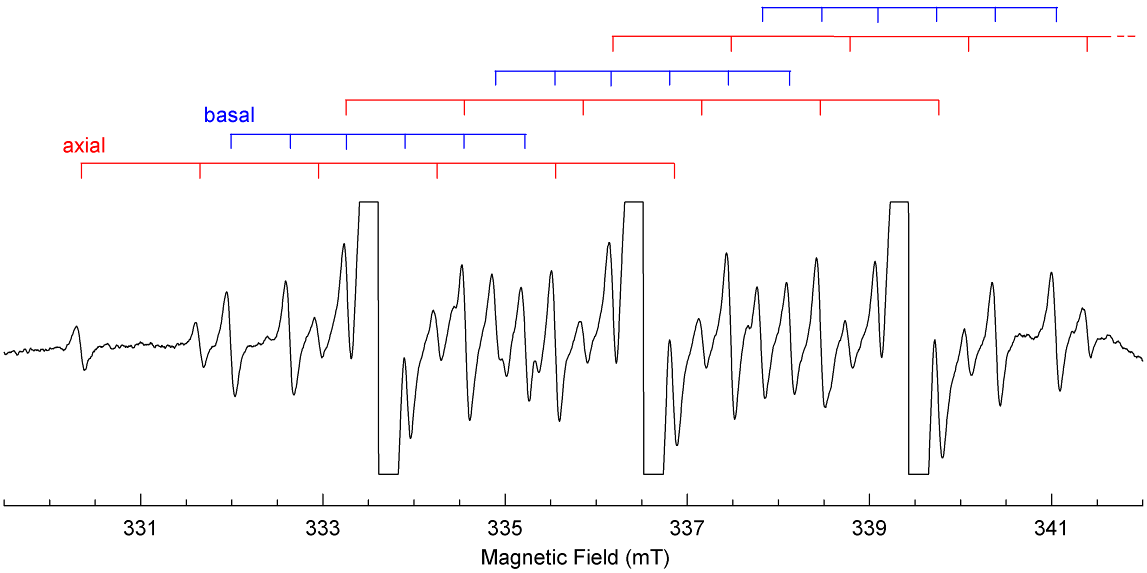

Figure 11. ^{67}Zn hyperfine lines in the electron paramagnetic resonance spectrum of the neutral nitrogen acceptor with the magnetic field along the [0001] direction. The data were recorded at a microwave frequency of 9.3973 GHz and a temperature of 5 K. The spectrum is photoinduced with 442 nm laser light from a cw HeCd laser. Stick diagrams show the axial (red) and basal (blue) ^{67}Zn hyperfine lines that surround each of the three large (off-scale) ^{14}N hyperfine lines.

forbidden lines have similar intensities near this direction). Two forbidden lines are still present, but less noticeable, when the field is in the basal plane. In Figure 10(b), these forbidden transitions are observed on either side of the middle allowed ^{14}N hyperfine line.

In Figure 11, there are three well-resolved axial ^{67}Zn hyperfine lines in the field region below the ^{14}N hyperfine line at 333.6 mT. These three hyperfine lines move closer to the ^{14}N hyperfine line as the magnetic field is rotated from the [0001] direction toward the [$10\bar{1}0$] direction and no splitting into components is detected. The same behavior occurs when the field is rotated from the [0001] direction toward the [$2\bar{1}\bar{1}0$] direction. These low-field axial ^{67}Zn hyperfine lines are accurately identified and measured only during the first 40° of rotation from the [0001] direction. Beyond this angle, basal ^{67}Zn hyperfine lines begin to interfere. The axial ^{67}Zn hyperfine lines extend out farther from the low-field ^{14}N hyperfine line than the basal ^{67}Zn hyperfine lines when the magnetic field is along the [0001] direction (as seen in Figure

11). However, as the magnetic field is rotated from the [0001] direction toward the basal plane, this ordering reverses for angles beyond 40°. For angles greater than 40°, the basal ^{67}Zn hyperfine lines extend farther out from the ^{14}N hyperfine line than the axial ^{67}Zn hyperfine lines. In the basal plane, the axial ^{67}Zn hyperfine lines are completely obscured by the inner basal ^{67}Zn hyperfine lines. This interference from basal ^{67}Zn hyperfine lines limits the range where the axial ^{67}Zn hyperfine lines can be measured (and thus accounts for the lack of data points beyond 40° in Figure 12). Fortunately, the experimental results obtained from the first 40° of rotation are sufficient to determine the axial ^{67}Zn hyperfine parameters, as described in Section 4.2. The experimental positions of these axial ^{67}Zn hyperfine lines are plotted as discrete points in Figure 12.

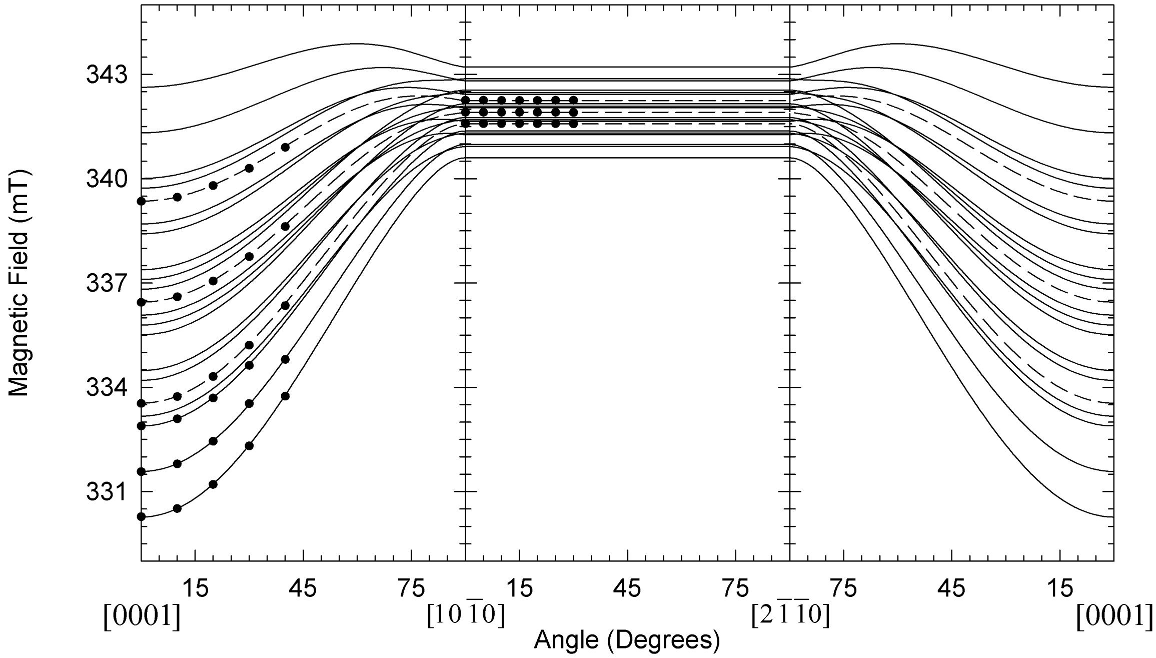

Figure 12. Angular dependence of the axial ^{67}Zn hyperfine lines. Solid and dashed lines are calculated at 9.395 GHz using the spin Hamiltonian parameters in Table 2. Black dots are experimental data recorded at 5 K and scaled to 9.395 GHz. Solid lines represent ^{67}Zn hyperfine interactions and dashed lines represent ^{14}N hyperfine interactions.

In Figure 11 there are three well-resolved basal ^{67}Zn hyperfine lines in the field region below the ^{14}N hyperfine line at 333.6 mT. The lowest-field basal ^{67}Zn hyperfine line maintains the same spacing from the ^{14}N hyperfine line for the first 30° of rotation of the magnetic field away from the [0001] direction toward the $[10\bar{1}0]$ direction. Only a slight broadening, but no splitting into components is observed during this rotation of the magnetic field. Continued rotation causes this lowest-field basal ^{67}Zn hyperfine line to split into two components. When the magnetic field reaches the basal plane, the two components that emerged from the original hyperfine line are well separated and easily seen. Unlike the case of the axial neighbor, electron paramagnetic resonance spectra taken in the basal plane provide detailed information about the basal ^{67}Zn hyperfine interactions. Figure 13 shows two of these spectra obtained at 5 K and a microwave frequency of 9.3951 GHz after illuminating the crystal with 442 nm laser light. Only the low-field sides of the spectra are shown in Figure 13 because the shallow donor spectrum interferes with the high-field sides of the spectra. The magnetic field is along the $[10\bar{1}0]$ direction in Figure 13(a) and along the $[2\bar{1}\bar{1}0]$ direction in Figure 13(b). Interference from the axial ^{67}Zn hyperfine lines is not a problem in the basal plane because the basal ^{67}Zn hyperfine lines extend farther from the ^{14}N hyperfine lines than the axial ^{67}Zn hyperfine lines. Also, in the basal plane, the basal ^{67}Zn hyperfine spacings are larger than the ^{14}N hyperfine spacings. This makes it easy to identify individual basal ^{67}Zn hyperfine lines on the low-field side of the spectra in Figure 13, because they appear as sets of three lines that mimic the spacing of the three ^{14}N hyperfine lines. The lowest-field three-line sets are identified by stick diagrams in Figure 13.

When the magnetic field is along either the $[10\bar{1}0]$ or $[2\bar{1}\bar{1}0]$ directions, two of the three zinc ions in the basal plane have equivalent hyperfine interactions. Thus, there are two sets of basal ^{67}Zn hyperfine lines for these directions of magnetic field, with one set twice as intense as the other set. In Figure 13, basal ^{67}Zn hyperfine lines from a doubly-degenerate set are labeled "double" and lines from a nondegenerate set are labeled "single." A single set of three lines (representing the interaction with one zinc nucleus) is lowest in field in Figure 13(a) with the lowest line in this set of three located at 339.7 mT. The lowest line of the double set is located at 340.1 mT

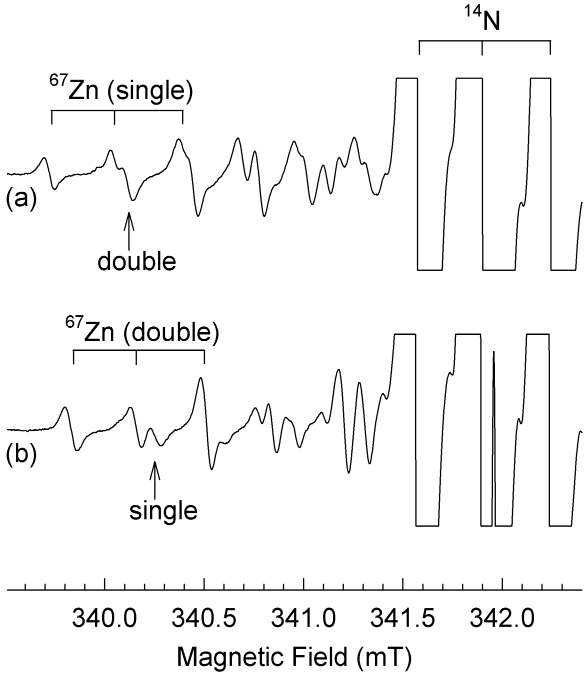

Figure 13. Low-field ^{67}Zn hyperfine lines in the electron paramagnetic resonance spectrum of the neutral nitrogen acceptor with the magnetic field in the basal plane. The data were recorded at a microwave frequency of 9.3949 GHz and a temperature of 5 K. The spectra are photoinduced with 442 nm laser light from a cw HeCd laser. (a) The magnetic field is along the $[10\bar{1}0]$ direction. (b) The magnetic field is along the $[2\bar{1}\bar{1}0]$ direction.

in Figure 13(a). The ordering is reversed in Figure 13(b) for the other orientation of magnetic field in the basal plane. The double set of three lines (representing the interaction with two equivalent zinc nuclei) is now lowest in magnetic field with the lowest line in this set of three located at 339.8 mT. The lowest line of the single set is at 340.3 mT in Figure 13(b).

During a 30° rotation of the magnetic field from the $[10\bar{1}0]$ direction to the $[2\bar{1}\bar{1}0]$ direction in the basal plane, the single set in Figure 13(a) moves to higher field until it merges with another set to form the double set in Figure 13(b). From the perspective of a single basal ^{67}Zn nucleus, this represents rotation angles of $0° - 30°$ from the $[10\bar{1}0]$ direction. The double set in Figure 13(a) splits into two sets with one set moving to lower field and the other moving to higher field. The set that travels to lower field merges with the single set in Figure 13(a) to form the double set in

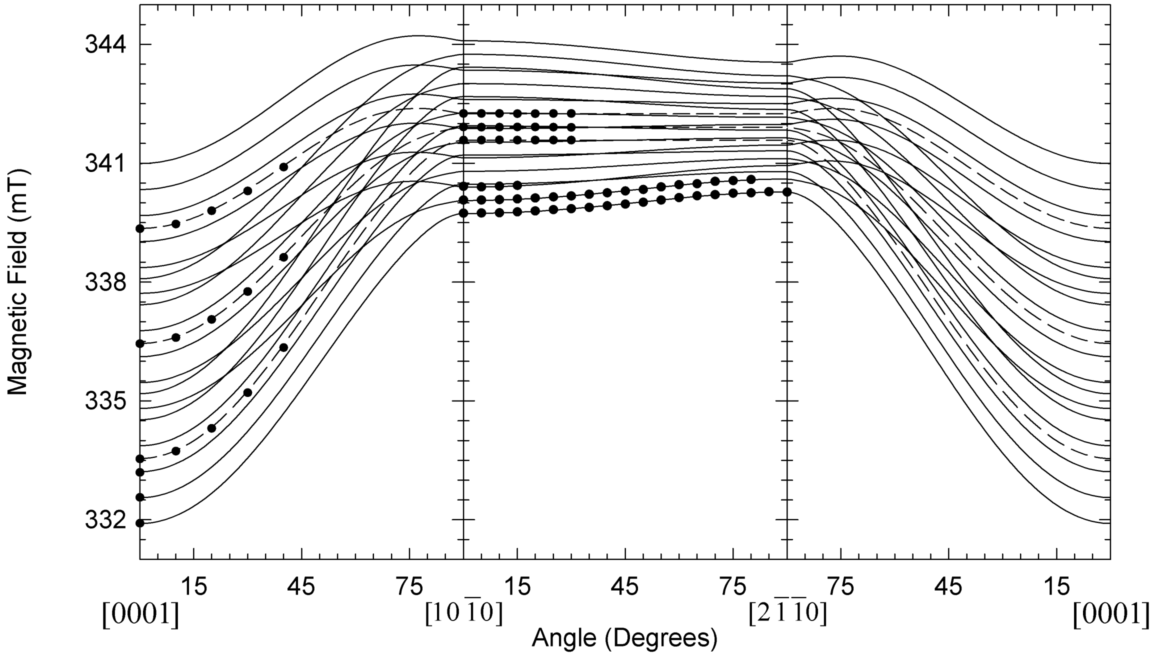

Figure 14. Angular dependence of the basal ^{67}Zn hyperfine lines. Solid and dashed lines are calculated at 9.395 GHz using the spin Hamiltonian parameters in Table 2. Black dots are experimental data recorded at 5 K and scaled to 9.395 GHz. Solid lines represent ^{67}Zn hyperfine interactions and dashed lines represent ^{14}N hyperfine interactions.

Figure 13(b). From the perspective of a single basal ^{67}Zn nucleus, this represents rotation angles of $60° - 30°$ from the $[10\bar{1}0]$ direction. The set that travels to higher field becomes the single set in Figure 13(b). From the perspective of a single basal ^{67}Zn nucleus, this represents rotation angles of $60° - 90°$ from the $[10\bar{1}0]$ direction. Therefore, data for 90° of magnetic field rotation for a single basal ^{67}Zn hyperfine line are obtained with 30° of actual rotation in the basal plane. The experimental positions of these low-field basal ^{67}Zn hyperfine lines are plotted as discrete points in Figure 14.

4.2 Spin-Hamiltonian Analysis

Spin-Hamiltonian parameters describing the axial and basal ^{67}Zn hyperfine interaction matrices are obtained from the angular dependence of the ^{67}Zn hyperfine lines. The width of each electron paramagnetic resonance line is about 0.1 mT. This gives a minimum estimated error for the g parameters of ±0.0006, and for the hyperfine interaction parameters of ±0.6 MHz. For many directions of magnetic field, the majority of the hyperfine lines are strongly overlapping and it is difficult to make specific assignments and extract useful information. Fortunately, as described in Section 4.1, there are angles where subsets of ^{67}Zn hyperfine lines on the low field side of the electron paramagnetic resonance spectra can be assigned to specific transitions and used to determine precise values of the parameters. In the following analysis of the nitrogen electron paramagnetic resonance spectra, the focus is placed on these low field ^{67}Zn hyperfine lines to determine the ^{67}Zn hyperfine interaction parameters. Because of this it is first necessary to determine the g parameters and ^{14}N hyperfine interaction parameters from the angular dependence of the ^{14}N hyperfine lines.

Parameters for the g matrix, the ^{14}N hyperfine interaction matrix, and the ^{14}N nuclear electric quadrupole interaction matrix have been independently determined by several groups [39, 40, 42, 43, 44]. Their findings show that the g matrix, ^{14}N hyperfine interaction matrix, and ^{14}N nuclear electric quadrupole interaction matrix are axial with the unique direction along the [0001] direction. A summary of their parameters is listed in Table 1.

Table 1. Spin-Hamiltonian parameters for the ^{14}N hyperfine interaction of the neutral nitrogen acceptor in zinc oxide from previous studies. The hyperfine and nuclear electric quadrupole interaction parameters are in terms of h and are in units of MHz.

Reference	$g_{\perp}$	$g_{\|\|}$	$A_{\perp}$	$A_{\|\|}$	e^2qQ/h
Carlos *et al.*[39]	1.9633	1.9953	9.9	82.5	-
Garces *et al.*[40]	1.9632	1.9948	9.5	81.3	-
Gallino *et al.*[42]	1.9630	1.9947	8.6	81.3	2.65
Evans [43]	1.9631	1.9949	7.95	81.26	2.95
Stehr *et al.*[44]	1.963	1.995	8.5	81.1	2.95

The spin Hamiltonian

$$\hat{H}_s = \mu_B \hat{\mathbf{S}} \cdot \mathbf{g} \cdot \mathbf{B} + \hat{\mathbf{I}} \cdot \mathbf{Q} \cdot \hat{\mathbf{I}} + \hat{\mathbf{S}} \cdot \mathbf{A} \cdot \hat{\mathbf{I}} - g_{\mathrm{N}} \mu_N \hat{\mathbf{I}} \cdot \mathbf{B}, \tag{53}$$

where g_N is the g factor for ^{14}N and is known to be 0.40375 [4], describes the angular dependence of the ^{14}N hyperfine lines and is fitted to the ^{14}N hyperfine data presented in Figures 12 and 14 and included in Appendix E. The results of a least-squares fitting routine are g parameters of 1.9632 and 1.9951, and hyperfine interaction parameters of 8.0 MHz and 81.1 MHz for principal axes in the basal plane and along the [0001] direction, respectively. The standard deviation of the frequency data from the fit is 121 kHz. This standard deviation translates into an estimated error for the g parameters of ±0.00003, and for the hyperfine interaction parameters of ±0.2 MHz. These estimates are within the minimum estimates. The nuclear electric quadrupole interaction parameters of Evans [43] were used in the fitting routine. Gallino *et al.* [42] determined that the signs of the hyperfine interaction parameters are opposite. The hyperfine interaction parameter along the [0001] direction is assigned a positive sign because the nuclear magnetic moment for ^{14}N is positive. From experiment [43, 44], the positions of forbidden lines between the middle and highest field ^{14}N hyperfine lines require the signs of the hyperfine interaction parameter in the basal plane and the nuclear electric quadrupole interaction parameter along the [0001] direction to have opposite signs. These parameters are used in the ^{67}Zn spin Hamiltonian to extract the ^{67}Zn hyperfine interaction parameters, and are included in Table 2.

The observation of a maximum hyperfine splitting along the [0001] direction in two planes of rotation for the axial ^{67}Zn hyperfine lines establishes this direction as a principal axis direction. These hyperfine lines are also observed to be very close to axial with the unique direction along the [0001] direction. Using these principal-axis directions, the spin Hamiltonian

$$\hat{H}_s = \mu_B \hat{\mathbf{S}} \cdot \mathbf{g} \cdot \mathbf{B} + \hat{\mathbf{I}} \cdot \mathbf{Q} \cdot \hat{\mathbf{I}} + \sum_{n=\{\mathrm{N},\mathrm{Zn}\}} \left(\hat{\mathbf{S}} \cdot \mathbf{A}^{(n)} \cdot \hat{\mathbf{I}}^{(n)} - g_n \mu_N \hat{\mathbf{I}}^{(n)} \cdot \mathbf{B} \right), \tag{54}$$

where g_{Zn} is the g factor for ^{67}Zn and is known to be 0.35024 [4], describes the angular dependence of the ^{67}Zn hyperfine lines and is fitted to the axial ^{67}Zn hyperfine data presented in Figure 12 and included in Appendix E. The spin Hamiltonian in

Equation 54 is the same as in Equation 53 except terms have been added for the ^{67}Zn hyperfine interactions. The results of a least-squares fitting routine results in hyperfine interaction parameters of 10.7 MHz and 36.6 MHz for principal axes in the basal plane and along the [0001] direction, respectively. The standard deviation of the frequency data from the fit is 431 kHz. This standard deviation translates into an estimated error of ±0.9 MHz. This estimate is slightly larger than the minimum estimate. A plot of the axial ^{67}Zn hyperfine lines is shown in Figure 12 for three planes of rotation. These parameters are included in Table 2.

Table 2. Spin-Hamiltonian parameters for the neutral nitrogen acceptor in zinc oxide. The nuclear electric quadrupole interaction parameters are from Evans [43]. The hyperfine and nuclear electric quadrupole interaction parameters are in terms of h and are in units of MHz. The estimated error in the g parameters is ±0.0006 and in the hyperfine interaction parameters is ±1 MHz.

Parameter	Principal Value	Principal-Axis Direction
g parameters		
$g_\perp$	1.9632	-
$g_{\|\|}$	1.9951	[0001]
Hyperfine interaction parameters for ^{14}N		
$A_\perp$	-8.0	-
$A_{\|\|}$	81.1	[0001]
Nuclear electric quadrupole interaction parameters for ^{14}N		
$Q_\perp$	-1.5	-
$Q_{\|\|}$	3.0	[0001]
Hyperfine interaction parameters for axial ^{67}Zn		
$\lvert A_\perp\rvert$	10.7	-
$\lvert A_{\|\|}\rvert$	36.6	[0001]
Hyperfine interaction parameters for basal ^{67}Zn		
$\lvert A_1\rvert$	14.3	$[\bar{1}2\bar{1}0]$
$\lvert A_2\rvert$	18.3	[0001]
$\lvert A_3\rvert$	20.3	$[10\bar{1}0]$

As seen in Figures 13(a) and 14, the lowest-field (single) basal ^{67}Zn hyperfine line has a turning point along the $[10\bar{1}0]$ direction. This suggests that a principal axis of the basal ^{67}Zn hyperfine interaction matrix is along this direction. Rotation of the magnetic field from the $[10\bar{1}0]$ direction toward the [0001] direction provides further verification that $[10\bar{1}0]$ is a principal-axis direction. In this second plane of rotation, the lowest-field basal ^{67}Zn hyperfine line also has a turning point when the magnetic field is along the $[10\bar{1}0]$ direction. The crystal lattice of zinc oxide has C_{6v} symmetry. This symmetry has a six-fold rotation axis along the [0001] direction, three $\{10\bar{1}0\}$ mirror planes and three $\{2\bar{1}\bar{1}0\}$ mirror planes in zinc oxide. Due to this symmetry, any deviation of the remaining principal axes from the [0001] or $[\bar{1}2\bar{1}0]$ (normal to $[10\bar{1}0]$) directions will cause additional splitting of the basal ^{67}Zn hyperfine lines. Therefore, principal axes of the basal ^{67}Zn hyperfine interaction matrix must be along the [0001] and $[\bar{1}2\bar{1}0]$ directions, because additional splitting of the basal ^{67}Zn hyperfine lines is not observed. Using these principal-axis directions, the spin Hamiltonian in Equation (54) is fitted to the basal ^{67}Zn hyperfine data presented in Figure 14 and included in Appendix E. The results of a least-squares fitting routine are hyperfine interaction parameters of 14.3 MHz, 18.3 MHz, and 20.3 MHz for principal axes along the $[\bar{1}2\bar{1}0]$, [0001], and $[10\bar{1}0]$ directions, respectively. The standard deviation of the frequency data from the fit is 198 kHz. This standard deviation translates into an estimated error of ±0.4 MHz. This estimate is within the minimum estimate. A plot of the basal ^{67}Zn hyperfine lines is shown in Figure 14 for three planes of rotation. These parameters are included in Table 2.

4.3 Discussion

Figure 15 is a schematic representation of the neutral nitrogen acceptor in zinc oxide. The axial zinc neighbor and one basal zinc neighbor are shown. Two of the principal-axis directions of the basal ^{67}Zn hyperfine interaction matrix are in the basal plane with A_3 pointing toward the nitrogen. Having A_3 in the basal plane suggests that the nitrogen ion has relaxed along the [0001] direction (i.e. the nitrogen has moved away from its axial zinc neighbor to a new equilibrium position that is close to the plane containing the three basal zinc neighbors). This relaxation is partially driven by the electrostatic repulsion between the "hole" on the nitrogen and the positive charge of the axial zinc cation. Density functional theory calculations [46, 48] have predicted this movement away from the axial zinc neighbor.

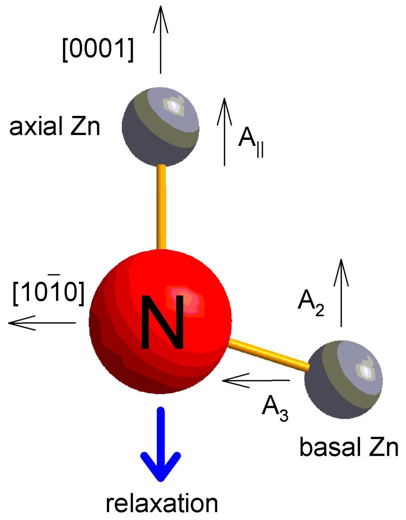

Figure 15. Model of the neutral nitrogen acceptor in zinc oxide showing the directions of the principal axes for the ^{67}Zn hyperfine interaction matrices. These three ions are in the ($\bar{1}2\bar{1}0$) plane.

Previous magnetic resonance investigations have focused on the ^{14}N hyperfine interactions [42, 44]. In the present research, complete sets of ^{67}Zn hyperfine parameters have been obtained for the one axial and the three basal zinc neighbors of the neutral nitrogen acceptor. These ^{67}Zn results establish that the nitrogen is at an oxygen site and is isolated (i.e., it is not adjacent to another defect). Together, the ^{14}N and ^{67}Zn results provide information about the distribution of spin density in the ground state of this neutral defect. The ^{67}Zn hyperfine parameters, especially, address the delocalization of the unpaired spin and can be used as an experimental check on advanced density functional theory calculations.

The ^{14}N hyperfine interaction matrix can be separated into isotropic and anisotropic parts,

$$\mathbf{A}^{(^{14}\mathrm{N})} \rightarrow A \begin{bmatrix} 1 & 0 & 0 \\ 0 & 1 & 0 \\ 0 & 0 & 1 \end{bmatrix} + P \begin{bmatrix} -\frac{2}{5} & 0 & 0 \\ 0 & -\frac{2}{5} & 0 \\ 0 & 0 & \frac{4}{5} \end{bmatrix} \tag{55}$$

where Morton and Preston [55] calculate $A = 1811$ MHz for an electron in a $2s$ orbital and $P = 138.8$ MHz for an electron in a $2p$ orbital. The ^{14}N hyperfine interaction matrix in its principal axis basis is

$$\mathbf{A}^{(^{14}\mathrm{N})} \rightarrow \begin{bmatrix} -8.0 & 0 & 0 \\ 0 & -8.0 & 0 \\ 0 & 0 & 81.1 \end{bmatrix} = 21.7 \begin{bmatrix} 1 & 0 & 0 \\ 0 & 1 & 0 \\ 0 & 0 & 1 \end{bmatrix} + 74.25 \begin{bmatrix} -\frac{2}{5} & 0 & 0 \\ 0 & -\frac{2}{5} & 0 \\ 0 & 0 & \frac{4}{5} \end{bmatrix}. \tag{56}$$

This hyperfine interaction matrix suggests that $\frac{21.7}{1811} \approx 1\%$ of the electron wavefunction is in a nitrogen $2s$ orbital and $\frac{74.25}{138.8} \approx 53\%$ of the electron wavefunction is in a nitrogen $2p$ orbital. Thus, a significant portion of the unpaired spin ($\sim 54\%$) is localized on the nitrogen ion [39, 42].

The above analysis implies that approximately 46% of the unpaired spin is distributed on the zinc and oxygen ions neighboring the nitrogen ion. Unfortunately, hyperfine lines from the oxygen ions are not observed because the ^{17}O nuclei have a natural abundance of only 0.038% [3]. Thus, there is no experimental information available about the amount of spin density on the oxygen ions. On the other hand, the ^{67}Zn hyperfine interaction matrices do provide information about the unpaired spin density at the zinc cations. The isotropic parts of the ^{67}Zn matrices ($19.\bar{3}$ MHz for the axial neighbor and $17.6\bar{3}$ MHz for the basal neighbors) indicate that the unpaired spin has only a small contribution from $4s$ orbitals (less than 1%) on the zinc neighbors [55]. Larger contributions to the unpaired spin density at the zinc neighbors from the $3d$ and $4p$ orbitals are suggested by the anisotropic parts of the ^{67}Zn matrices. Interpreting these anisotropic results in terms of $3d$ and $4p$ orbitals is, however, challenging. Depending on the choice made for the signs of the ^{67}Zn principal values, the results of Morton and Preston [55] indicate that a significant portion of the spin density (perhaps 5% or more) may be found on each of the neighboring zinc ions. Advanced density functional theory quantum modeling methods appear to be the best approach to extract electronic information from these anisotropic experimental ^{67}Zn results.

V. Silicon Interstitial Impurity in Titanium Dioxide (TiO_2)

A silicon-related defect is identified in titanium dioxide through observations of ^{47}Ti and ^{49}Ti hyperfine lines with the magnetic field along the [001] direction and the angular dependence of ^{29}Si hyperfine lines. These observations suggest that the unpaired electron is highly localized about two silicon nuclei with one silicon located at or near a titanium site and the other in a neighboring tetrahedral interstitial site. The unpaired electron is primarily located at the interstitial silicon where it interacts with two neighboring titanium nuclei. The results of an isochronal pulse anneal experiment with an as-grown sample and observations of the electron paramagnetic resonance spectrum in a reduced sample lead to the assignment of an effective 1+ charge state for the observed paramagnetic state.

The rutile titanium dioxide crystals investigated in this dissertation were grown by the Verneuil process and purchased from Crystec (Berlin, Germany). A description of the rutile structure is provided in Appendix C. Samples were cut from a $10 \times 10 \times 2$ mm^3 plate into $3 \times 3 \times 2$ mm^3 pieces. One piece was left in its as-grown state. Another piece was initially used in a previous study [56] after being lithium-doped by annealing with lithium hydroxide powder for 6 hr at 450 K in air. A third piece was initially used in a previous study [37] after being reduced in nitrogen for 3 hr at 650 K. The as-grown fully oxidized titanium dioxide crystals include several unintentionally incorporated defects. These defects include chromium, copper, iron, and vanadium substitutional impurities, and oxygen vacancies. When impurities such as chromium and iron are present in the starting materials, they cause oxygen vacancies (for charge compensation) during growth due to their preferred trivalent charge states.

The electron paramagnetic resonance spectrum of the singly ionized chromium acceptor with the magnetic field along the [001] direction is displayed in Figure 16, and shows the $I = 0$ line at 136.7 mT and the characteristic set of four hyperfine lines from the $I = \frac{3}{2}$ [4] hyperfine interaction with a 9.5% naturally abundant [3] ^{53}Cr nucleus. The hyperfine splitting of the outer most ^{49}Ti hyperfine lines is 0.4 mT.

This $S = \frac{3}{2}$ defect was characterized by Gerritsen *et al.* [57] as a substitutional Cr^{3+} ($3d^3$) impurity at a titanium site. Due to a large fine interaction and the limitations of the spectrometer used in this dissertation, only one transition is observable.

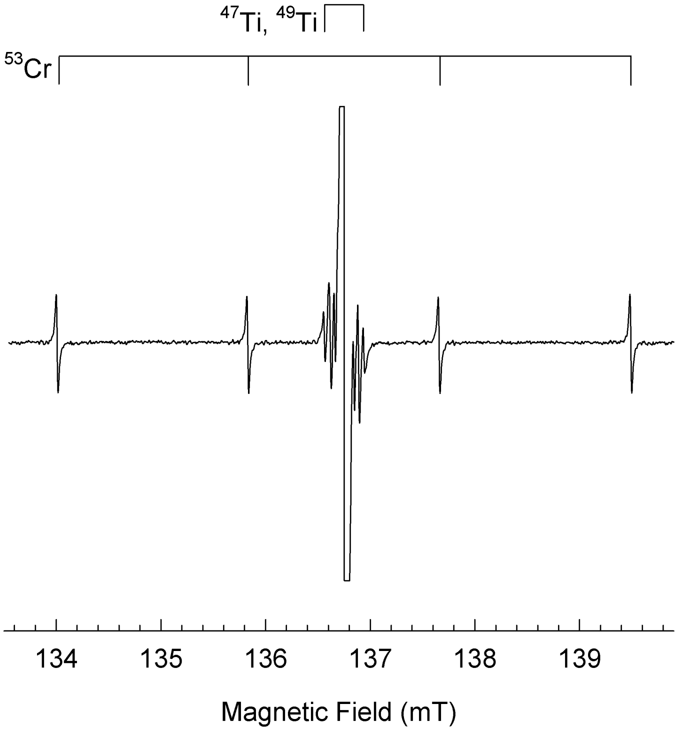

Figure 16. Electron paramagnetic resonance spectrum of the singly ionized chromium acceptor Cr^{3+} ($3d^3$) in titanium dioxide with the magnetic field along the [001] direction. The data were recorded from an as-grown sample at a microwave frequency of 9.5485 GHz and a temperature of 34 K.

The electron paramagnetic resonance spectrum of the neutral copper acceptor with the magnetic field along the [001] direction is displayed in Figure 17, and shows the two characteristic sets of four hyperfine lines from the $I = \frac{3}{2}$ [4] hyperfine interaction with a 69.2% naturally abundant [3] ^{63}Cu nucleus and a 30.8% naturally abundant [3] ^{65}Cu nucleus. This $S = \frac{1}{2}$ defect was initially described by Gerritsen and Sabisky [58]. The electron paramagnetic resonance spectrum shows significantly intense forbidden transitions due to a strong nuclear electric quadrupole interaction. The hyperfine and nuclear electric quadrupole interactions were characterized by Ensign *et al.* [59]. Refined hyperfine and nuclear electric quadrupole interaction parameters, and evidence that this copper related defect is an acceptor with a Cu^{2+} ($3d^9$) ion located at a titanium site and a doubly ionized oxygen vacancy immediately neighboring is provided by Brant *et al.* [60].

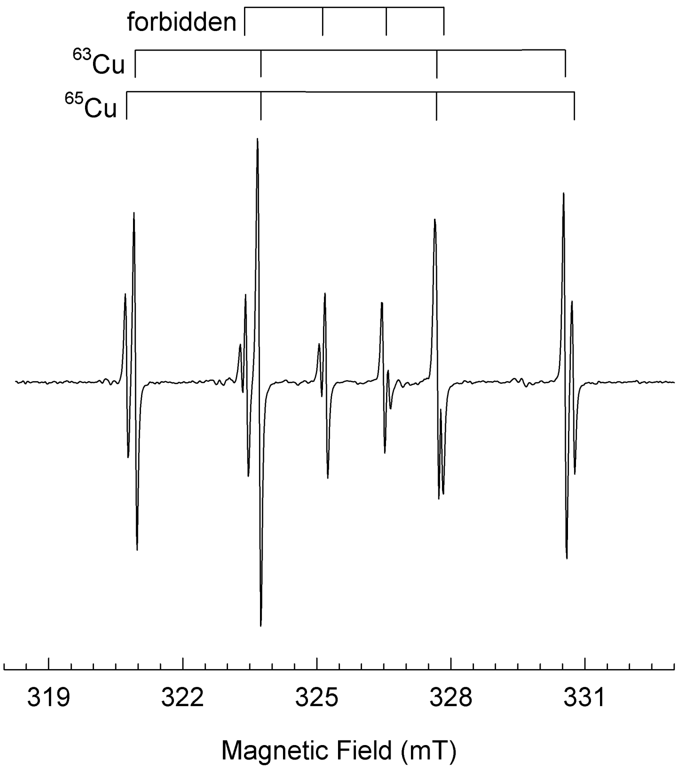

Figure 17. Electron paramagnetic resonance spectrum of the copper Cu^{2+} ($3d^9$) substitutional impurity next to an oxygen vacancy in titanium dioxide with the magnetic field along the [001] direction. The data were recorded from an as-grown sample at a microwave frequency of 9.5410 GHz and a temperature of 20 K.

The electron paramagnetic resonance spectrum of the singly ionized iron acceptor with the magnetic field along the [001] direction is displayed in Figure 18, and shows the $I = 0$ line at 83.7 mT and the characteristic set of two hyperfine lines from the $I = \frac{1}{2}$ [4] hyperfine interaction with a 2.1% naturally abundant [3] ^{57}Fe nucleus. The hyperfine splitting of the outer most ^{49}Ti hyperfine lines is 0.2 mT. This $S = \frac{5}{2}$ defect was characterized by Carter and Okaya [61] using an electron paramagnetic resonance spectroscopy technique that is significantly different than the technique employed in this dissertation. They established the defect as a substitutional Fe^{3+}

($3d^5$) impurity at a titanium site. Due to a large fine interaction and the limitations of the spectrometer used in this dissertation, only one transition is observable.

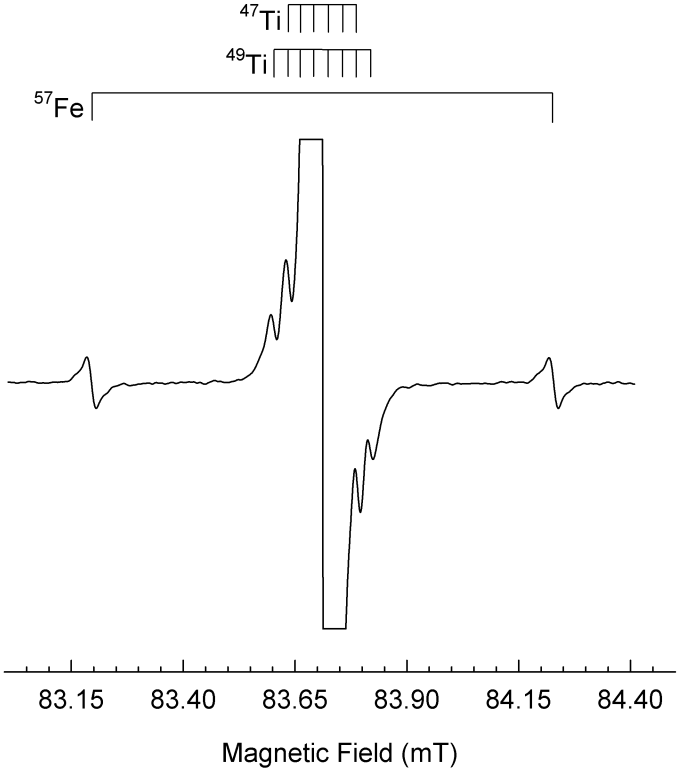

Figure 18. Electron paramagnetic resonance spectrum of the singly ionized iron acceptor Fe^{3+} ($3d^5$) in titanium dioxide with the magnetic field along the [001] direction. The data were recorded from an as-grown sample at a microwave frequency of 9.5484 GHz and a temperature of 34 K.

The electron paramagnetic resonance spectrum of the substitutional vanadium isovalent impurity with the magnetic field along the [001] direction is displayed in Figure 19, and shows the characteristic set of eight hyperfine lines from the $I = \frac{7}{2}$ [4] hyperfine interaction with a 100% [3] naturally abundant ^{51}V nucleus. This $S = \frac{1}{2}$ defect was characterized by Gerritsen and Lewis [62] as a substitutional V^{4+} ($3d^1$) impurity at a titanium site.

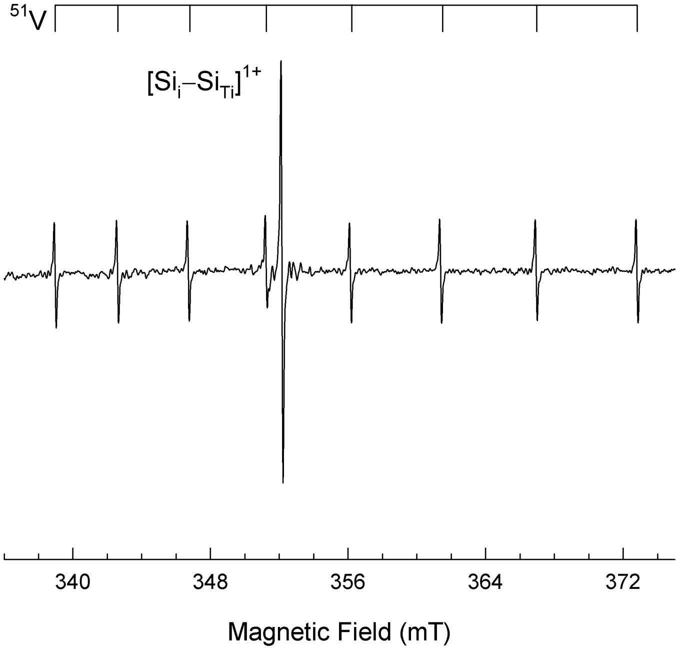

Figure 19. Electron paramagnetic resonance spectrum of the substitutional vanadium isovalent defect V^{4+} ($3d^1$) in titanium dioxide with the magnetic field along the [001] direction. The data were recorded from an as-grown sample at a microwave frequency of 9.5485 GHz and a temperature of 34 K.

The electron paramagnetic resonance spectrum of the singly ionized oxygen vacancy with the magnetic field along the [001] direction is displayed in Figure 20, and shows the $I = 0$ line at 373.7 mT and two characteristic sets of hyperfine lines. One set is a set of eight hyperfine lines from the $I = \frac{7}{2}$ [4] hyperfine interaction with a 5.4% [3] naturally abundant ^{49}Ti nucleus. The other set is a set of six hyperfine lines from the $I = \frac{5}{2}$ [4] hyperfine interaction with a 7.4% [3] naturally abundant ^{47}Ti nucleus. The hyperfine splitting of the outer most ^{49}Ti hyperfine lines is 9.3 mT. This $S = \frac{1}{2}$ defect and its neutral $S = 1$ state were initially described by Yang *et al.* [63] as unpaired electrons that are each localized about a single neighboring titanium atom forming Ti^{3+} ions. Of the three titanium nearest neighbors of the oxygen vacancy, the unpaired electrons are localized on the two that form a line that runs along the [001] direction. These $S = \frac{1}{2}$ [64] and $S = 1$ [65] defects were later characterized by Brant *et al.*

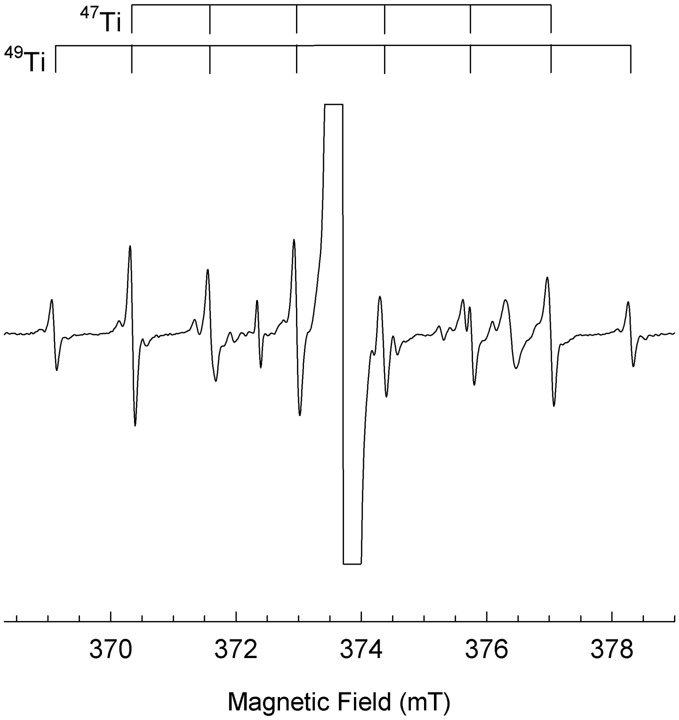

Figure 20. Electron paramagnetic resonance spectrum of the singly ionized oxygen vacancy V_O^{1+} in titanium dioxide with the magnetic field along the [001] direction. The data were recorded from an as-grown sample at a microwave frequency of 9.5403 GHz and a temperature of 30 K. The spectrum is photoinduced with 442 nm light from a cw HeCd laser.

5.1 Results

The electron paramagnetic resonance spectrum shown in Figure 21 is detected in an as-grown Crystec sample of rutile titanium dioxide after exposure to 442 nm laser light with the magnetic field along the [001] direction. This spectrum is observed in the Crystec sample after lithium diffusion, the Crystec reduced sample, and several samples grown by the Verneuil process at the University of Yamanashi, Japan. This spectrum was also seen before exposure to 442 nm laser light in an as-grown sample as seen in Figure 19 but is less intense. The central $I = 0$ line at 352.1 mT in Figure 21 is created by a single unpaired electron. Surrounding this line, are six hyperfine lines overlapping eight hyperfine lines representing the hyperfine interaction of the single unpaired electron with an $I = \frac{5}{2}$ and an $I = \frac{7}{2}$ nucleus, respectively. There are also two hyperfine lines representing the interaction of the single unpaired electron

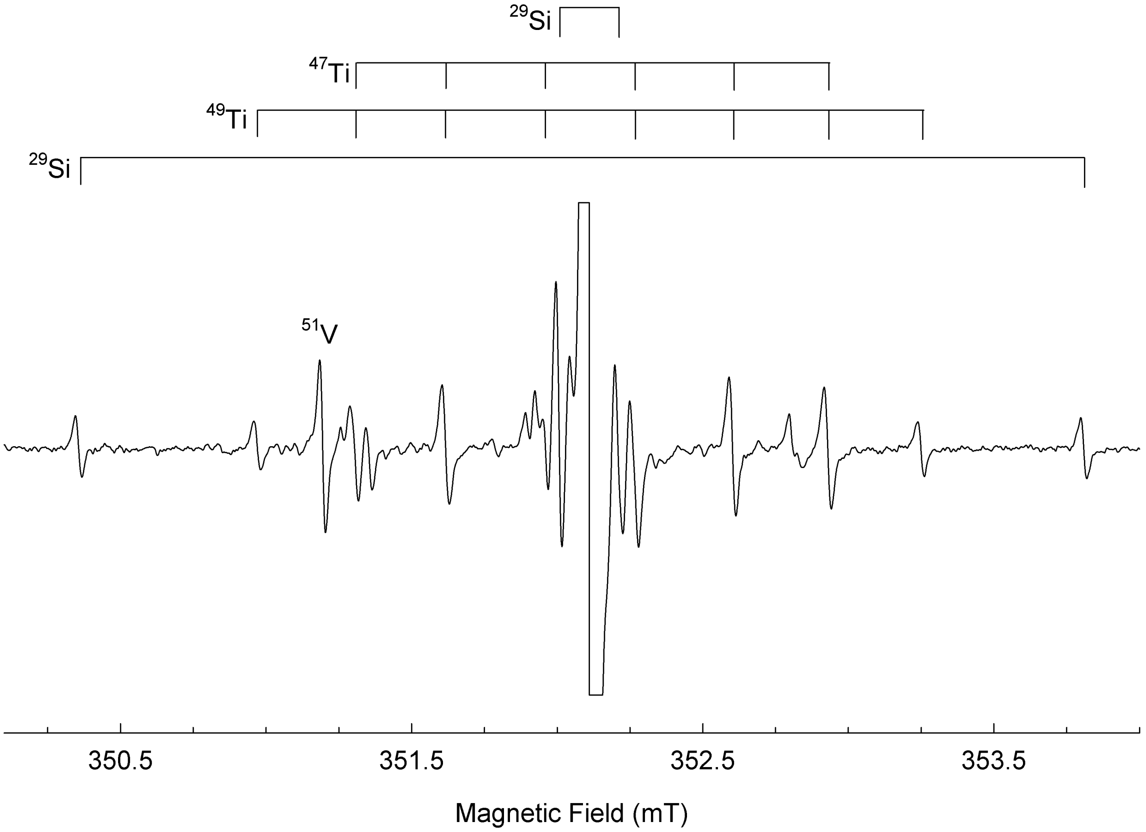

Figure 21. Electron paramagnetic resonance spectrum of the silicon defect $[\mathrm{Si_i} - \mathrm{Si_{Ti}}]^{1+}$ in titanium dioxide with the magnetic field along the [001] direction. The data were recorded from an as-grown sample at a microwave frequency of 9.5490 GHz and a temperature of 40 K after exposing the sample to 442 nm light from a cw HeCd laser.

with an $I = \frac{1}{2}$ nucleus, and multiple hyperfine lines within 0.5 mT of the $I = 0$ line representing interactions of the single unpaired electron with other more distant nuclei. Two of these latter hyperfine lines are identified as part of the six and eight-line sets, and two more of these hyperfine lines are attributed to an interaction of the single unpaired electron with a ^{29}Si nucleus [63]. The six-line pattern is identified as a hyperfine interaction with a ^{47}Ti nucleus, and the eight-line pattern is identified as a hyperfine interaction with a ^{49}Ti nucleus. These assignments are made because ^{47}Ti has $I = \frac{5}{2}$ [4], ^{49}Ti has $I = \frac{7}{2}$ [4] and the intensity ratio of the high-field ^{47}Ti/^{49}Ti hyperfine line at 352.9 mT to the high-field ^{49}Ti hyperfine line at 353.2 mT is 2.24. This is close to the predicted value of 2.76 calculated from natural abundances [3].

Comparing the intensities of the ^{47}Ti and ^{49}Ti hyperfine lines to the center $I = 0$ line, the estimated isotopic abundance of the ^{47}Ti isotope is 12.19% and of the ^{49}Ti isotope is 10.23%. These values are nearly double that of the natural abundances which are 7.4% for ^{47}Ti and 5.4% for ^{49}Ti [3]. This strongly suggests that the unpaired electron is interacting equally with two titanium nuclei. Using the intensity of the hyperfine line at 352.2 mT, the estimated isotopic abundance of the $I = \frac{1}{2}$ nucleus previously attributed to ^{29}Si is 8.54%. Using the intensity of the hyperfine line at 353.8 mT, the estimated isotopic abundance of the unattributed $I = \frac{1}{2}$ nucleus is 3.28%. Based on known natural abundances [3], possible candidates for the previously attributed nucleus are ^{77}Se (7.6%), ^{125}Te (7.1%), and ^{29}Si (4.7%), and for the unattributed nucleus are ^{29}Si (4.7%), and ^{57}Fe (2.1%). Since this is an undoped sample, selenium and tellurium are not expected to be present, but iron and silicon could possibly have been present in the crystal-growth starting materials. This is because selenium and tellurium are some of the least abundant elements in the Earth's crust (66th and 72nd, respectively [20]), and silicon and iron are some of the most abundant elements in the Earth's crust (2nd and 4th, respectively [20]). Iron is eliminated from consideration since it is unlikely to form a defect with a single unpaired electron, and already forms a stable defect, as shown in Figure 18. The subsequent angular dependence of this electron paramagnetic resonance spectrum in Figure 21 establishes it as the interaction of a single unpaired electron with two silicon nuclei and two titanium nuclei.

The angular dependence of the electron paramagnetic resonance spectrum is shown in Figure 22. The data were recorded without 442 nm illumination from a rutile titanium dioxide sample annealed in lithium hydroxide [56]. The intensity of the spectrum from this sample is greatest among the three samples considered when not exposed to 442 nm light. Recording data with no exposure to 442 nm light eliminates interference from the oxygen vacancy which has electron paramagnetic resonance lines in the same region of magnetic field (300 − 400 mT).

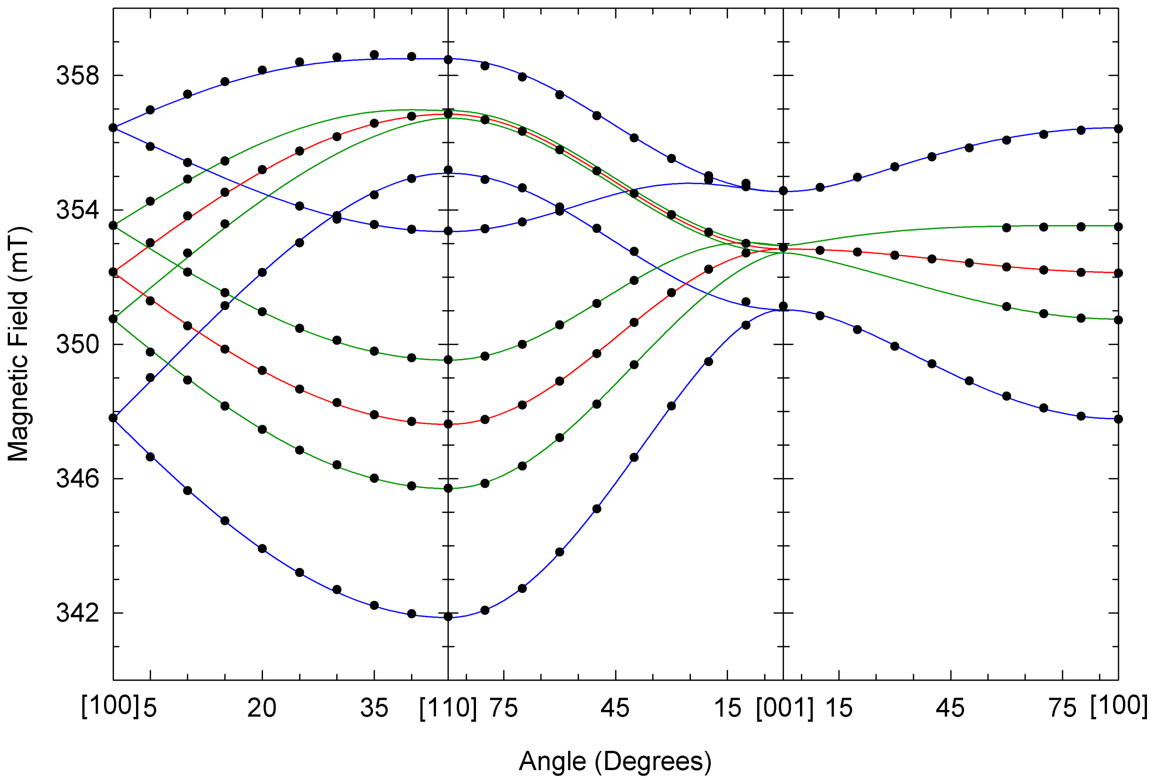

Figure 22. Angular dependence of the $I = 0$ line and ^{29}Si hyperfine lines. Solid lines are calculated at 9.569 GHz using the spin-Hamiltonian parameters in Table 3. Black dots are experimental data recorded at 40 K and scaled to 9.569 GHz. Red lines represent spectra with no hyperfine interactions. Each set of green and blue lines represent spectra with a single ^{29}Si hyperfine interaction.

Upon rotation of the magnetic field from the [001] direction to the [100] direction in the (100) plane, there is no significant splitting of the central line or of the ^{29}Si hyperfine lines. Once the magnetic field is rotated off the [001] axis, the titanium hyperfine lines become unidentifiable. This may be due to either slightly inequivalent hyperfine interactions with each titanium nucleus, the nuclear electric quadrupole interaction becoming dominant over the hyperfine interaction giving rise to forbidden lines, or a combination of both. The hyperfine splitting of the outermost ^{49}Ti hyperfine lines is 2.3 mT with the magnetic field along the [001] direction. The central $I = 0$ line moves to a lower field reaching a minimum of 351.9 mT along the [100] direction, while the hyperfine splitting of the outer ^{29}Si hyperfine lines increases from 3.5 mT to 8.6 mT, reaching a maximum along the [100] direction. The inner

^{29}Si hyperfine lines get "lost" in the titanium hyperfine lines until the magnetic field has been rotated about 60° away form the [001] direction where they emerge from the titanium hyperfine lines. From this point, the hyperfine splitting of the inner ^{29}Si hyperfine lines continues to increase, reaching a maximum of 2.8 mT along the [100] direction from an initial value of 0.2 mT along the [001] direction.

Figure 23 shows the electron paramagnetic resonance spectrum with the magnetic field along the [100] direction. Along this direction the ^{29}Si hyperfine lines are clearly observed as two pairs of equally intense lines. From the intensities of the ^{29}Si hyperfine lines in this spectrum, the estimated isotopic abundance is 4.7%. This is essentially equal to the natural abundance of ^{29}Si [3], and thus confirming the identity of these $I = \frac{1}{2}$ nuclei.

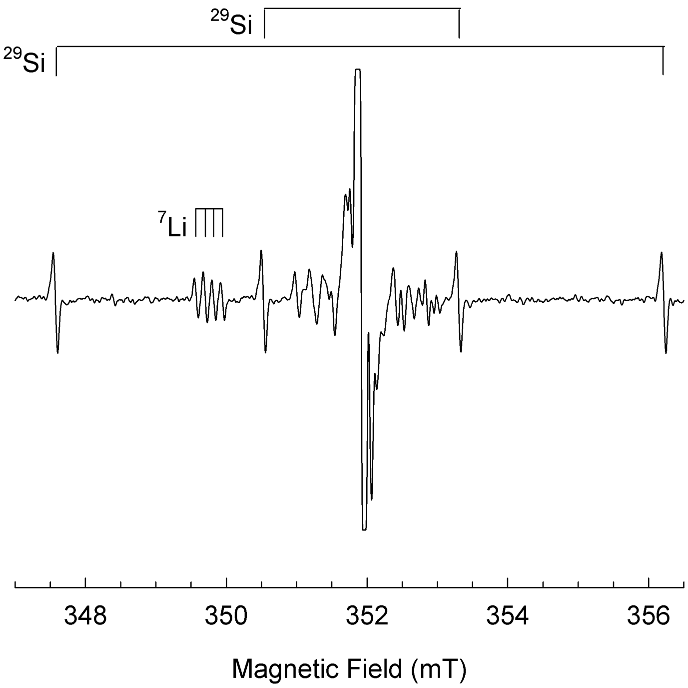

Figure 23. Electron paramagnetic resonance spectrum of the silicon defect $[\mathrm{Si_i} - \mathrm{Si_{Ti}}]^{1+}$ in titanium dioxide with the magnetic field along [100]. The data were recorded at a microwave frequency of 9.5637 GHz and a temperature of 40 K from a sample that was annealed in lithium hydroxide for 6 hr.

Upon rotation of the magnetic field from [100] to [110] in the (001) plane, the $I = 0$ line and the ^{29}Si hyperfine lines split into two spectra. One spectrum moves to a higher field, reaching a maximum of 357.0 mT along the [110] direction. The hyperfine splitting of the outer ^{29}Si hyperfine lines decreases, reaching a minimum of 3.3 mT along the [110] direction. The hyperfine splitting of the inner ^{29}Si hyperfine lines decreases as well until they are lost in the titanium hyperfine lines for angles greater than 30° from the [100] direction. The other spectrum moves to a lower field, reaching a minimum of 347.8 mT along the [110] direction. The hyperfine splitting of both sets of ^{29}Si hyperfine lines increases, reaching a maximum of 3.8 mT for the inner set and 11.5 mT for the outer set along the [110] direction.

Upon rotation of the magnetic field from the [110] direction to the [001] direction in the (110) plane, the high field spectrum moves to lower field while the low field spectrum moves to higher field until the two spectra merge into one when the magnetic field is along the [001] direction. The outer ^{29}Si hyperfine splitting of the high field spectrum increases slightly. The inner ^{29}Si hyperfine lines of the high field spectrum are not observed during this rotation. The outer ^{29}Si hyperfine splitting of the low field spectrum decreases. The inner ^{29}Si hyperfine splitting of the low field spectrum decreases as well until the hyperfine lines are lost in the titanium hyperfine lines for angles greater than 50° from the [110] direction.

These angular dependence data establish that a single unpaired electron is interacting with two silicon nuclei and are sufficient for determining the g matrix and ^{29}Si hyperfine interaction matrices, but the change in ionization state of the defect due to photo-excitation is yet to be determined by an isochronal pulse anneal experiment and an observation of the spectrum in a reduced sample of titanium dioxide.

The results of an isochronal pulse anneal experiment are presented in Figure 24. Data were recorded from an as-grown Crystec sample. The sample was exposed to 442 nm light from a cw HeCd laser at a temperature of 20 K for 5 min prior to commencing the experiment. The intensities of the Cr^{3+}, Cu^{2+}, Fe^{3+}, $\mathrm{V}_\mathrm{O}^{1+}$, and $\mathrm{V}_\mathrm{O}^{0}$ spectra were monitored during the experiment along with the intensity of the silicon-related spectrum. A pulse anneal consisted of raising the temperature in the microwave cavity to a specified temperature, holding at that temperature for 30 s, then lowering back down to the monitoring temperature of 20 K where the intensities of the previously mentioned spectra were once again measured. The sample was not exposed to light between pulse anneals.

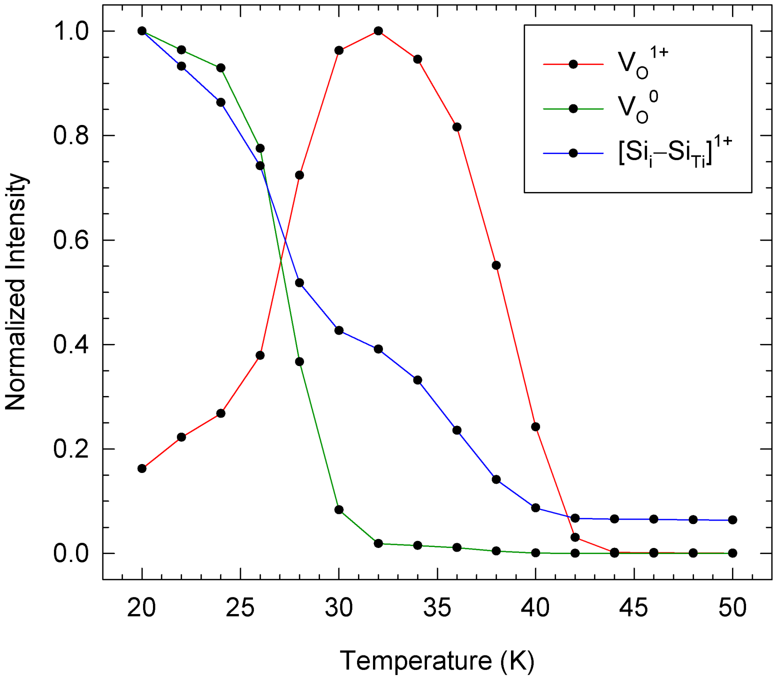

Figure 24. Results of an isochronal pulse anneal experiment on a sample of as-grown titanium dioxide. Black dots are experimental data recorded at a temperature of 20 K with the magnetic field along the [001] direction. Data connected by red lines are from the singly ionized oxygen vacancy, by green lines are from the neutral oxygen vacancy, and by blue lines are from the singly ionized silicon interstitial complex.

After exposure to light but before starting the anneal, the intensity of the Cr^{3+} spectrum decreased by 33%, the Cu^{2+} spectrum decreased by 74%, and the Fe^{3+} spectrum decreased by 30%. The oxygen-vacancy-related spectra became observable with the V_O^{1+} spectrum 64% less intense than the V_O^0 spectrum. The intensity of the silicon-related spectrum increased by a factor of 11. During exposure, electrons are effectively pumped from Cr^{3+} and Fe^{3+} defects to Cu^{2+} and V_O^{2+} defects. At this point, it is unclear if electrons are pumped to or from the silicon-related defect.

During the isochronal anneal, the Cr^{3+} spectrum increased steadily until it reached full recovery after the 40 K anneal. The Cu^{2+} and Fe^{3+} spectra remained relatively flat throughout this experiment which ended after a 50 K anneal, and are not expected to recover until after an anneal above 100 K when electrons are released from Cu^{1+} defects to be trapped once again at Fe^{3+} defects [60].

As the temperature of the anneal step increased, the intensity of the V_O^0 spectrum decreased slightly until it started decreasing rapidly between the 24 K and 30 K anneals, and disappeared after the 32 K anneal. During this drop in intensity of the V_O^0 spectrum, the intensity of the silicon-related spectrum decreased rapidly until it started to level off after the 32 K anneal, and the intensity of the V_O^{1+} spectrum increased rapidly until it reached a peak after the 32 K anneal. The decrease in the intensity of the silicon-related spectrum nearly mirrored the increase in the intensity of the V_O^{1+} spectrum during this stage of the experiment. Between the 32 K and 44 K anneals, the silicon-related spectrum and the V_O^{1+} spectrum increased their rate of decay until after the 44 K anneal where they both recovered to their pre-exposure intensities.

These results suggest that for anneals between 20 K and 32 K electrons are being released from V_O^0 defects, which become V_O^{1+} defects, and returned to the silicon-related defect. For anneals between 32 K and 44 K, electrons are being released from V_O^{1+} defects and returned to the silicon-related defect until the defects reach their pre-exposure concentrations. This establishes the silicon-related defect as a hole trap. Therefore during exposure to 442 nm light, electrons are being pumped away from this defect. This assertion is supported by an observation of the spectrum without exposure to 442 nm light in a reduced sample of titanium dioxide, which has been annealed in nitrogen for 3 hr at 650 K. The intensity of the spectrum is 70% less in the reduced sample compared to the intensity of the spectrum in the as-grown sample. Since reduction decreases the intensity of the electron paramagnetic resonance spectrum, the change in ionization state from the non-paramagnetic state to the paramagnetic state is positive [58, 60].

5.2 Spin-Hamiltonian Analysis

The angular dependence data presented in Figure 22 and included in Appendix F are sufficient in determining the full set of parameters necessary for describing the g matrix and ^{29}Si hyperfine interaction matrices. These parameters are the principal-axis directions and the principal values associated with them. The principal-axis directions are determined through observations of the angular dependence data. The principal values are determined by fitting the angular dependence data to a set of spin Hamiltonians. The width of each electron paramagnetic resonance line is approximately 0.05 mT. This gives a minimum estimated error for the g parameters of ± 0.0003, and for the hyperfine interaction parameters of ± 0.3 MHz.

Based on the behavior of the angular dependence data, the principal axes of the g matrix and both ^{29}Si hyperfine interaction matrices are determined. The electron paramagnetic resonance spectrum has both a high field and low field turning point along the [110] direction in two planes of rotation. This establishes that the g matrix has two principal axes along $\langle 110 \rangle$ directions, and by default the third principal axis must be along the [001] direction. The same can be said for the outer ^{29}Si hyperfine lines, where the hyperfine splitting reaches both a maximum and a minimum along the [110] direction in two planes of rotation. This establishes that the outer ^{29}Si hyperfine interaction matrix has two principal axes along $\langle 110 \rangle$ directions, and by default the third principal axis must be along the [001] direction. The inner ^{29}Si hyperfine splitting reaches a maximum along the [110] direction in two planes of rotation. This establishes that the inner ^{29}Si hyperfine interaction matrix has at least one principal axis along a $\langle 110 \rangle$ direction. The minimum of the inner ^{29}Si hyperfine splitting can not be determined because the inner ^{29}Si hyperfine lines of the high field spectrum about the [110] and [001] directions and in the (110) plane are not observable. A second principal axis is determined for the inner ^{29}Si hyperfine interaction matrix by noticing that the spectrum does not split in the (100) plane and that the crystal has D_{4h} symmetry. This symmetry has a (001) mirror plane, twofold rotation axes along the $\langle 110 \rangle$ directions, and a fourfold rotation axis along the [001] direction in titanium dioxide. Since the [110] direction has already been established as a principal axis, the (001) mirror plane will cause the spectrum to split into two components if a principal axis is not along the [001] direction. Since no splitting is observed for the inner ^{29}Si hyperfine lines when rotating the magnetic field in the (100) plane, then a principal axis must be along the [001] direction. By default, this establishes the third principal axis for the inner ^{29}Si hyperfine interaction matrix along another $\langle 110 \rangle$ direction.

The principal values of the g matrix are determined by fitting spin Hamiltonians to angular dependence data of the $I = 0$ line or ^{29}Si hyperfine lines, and principal values of the ^{29}Si hyperfine interaction matrices are determined by fitting a spin Hamiltonian to their respective angular dependence data. The principal values of the g matrix are determined by fitting the spin Hamiltonian

$$\hat{H}_s = \mu_B \hat{\mathbf{S}} \cdot \mathbf{g} \cdot \mathbf{B} \tag{57}$$

to the angular dependence data of the $I = 0$ line. This line and spin Hamiltonian represent a configuration of the defect that has only $I = 0$ nuclei present. The results of a least-squares fitting are g parameters of 1.9159, 1.9376, and 1.9668 for principal axes along the $[\bar{1}10]$, [001], and [110] directions, respectively. The standard deviation of the frequency data from the fit is 867 kHz. This standard deviation translates into an estimated error of ±0.0002. This estimate is within the minimum estimate. The principal values of the g matrix and both ^{29}Si hyperfine interaction matrices are determined by fitting the spin Hamiltonian

$$\hat{H}_s = \mu_B \hat{\mathbf{S}} \cdot \mathbf{g} \cdot \mathbf{B} + \hat{\mathbf{S}} \cdot \mathbf{A} \cdot \hat{\mathbf{I}} - g_{\mathrm{Si}} \mu_N \hat{\mathbf{I}} \cdot \mathbf{B}, \tag{58}$$

where g_{Si} is the g factor for ^{29}Si and is known to be -1.11052 [4], to the angular dependence data of the ^{29}Si hyperfine lines. Each set of silicon hyperfine lines and the spin Hamiltonian represent a configuration of the silicon-related defect with a single ^{29}Si nucleus. The results of a least-squares fitting to the inner ^{29}Si hyperfine lines are g parameters of 1.9158, 1.9379, and 1.9668, and hyperfine interaction parameters of 0.3 MHz, 0.8 MHz, and 105.3 MHz for principal axes along the $[\bar{1}10]$, [001], and [110] directions, respectively. The standard deviation of the frequency data from the fit is 986 kHz. This standard deviation translates into an estimated error for the g parameters of ±0.0002, and for the hyperfine interaction parameters of ±2 MHz. The g parameter error estimate is within the minimum estimate, but the hyperfine-interaction-parameter error estimate is larger. The results of a least-squares fitting to the outer ^{29}Si hyperfine lines are g parameters of 1.9159, 1.9376, and 1.9668, and hyperfine interaction parameters of 91.4 MHz, 95.4 MHz, and 316.4 MHz for principal axes along the $[\bar{1}10]$, [001], and [110] directions, respectively. The standard deviation of the frequency data from the fit is 1.56 MHz. This standard deviation translates into an estimated error for the g parameters of ±0.0003, and for the hyperfine interaction parameters of ±3 MHz. The g parameter error estimate is equal to the minimum estimate, but the hyperfine-interaction-parameter error estimate is larger. A consolidation of this data is presented in Table 3 and is used in a discussion of the defect model.

Table 3. Spin-Hamiltonian parameters for the silicon interstitial in titanium dioxide. The hyperfine interaction parameters are in terms of h and are in units of MHz. The estimated error in the g parameters is ±0.0003 and in the hyperfine interaction parameters is ±3 MHz.

Parameter	Principal Value	Principal-Axis Direction
g parameters		
g_1	1.9159	$[\bar{1}10]$
g_2	1.9377	[001]
g_3	1.9668	[110]
Hyperfine interaction parameters for ^{29}Si		
$\lvert A_1^{(1)}\rvert$	0.3	$[\bar{1}10]$
$\lvert A_2^{(1)}\rvert$	0.8	[001]
$\lvert A_3^{(1)}\rvert$	105.3	[110]
$\lvert A_1^{(2)}\rvert$	91.4	$[\bar{1}10]$
$\lvert A_2^{(2)}\rvert$	95.4	[001]
$\lvert A_3^{(2)}\rvert$	316.4	[110]

5.3 *Discussion*

The electron paramagnetic resonance data identify a defect with a single unpaired electron that interacts with at least two silicon and two titanium nuclei. The ^{29}Si hyperfine parameters give information about the distribution of the electron wave function. The intensity of the ^{47}Ti and ^{49}Ti hyperfine lines compared to the intenisty of the $I = 0$ line along with the known structure of rutile titanium dioxide (see Appendix C) provide information about the location of the silicon atoms. The pulse anneal experiment suggests that this defect loses an electron or captures a hole when exposed to 442 nm light from a HeCd laser. The spectrum after reduction suggests that the change in ionization state from the non-paramagnetic state to the paramagnetic state is positive. All of this information supports the proposed defect model shown in Figure 25. In this model, one silicon is located at a titanium site and the other silicon is located at a neighboring tetrahedral interstitial site. The silicon ions are stabilized at their positions by a double bond.

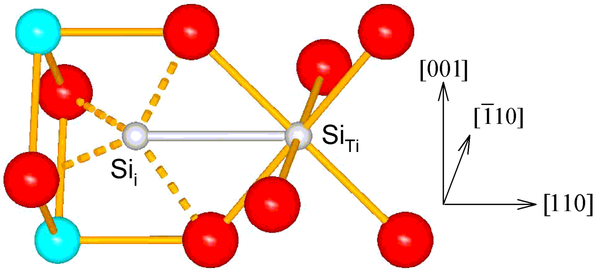

Figure 25. Model of the silicon intersititial impurity in titanium dioxide. Titanium atoms are in turquoise, oxygen atoms are in red, and silicon atoms are in gray. The gold bonds are those normally present in titanium dioxide, the dashed bonds are those that would exist between an atom at a tetrahedral site and the neighboring oxygen atoms, and the gray bond is the double bond between the two silicon atoms.

Using the hyperfine interaction parameters in Table 3 along with the atomic predictions of Morton and Preston [55], the distribution of the electron wave function among the silicon nuclei is estimated. For a ^{29}Si atom, the hyperfine interaction matrix can be broken into isotropic and anisotropic parts,

$$\mathbf{A}^{(^{29}\mathrm{Si})} \to A \begin{bmatrix} 1 & 0 & 0 \\ 0 & 1 & 0 \\ 0 & 0 & 1 \end{bmatrix} + P \begin{bmatrix} -\frac{2}{5} & 0 & 0 \\ 0 & -\frac{2}{5} & 0 \\ 0 & 0 & \frac{4}{5} \end{bmatrix} \tag{59}$$

where Morton and Preston [55] calculate $A = -4594$ MHz for an electron in a $3s$ orbital and $P = -285.5$ MHz for an electron in a $3p$ orbital. Within experimental error, the inner silicon hyperfine interaction matrix in its principal-axes basis is

$$\mathbf{A}^{(1)} \to \begin{bmatrix} 0 & 0 & 0 \\ 0 & 0 & 0 \\ 0 & 0 & -105 \end{bmatrix} = -35 \begin{bmatrix} 1 & 0 & 0 \\ 0 & 1 & 0 \\ 0 & 0 & 1 \end{bmatrix} - 87.5 \begin{bmatrix} -\frac{2}{5} & 0 & 0 \\ 0 & -\frac{2}{5} & 0 \\ 0 & 0 & \frac{4}{5} \end{bmatrix} \tag{60}$$

where the sign of the $A_3^{(1)}$ hyperfine interaction parameter is chosen to be negative, since the sign of the g factor for ^{29}Si is negative. This hyperfine interaction matrix suggests that $\frac{-35}{-4549.4} \approx 1\%$ of the electron wavefunction is in a silicon $3s$ orbital and $\frac{-87.5}{-285.5} \approx 31\%$ of the electron wavefunction is in a silicon $3p$ orbital. Within experimental error, the outer silicon hyperfine interaction matrix is

$$\begin{aligned} \mathbf{A}^{(2)} \to & \begin{bmatrix} -93 & 0 & 0 \\ 0 & -93 & 0 \\ 0 & 0 & -316 \end{bmatrix} \\ & = -167.\bar{3} \begin{bmatrix} 1 & 0 & 0 \\ 0 & 1 & 0 \\ 0 & 0 & 1 \end{bmatrix} - 185.8\bar{3} \begin{bmatrix} -\frac{2}{5} & 0 & 0 \\ 0 & -\frac{2}{5} & 0 \\ 0 & 0 & \frac{4}{5} \end{bmatrix} \end{aligned} \tag{61}$$

where the sign of the $A_3^{(2)}$ hyperfine interaction parameter is chosen to be negative, since the sign of the g factor for ^{29}Si is negative. The signs of the other hyperfine interaction parameters are chosen to be the same because choosing signs such that $A_3^{(2)}$ has the opposite sign of $A_1^{(2)}$ and $A_2^{(2)}$ results in $P = -340.8\bar{3}$ MHz which is significantly greater than the calculated P parameter. This hyperfine interaction matrix suggests that $\frac{-167.\bar{3}}{-4549.4} \approx 4\%$ of the electron wavefunction is in a silicon $3s$ orbital and $\frac{-185.8\bar{3}}{-285.5} \approx 65\%$ of the electron wavefunction is in a silicon $3p$ orbital. In total, 32% of the electron wavefunction is on one silicon nuclei, and 69% is on the other for a total of 101%. This suggests that the unpaired electron is highly localized on this pair of silicon nuclei.

The intensity of the ^{47}Ti/^{49}Ti hyperfine lines compared to the intensity of the $I = 0$ line in Figure 21 suggests equivalent hyperfine interactions with two titanium nuclei. Based on this and and the tendency of silicon to form a 4+ ion, an initial placement for a silicon is at a titanium site which has two titanium nearest neighbors along the [001] direction at a distance of 2.959 Å. As seen with the chromium (Figure 16) and iron (Figure 18) substitutional impurities, this placement produces hyperfine splittings of the outer most ^{49}Ti hyperfine lines that are less than 0.5 mT. This is more consistent with the set of hyperfine lines around the $I = 0$ line in Figure 21. The ^{47}Ti/^{49}Ti hyperfine pattern is more consistent with the ^{47}Ti/^{49}Ti hyperfine pattern of the oxygen vacancy (Figure 20) but has a quarter of the hyperfine splitting. Silicon is not likely to substitute for an oxygen, but a similar site is the tetrahedral interstitial site. This site is surrounded by oxygen anions at a distance of 1.7 Å. This is a reasonable site for silicon because the silicon cations in the various polymorphs of silicon dioxide are tetrahedrally coordinated with oxygen anions at a typical distance of 1.6 Å [66]. The tetrahedral interstitial sites like the oxygen anions have three nearest-neighbor titanium cations. Two of the titanium cations are located at a distance of 1.871 Å and the other is located at a distance of 2.104 Å. A paramagnetic silicon impurity at this site would likely have a nondegenerate ^{47}Ti/^{49}Ti hyperfine pattern in addition to the observed doubly-degenerate ^{47}Ti/^{49}Ti hyperfine pattern. One way of addressing this missing hyperfine pattern is to replace the titanium cation at 2.104 Å with the second silicon. With a silicon at a tetrahedral interstitial site and another silicon at this titanium site, all of the features of the electron paramagnetic resonance spectrum in Figure 21 are explained. This arrangement also fits with the principal-axis directions of the g and ^{29}Si hyperfine interaction matrices, because the axis formed by the two silicons is along the [110] direction. This model becomes even more intriguing by noticing that the silicon-to-silicon distance is close to the typical bond length (2.2 Å) of the double silicon bond in acyclic disilenes [67].

All of this information taken together suggests that the silicon-related defect is most likely a deep donor with an effective charge of 1+ in the paramagnetic state. One possible ionic configuration of this silicon-related donor in its nonparamagnetic neutral state is a neutral silicon atom at the interstitial site and a Si^{4+} ion at the titanium site. In the paramagnetic state, the captured hole is likely to be localized on the interstitial silicon, essentially becoming a Si^{1+} ion which has an unpaired electron in a p orbital. The only problem with this model is that there is no apparent reason why this configuration would be stable. There is no Coulomb attraction between the two silicons, because a Si^{4+} ion at a titanium site has an effective charge of 0 according to the crystal lattice. This lack of a stabilizing force is addressed by treating the silicons as a disilene molecule. This configuration of the silicon-related donor in its nonparamagnetic neutral state has the silicons sharing a double bond. This gives each silicon an effective charge state of 2+. In this model the silicon atoms are stabilized in their positions by the double bond and a Coulomb attraction. The Coulomb attraction arises from an effective charge of 2+ at the interstitial silicon and an effective charge of 2− at the substitutional silicon. For this configuration, the paramagnetic state likely arises from an unpaired electron in a bonding orbital between the two silicons. Due to the effective charges of the silicons, this unpaired electron is likely to be repelled from the substitutional silicon ion and attracted to the interstitial silicon ion. This essentially creates a Si^{1+} ion at the interstitial site and a Si^{4+} ion at the substitutional site. These models are somewhat speculative which is why advanced density functional theory calculations could help confirm or exclude these models as an explanation for the observed features and angular dependence of the silicon-related electron paramagnetic resonance spectrum.

VI. Sulfur Vacancy in Stannous Hexathiohypodiphosphate ($Sn_2P_2S_6$)

Previous electron paramagnetic resonance studies of stannous hexathiohypodiphosphate (SPS) have identified substitutional impurities at the Sn^{2+} site and also an intrinsic defect at the Sn^{2+} site. The substitutional impurities are antimony Sb^{2+} ($5s^25p^1$) [68] and manganese Mn^{2+} ($3d^5$) [69], and the intrinsic defect is the small polaron Sn^{3+} [70]. The intrinsic small polaron was previously assigned to the electron paramagnetic resonance spectrum in Figure 26 by Ruediger *et al.* [71], but the assignment of the intrinsic small polaron to a different electron paramagnetic resonance spectum by Brant *et al.* [70] has placed doubt on this previous assignment. In this dissertation, the electron paramagnetic resonance spectrum previously assigned to the intrinsic small polaron is now shown to be due to the singly ionized sulfur vacancy. This assignment is made through careful observations of hyperfine interactions in the angular dependence of the electron paramagnetic resonance spectrum.

6.1 Results

As described in Appendix D, SPS has a monoclinic crystal structure that only sightly deviates from an orthorhombic crystal structure. Due to the modest angular dependence of the electron paramagnetic resonance spectrum in Figure 26, this deviation from orthogonality is disregarded and the directions a, b, and c are considered orthogonal.

The electron paramagnetic resonance spectrum shown in Figure 26 is detected in several samples of SPS after exposure to 442 nm laser light at a temperature of 45 K with the magnetic field along the b direction. After photo-excitation, the spectrum is stable below 100 K. The sample considered in the current study has dimensions of $1.5 \times 2 \times 3$ mm^3, and was grown by the Bridgman process at the Uzhgorod State University, Ukraine. The sample was provided to the Air Force Institute of Technology by Dr. Dean Evans (Air Force Research Laboratory, Materials and Manufacturing

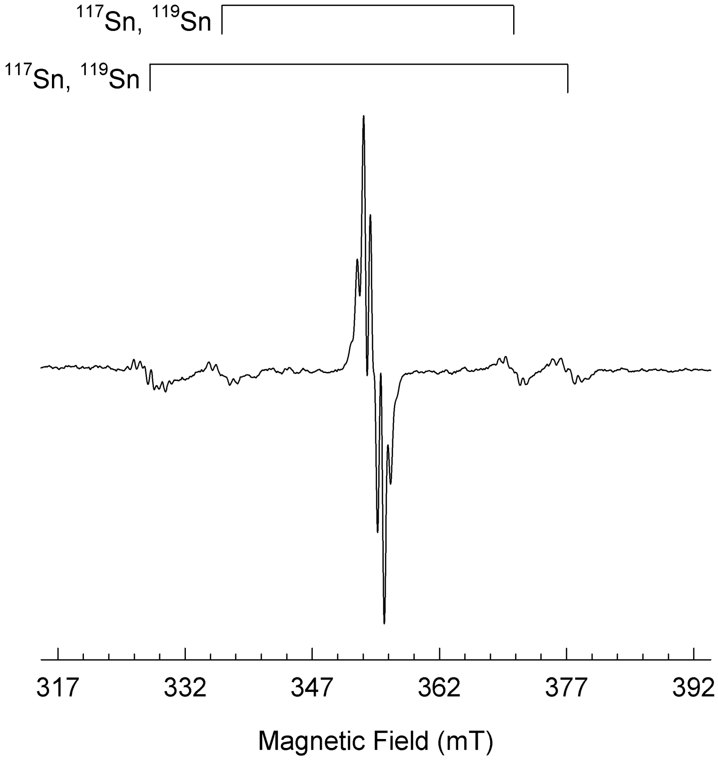

Figure 26. Electron paramagnetic resonance spectrum of the singly ionized sulfur vacancy V_S^{1+} in SPS with the magnetic field along the *b* direction. The data were recorded at a microwave frequency of 9.3896 GHz and a temperature of 45 K. The spectrum is photoinduced with 442 nm laser light from a cw HeCd laser.

Directorate). The electron paramagnetic resonance spectrum is composed of a central set of lines at 354.1 mT surrounded by four sets of less intense lines. The inner and outer pairs of the four surrounding sets are each due to a strong hyperfine interaction with an $I = \frac{1}{2}$ nucleus.

A close-up of the central set and the high-field hyperfine sets is shown in Figures 27, 28, and 29 for magnetic fields along the *a*, *b*, and *c* directions, respectively. These figures show that the central set is symmetric and composed of four closely spaced lines, and that the high-field hyperfine sets are also symmetric but do not mirror the structure of the central set, as expected. With strong hyperfine interactions, differences in the nuclear magnetic moments of a nucleus among its isotopes will cause the associated hyperfine lines to split. The observation that the hyperfine sets

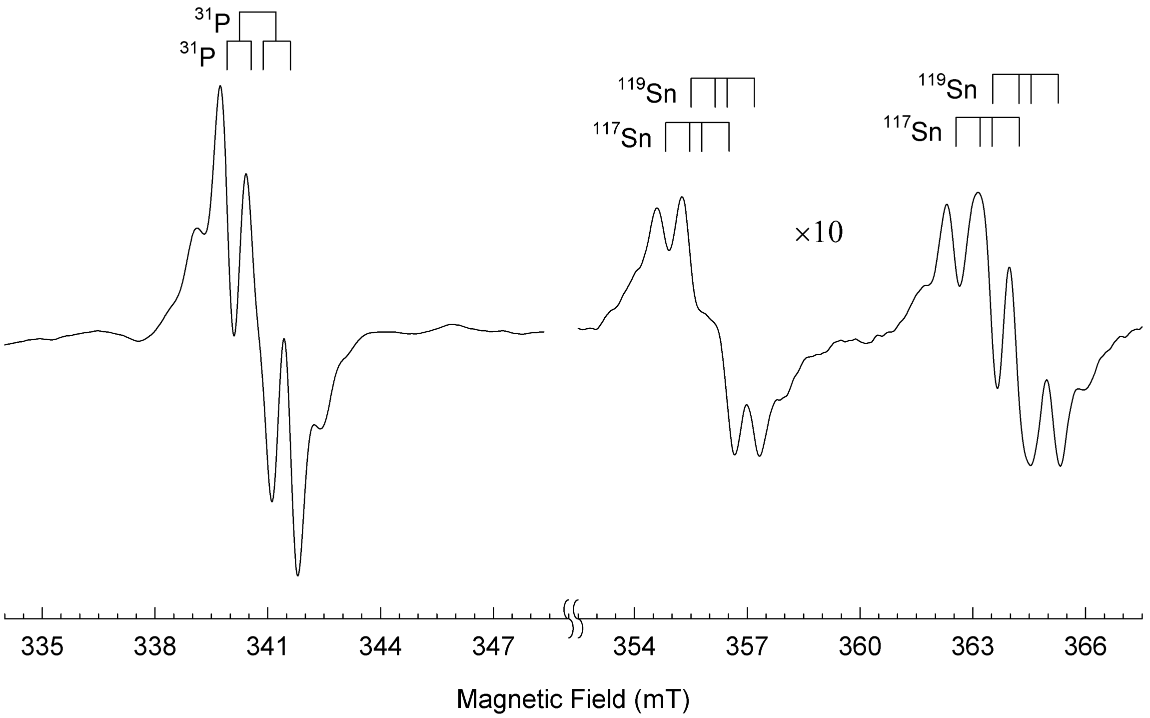

Figure 27. Hyperfine lines in the electron paramagnetic resonance spectrum of the singly ionized sulfur vacancy in SPS with the magnetic field along the *a* direction. The data were recorded at a microwave frequency of 9.3959 GHz and a temperature of 45 K. The spectrum is photoinduced with 442 nm laser light from a cw HeCd laser.

are symmetric indicates that the interacting nucleus has multiple isotopes that have significant ($> 1\%$), nearly equal abundances and nuclear magnetic moments that are evenly distributed. Nuclei with $I = \frac{1}{2}$ that meet these requirements include ^{107}Ag and ^{109}Ag with natural abundances of 51.8% and 48.2% respectively, ^{111}Cd and ^{113}Cd with natural abundances of 12.8% and 12.2% respectively, and ^{117}Sn and ^{119}Sn with natural abundances of 7.7% and 8.6% respectively [3, 4]. Since these candidate nuclei have only two isotopes to consider, the outer lines in a hyperfine set are associated with the outer lines in the central set. The low-field line in a hyperfine set is associated with one isotope, and the high-field line in a hyperfine set is associated with the other isotope. Since hyperfine interactions are proportional to the nuclear magnetic moment of the nucleus, the difference in magnetic field between a line in a hyperfine set and its associated line in the central set is proportional to the nuclear magnetic moment of the associated isotope. Therefore, the ratio of the nuclear magnetic moments can

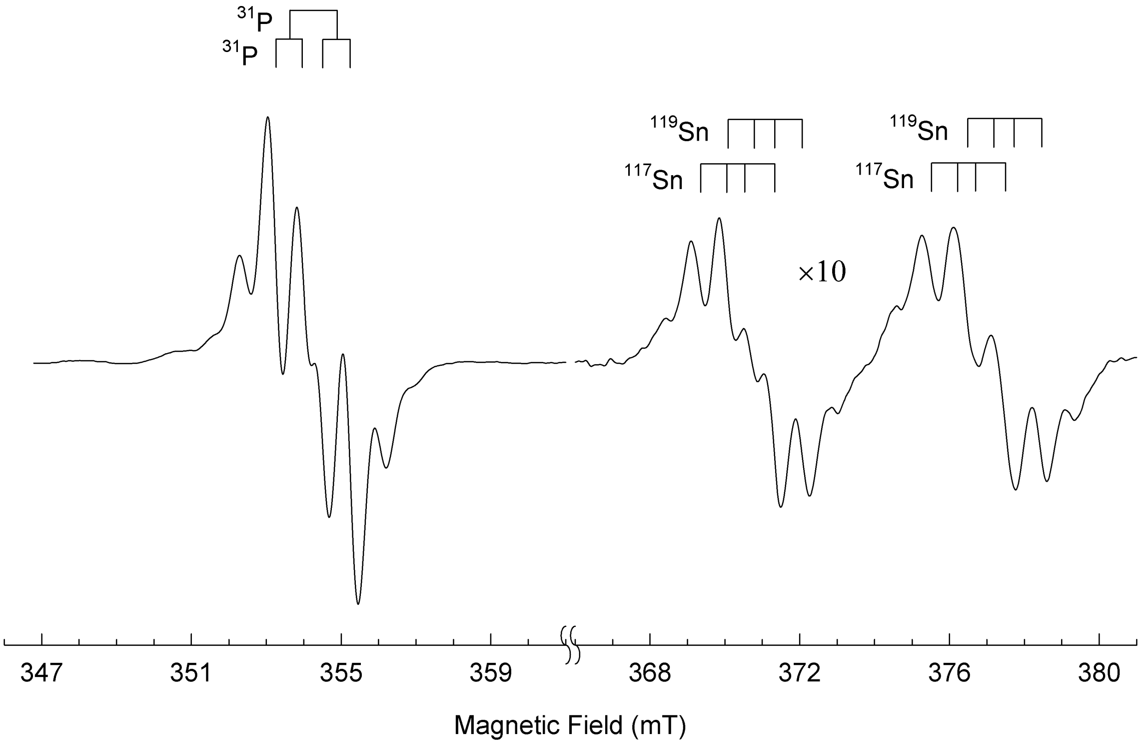

Figure 28. Hyperfine lines in the electron paramagnetic resonance spectrum of the singly ionized sulfur vacancy in SPS with the magnetic field along the *b* direction. The data were recorded at a microwave frequency of 9.3942 GHz and a temperature of 45 K. The spectrum is photoinduced with 442 nm laser light from a cw HeCd laser.

be estimated. In addition, an estimate of the abundance of each isotope can be made from the intensity of the lines. From data presented in Figures 27, 28, and 29, the ratio of the nuclear magnetic moments is estimated as 1.044 and the abundance is estimated as 5.6%. The ratio of the known nuclear magnetic moments is $\frac{-0.1305}{-0.1135} = 1.150$ for ^{107}Ag and ^{109}Ag, $\frac{-0.6225}{-0.5950} = 1.046$ for ^{111}Cd and ^{113}Cd, and $\frac{-1.046}{-0.9999} = 1.046$ for ^{117}Sn and ^{119}Sn [4]. Based on this information, the most likely nuclei responsible for the strong hyperfine interactions are those of tin.

With the magnetic field along the *c* direction, Figure 29 shows that the central set is centered at 352.9 mT, and composed of four equally intense hyperfine lines that are split by a central interval of 0.63 mT and by two outer intervals of 0.74 mT. Upon rotation from the *c* direction towards the *a* direction in the *b* plane, the central set moves to a lower field reaching a minimum of 340.8 mT. Also, the central

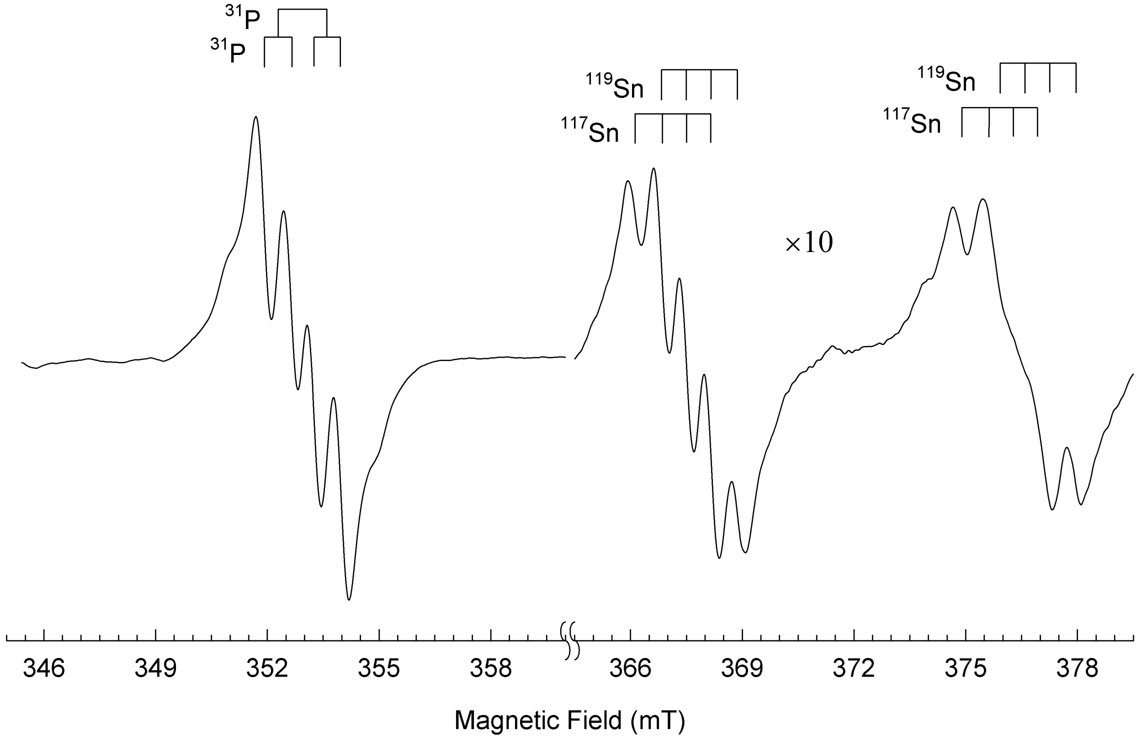

Figure 29. Hyperfine lines in the electron paramagnetic resonance spectrum of the singly ionized sulfur vacancy in SPS with the magnetic field along the *c* direction. The data were recorded at a microwave frequency of 9.3898 GHz and a temperature of 45 K. The spectrum is photoinduced with 442 nm laser light from a cw HeCd laser.

interval decreases reaching an apparent minimum of 0.35 mT, and the outer interval decreases slightly reaching an apparent minimum of 0.68 mT. Upon rotation from the *a* direction towards the *b* direction in the *c* plane, the central set moves to a higher field reaching a maximum of 354.2 mT. Also, the central interval increases reaching an apparent maximum of 0.49 mT, and the outer interval increases reaching an apparent maximum of 0.77 mT. For rotations in the *a* plane, the spectrum becomes asymmetric indicating splitting due to inequivalent orientations of the defect.

The angular dependence of the four lines of the central set is shown in Figure 30 and suggests a hyperfine interaction with two $I = \frac{1}{2}$ nuclei with a 100% abundance. Nuclei with $I = \frac{1}{2}$ and a nearly 100% natural abundance incude ^{1}H, ^{19}F, ^{31}P, ^{89}Y, ^{103}Rh, ^{169}Tm, ^{107}Ag and ^{109}Ag, and ^{203}Tl and ^{205}Tl [3, 4]. Of these, ^{1}H and ^{19}F could possibly be incorporated into undoped crystals through crystal-growth starting materials, and ^{31}P is certainly present. Since SPS is composed of P_2S_6 molecules where the two phosphorus atoms form bonds with the six sulfur atoms (see Appendix D), two ^{31}P nuclei are likely responsible for the four hyperfine lines in the central set.

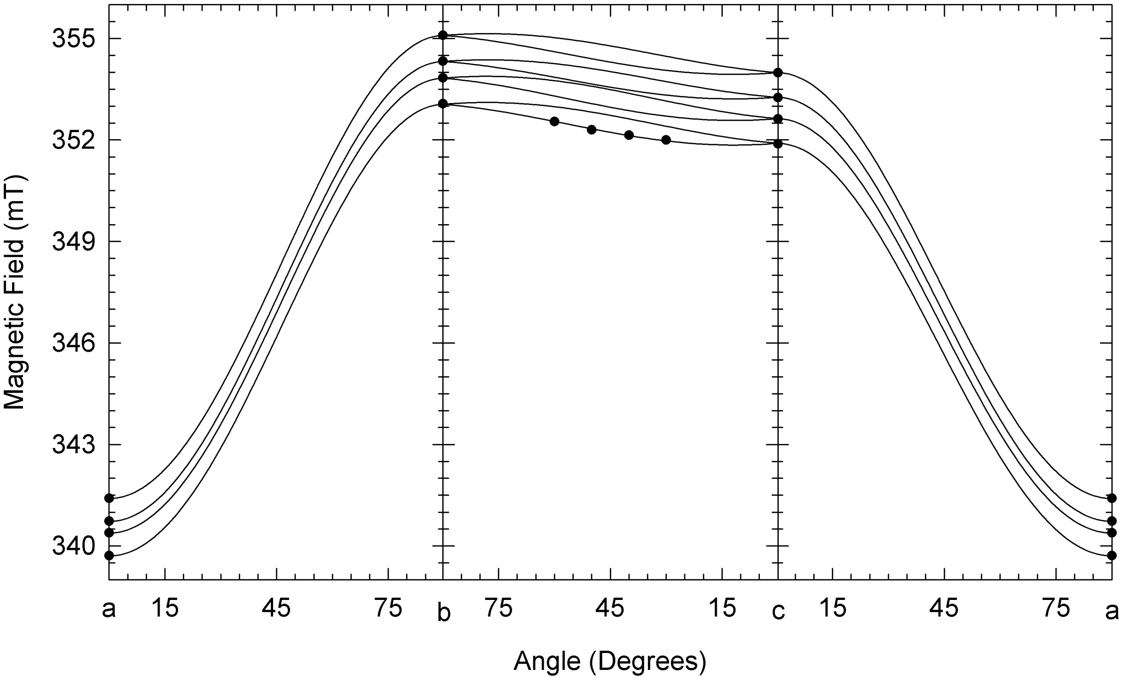

Figure 30. Angular dependence of the ^{31}P hyperfine lines. Solid lines are calculated at 9.39 GHz using the spin-Hamiltonian parameters in Table 4. Black dots are experimental data recorded at 45 K and scaled to 9.39 GHz.

The additional outer lines in the central sets in Figures 27 and 28 are attributed to hyperfine interactions with the remaining four tin nuclei that surround the P_2S_6 molecule (see Appendix D). This attribution is supported by a simulation of the central set in Figure 28. The simulation was carried out by using the best-fit g parameter and ^{31}P hyperfine interaction parameters. The width of the electron paramagnetic resonance lines and the value of a single hyperfine interaction parameter for four equally interacting tin nuclei were adjusted until the simulated spectrum closely fit the appearance of the recorded spectrum. Figure 31 shows the recorded spectrum and two simulated spectra. Figure 31(a) shows a simulation that uses only the best-fit g parameter and ^{31}P hyperfine interaction parameters. Figure 31(c) shows a simulation that uses the best-fit g parameter and ^{31}P hyperfine interaction parameters with the additional hyperfine interaction parameter of 37 MHz for the four equally interacting tin nuclei. Figure 31(b) shows the recorded spectrum. As can be seen in Figure 31 the spectrum in Figure 28 is described well by the best-fit parameters with the additional four equally interacting tin nuclei.

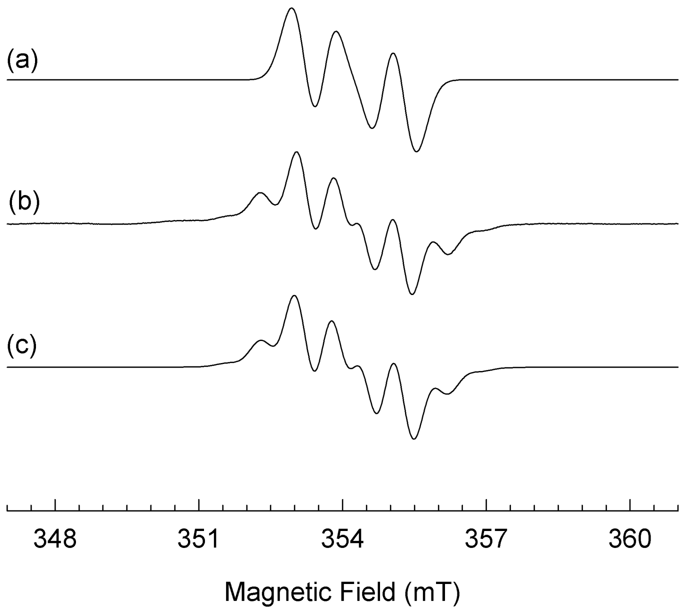

Figure 31. Simulations of the central set with the magnetic field along the b direction compared to recorded data. The simulations include the calculated g parameter and ^{31}P hyperfine interaction parameters for the magnetic field along the b direction. (a) Simulation that includes the calculated g parameter and ^{31}P hyperfine interaction parameters only. (b) Recorded data. (c) Simulation that includes the calculated g parameter and ^{31}P hyperfine interaction parameters, and a hyperfine interaction parameter of 37 MHz for four tin nuclei.

Only the average angular-dependence data of the high-field tin hyperfine sets and central set were recorded in the b and c planes. This was because identification of individual lines in each hyperfine set was difficult due to the width of the hyperfine lines and the slight splitting due to the isotopes of tin, and overlap with other lines in the low-field region made observation of the low-field tin hyperfine sets difficult. Angular-dependence data in the a plane was not recorded because splitting of the spectrum in this plane made determination of the centers difficult. These angular-dependence data are shown as black dots in Figure 32. The tin hyperfine interactions appear to be nearly isotropic with an average splitting from the center set of 15.4 mT for the inner hyperfine set and 22.7 mT for the outer hyperfine set.

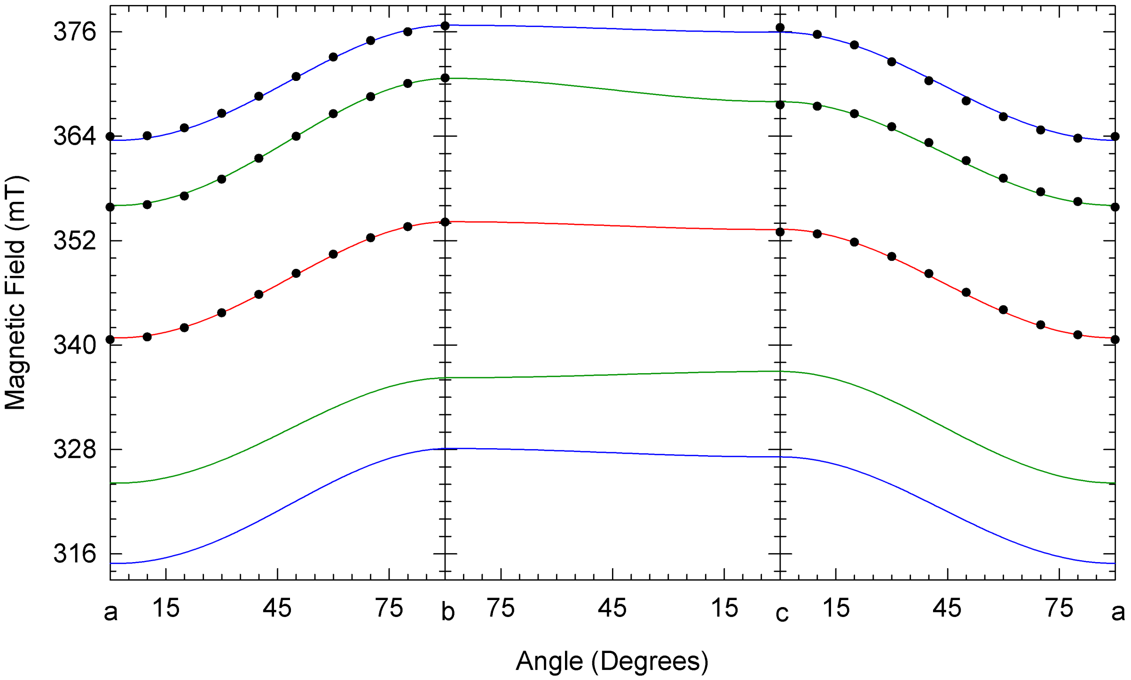

Figure 32. Angular dependence of the central set and tin hyperfine sets. Solid lines are calculated at 9.39 GHz using the spin-Hamiltonian parameters in Table 5. The red line is the calculated angular dependence of the g matrix, and the green and blue lines are each the calculated angular dependence of a hyperfine interation with a single tin nucleus. Black dots are experimental data recorded at 45 K and scaled to 9.39 GHz.

6.2 Spin-Hamiltonian Analysis

The angular-dependence data presented in Figure 30 and included in Appendix G are sufficient to estimate the principal values and principal-axis directions of the g matrix and ^{31}P hyperfine interaction matrices. The angular-dependence data presented in Figure 32 and included in Appendix G are sufficient to estimate the principal values and principal-axis directions of the g matrix and ^{117}Sn and ^{119}Sn hyperfine interaction matrices. The width of each electron paramagnetic resonance line is about 0.4 mT. This gives a mimimun estimated error for the g parameters of ±0.002, and for the hyperfine interaction parameters of ±2 MHz. Through observations of the angular-dependence data in Figure 32, one principal-axis direction is determined for the g matrix. Using this observation and making some reasonable assumptions, the principal values and principal-axis directions of the g matrix and ^{31}P hyperfine interaction matrices are estimated by fitting the angular-dependence data in Figure 30 to a spin Hamiltonian. Using some reasonable assumptions and the measured ratio of the nuclear magnetic moments of ^{117}Sn and ^{119}Sn, the principal values and principal-axis directions of the g matrix, and ^{117}Sn and ^{119}Sn hyperfine interaction matrices are estimated by fitting the angular-dependence data in Figure 32 to another spin Hamiltonian.

Angular-dependence data in Figure 32 show that the spectrum has a low-field turning point along the a direction in two planes of rotation. This establishes one principal-axis direction for the g matrix as the a direction. Since the crystal has C_{1h} symmetry with a single mirror plane normal to the b direction, the asymmetry observed in the spectrum for rotation of the magnetic field in the a plane is likely due to inequivalent orientations of the defect caused by the crystal symmetry. These inequivalent orientations are created by having the principal axes rotated by an angle about the a direction away from the b and c directions.

The g and ^{31}P hyperfine interaction parameters are estimated by observing that the angular-dependence of the ^{31}P hyperfine splitting appears to behave in the same manner as the center position of the spectrum. Therefore, it is assumed that the g matrix and the ^{31}P hyperfine interaction matrices share the same principal axes. Based on this assumption, when rotating the magnetic field away from the c direction towards the b direction in the a plane, one orientation of the defect will have a spectrum that expands and moves to lower field, while the other orientation of the defect will have a spectrum that contracts and moves to higher field. Due to this behavior, a single ^{31}P hyperfine line should emerge from the central set at the low-field side. After rotating the magnetic field 30° away from the c direction towards the b direction in the a plane, a hyperfine line appears on the low-field side of the central set. This hyperfine line remains observable until the magnetic field is rotated by 60° where the line begins to merge with the central set. This line has about half the intensity of a ^{31}P hyperfine line when the magnetic field is along the c direction supporting the previously asserted assumption. A spin Hamiltonian

$$\hat{H}_s = \mu_B \hat{\mathbf{S}} \cdot \mathbf{g} \cdot \mathbf{B} + \sum_{n=1}^{2} \left(\hat{\mathbf{S}} \cdot \mathbf{A}^{(n)} \cdot \hat{\mathbf{I}}^{(n)} - g_{\mathrm{P}} \mu_N \hat{\mathbf{I}}^{(n)} \cdot \mathbf{B} \right), \tag{62}$$

where g_P is the g factor for ^{31}P and is known to be 2.2634 [4], is fitted to the angular-dependence data in Figure 30. The results of a least-squares fitting routine where the g and ^{31}P hyperfine interaction matrices are assumed to have the same principal-axis directions are g parameters of 1.9700, 1.8945 and 1.9011, ^{31}P hyperfine interaction parameters of 18.6 MHz, 20.5 MHz and 19.3 MHz for one hyperfine interaction, and ^{31}P hyperfine interaction parameters of 28.1 MHz, 33.4 MHz and 36.3 MHz for the other hyperfine interaction. The principal-axis directions are along the a, $b \pm 12°$ towards $\pm c$, and $c \pm 12°$ towards $\mp b$ directions, respectively. The standard deviation of the frequency data from the fit is 329 kHz. This standard deviation translates into an estimated error for the g parameters of 0.00007, and for the hyperfine interaction parameters of 0.7 MHz. These estimates are well within the minimum estimates. These parameters are listed in Table 4 for the g matrix and ^{31}P hyperfine interaction matrices.

The g and ^{117}Sn and ^{117}Sn hyperfine interaction parameters are estimated by fitting the angular-dependence data in Figure 32 to a set of spin Hamiltonians. The angular-dependence data in Figure 32 are measurements of the center of the central and tin hyperfine sets. Since the high-field tin hyperfine sets were the only tin hyperfine sets measured, the spin Hamiltonian

$$\hat{H}_s = \mu_B \hat{\mathbf{S}} \cdot \mathbf{g} \cdot \mathbf{B} \tag{63}$$

Table 4. ^{31}P hyperfine interaction and g parameters for the singly ionized sulfur vacancy in SPS. The hyperfine interaction parameters are in terms of h and are in units of MHz. The estimated error in the g parameters is ±0.002 and in the hyperfine interaction parameters is ±2 MHz.

Parameter	Principal Value	Principal-Axis Direction
g parameters		
g_1	1.8945	$b \pm 12°$ towards $\pm c$
g_2	1.9011	$c \pm 12°$ towards $\mp b$
g_3	1.9700	a
Hyperfine interaction parameters for ^{31}P		
$\lvert A_1^{(1)} \rvert$	18.6	a
$\lvert A_2^{(1)} \rvert$	19.3	$c \pm 12°$ towards $\mp b$
$\lvert A_3^{(1)} \rvert$	20.5	$-b \pm 12°$ towards $\mp c$
$\lvert A_1^{(2)} \rvert$	28.1	a
$\lvert A_2^{(2)} \rvert$	33.4	$b \pm 12°$ towards $\pm c$
$\lvert A_3^{(2)} \rvert$	36.3	$c \pm 12°$ towards $\mp b$

is first fitted to the angular-dependence data of the central set in Figure 32 to calculate the principal values of the g matrix. The results of a least-squares fitting routine, where an initial guess for the principal-axis directions is along the a, b, and c directions, are g parameters of 1.9685, 1.8942, and 1.8991, and principal-axis directions within 2° of the a, b, and c directions, respectively. The standard deviation of the frequency data from the fit is 4.07 MHz. This standard deviation translates into an estimated error of ±0.0008. This estimate is well within the minimum estimate. These parameters are used in the spin Hamiltonian

$$\hat{H}_s = \mu_B \hat{\mathbf{S}} \cdot \mathbf{g} \cdot \mathbf{B} + \hat{\mathbf{S}} \cdot \mathbf{A} \cdot \hat{\mathbf{I}} - g_{\mathrm{Sn}} \mu_N \hat{\mathbf{I}} \cdot \mathbf{B}, \tag{64}$$

where g_{Sn} is the average g factor of ^{117}Sn and ^{119}Sn and is calculated from known data as -2.046 [4], to estimate the principal values of each ^{117}Sn and ^{117}Sn hyperfine interaction matrix. The results of a least-squares fitting routine to the angular-dependence data of the inner tin hyperfine set in Figure 32 are hyperfine interaction parameters of 877.3 MHz, 910.5 MHz, and 822.2 MHz for principal-axis directions along the a, *b*, and *c* directions, respectively. The standard deviation of the frequency data from the fit is 5.46 MHz. This standard deviation translates into an estimated error of ±10 MHz. This estimate is greater than the minimum estimate. The results of a least-squares fitting routine to the angular dependence data of the outer tin hyperfine set in Figure 32 are hyperfine interaction parameters of 1334.0 MHz, 1283.6 MHz, and 1291.1 MHz for principal-axis directions along the *a*, *b*, and *c* directions, respectively. The standard deviation of the frequency data from the fit is 7.08 MHz. This standard deviation translates into an estimated error of ±10 MHz. This estimate is greater than the minimum estimate. With these average parameters, the ^{117}Sn and ^{117}Sn hyperfine interaction parameters for each isotope are calculated using the measured ratio of the nuclear magnetic moments. These parameters are listed in Table 5 for the ^{117}Sn and ^{117}Sn hyperfine interaction matrices.

Table 5. ^{117}Sn and ^{119}Sn hyperfine interaction parameters for the singly ionized sulfur vacancy in SPS. The hyperfine interaction parameters are in terms of h and are in units of MHz. The estimated error is ±10 MHz.

Parameter	Principal Value	Principal-Axis Direction
Hyperfine interaction parameters for ^{117}Sn		
$\lvert A_1^{(1)}\rvert$	804.4	c
$\lvert A_2^{(1)}\rvert$	858.3	a
$\lvert A_3^{(1)}\rvert$	890.8	b
$\lvert A_1^{(2)}\rvert$	1255.8	b
$\lvert A_2^{(2)}\rvert$	1263.1	c
$\lvert A_3^{(2)}\rvert$	1305.1	a
Hyperfine interaction parameters for ^{119}Sn		
$\lvert A_1^{(1)}\rvert$	840.0	c
$\lvert A_2^{(1)}\rvert$	896.3	a
$\lvert A_3^{(1)}\rvert$	930.2	b
$\lvert A_1^{(2)}\rvert$	1311.4	b
$\lvert A_2^{(2)}\rvert$	1319.1	c
$\lvert A_3^{(2)}\rvert$	1362.9	a

6.3 Discussion

The electron paramagnetic resonance data identify a defect with a single unpaired electron that interacts with at least two tin and two phosphorus nuclei. The ^{31}P, and ^{119}Sn hyperfine parameters give information about the distribution of the electron wave function. This information along with the crystal structure of SPS support the assignment of this electron paramagnetic resonance spectrum to the singly ionized sulfur vacancy.

Using the hyperfine interaction parameters in Tables 4 and 5 along with the atomic predictions of Morton and Preston [55], the distribution of the electron wave function among the phosphorus and tin cations is estimated. Since both of these elements are post transition elements, the anisotropic part of the hyperfine interaction matrix can be separated into a term that accounts for p orbital contributions, and a term that accounts for additional contributions. This results in

$$\mathbf{A} \rightarrow A \begin{bmatrix} 1 & 0 & 0 \\ 0 & 1 & 0 \\ 0 & 0 & 1 \end{bmatrix} + P \begin{bmatrix} -\frac{2}{5} & 0 & 0 \\ 0 & -\frac{2}{5} & 0 \\ 0 & 0 & \frac{4}{5} \end{bmatrix} + F \begin{bmatrix} 1 & 0 & 0 \\ 0 & -1 & 0 \\ 0 & 0 & 0 \end{bmatrix} \qquad (65)$$

where Morton and Preston [55] calculate $A = 13306$ MHz for an electron in a ^{31}P 3s orbital, $P = 917$ MHz for an electron in a ^{31}P 3p orbital, $A = -43920$ MHz for an electron in a ^{119}Sn 5s orbital, and $P = -1831$ MHz for an electron in a ^{119}Sn 5p orbital.

The ^{31}P hyperfine interaction matrix for the weaker hyperfine interaction in its principal-axes basis is

$$\begin{aligned}\mathbf{A}^{(1)} &\to \begin{bmatrix} 18.6 & 0 & 0 \\ 0 & 19.3 & 0 \\ 0 & 0 & 20.5 \end{bmatrix} \\ &= 19.4\bar{6}\begin{bmatrix} 1 & 0 & 0 \\ 0 & 1 & 0 \\ 0 & 0 & 1 \end{bmatrix} + 1.291\bar{6}\begin{bmatrix} -\frac{2}{5} & 0 & 0 \\ 0 & -\frac{2}{5} & 0 \\ 0 & 0 & \frac{4}{5} \end{bmatrix} - 0.35\begin{bmatrix} 1 & 0 & 0 \\ 0 & -1 & 0 \\ 0 & 0 & 0 \end{bmatrix}\end{aligned} \tag{66}$$

where the signs of the principal values are chosen to give positive signs for A and P. The ^{31}P hyperfine interaction matrix for the stronger hyperfine interaction in its principal-axes basis is

$$\begin{aligned}\mathbf{A}^{(2)} &\to \begin{bmatrix} 28.1 & 0 & 0 \\ 0 & 33.4 & 0 \\ 0 & 0 & 36.3 \end{bmatrix} \\ &= 32.6\begin{bmatrix} 1 & 0 & 0 \\ 0 & 1 & 0 \\ 0 & 0 & 1 \end{bmatrix} + 4.625\begin{bmatrix} -\frac{2}{5} & 0 & 0 \\ 0 & -\frac{2}{5} & 0 \\ 0 & 0 & \frac{4}{5} \end{bmatrix} - 2.65\begin{bmatrix} 1 & 0 & 0 \\ 0 & -1 & 0 \\ 0 & 0 & 0 \end{bmatrix}\end{aligned} \tag{67}$$

where the signs of the principal values are chosen to give positive signs for A and P. In total, the ^{31}P hyperfine interaction matrices can account for $\frac{19.4\bar{6}+32.6}{13306} + \frac{1.291\bar{6}+4.625}{917} \approx$ 1% of the electron wave function in phosphorus $3s$ and $3p$ orbitals.

The ^{119}Sn hyperfine interaction matrix for the weaker hyperfine interaction in its principal-axes basis is

$$\begin{aligned}\mathbf{A}^{(1)} \rightarrow \begin{bmatrix} \text{-}840.0 & 0 & 0 \\ 0 & \text{-}896.3 & 0 \\ 0 & 0 & \text{-}930.2 \end{bmatrix} = \\ -888.8\bar{3}\begin{bmatrix} 1 & 0 & 0 \\ 0 & 1 & 0 \\ 0 & 0 & 1 \end{bmatrix} - 51.708\bar{3}\begin{bmatrix} \text{-}\frac{2}{5} & 0 & 0 \\ 0 & \text{-}\frac{2}{5} & 0 \\ 0 & 0 & \frac{4}{5} \end{bmatrix} + 28.15\begin{bmatrix} 1 & 0 & 0 \\ 0 & -1 & 0 \\ 0 & 0 & 0 \end{bmatrix}\end{aligned} \tag{68}$$

where the signs of the principal values are chosen to give negative signs for A and P. This hyperfine interaction matrix accounts for $\frac{-888.8\bar{3}}{-43920} \approx 2\%$ of the electron wave function in a silicon 5s orbital and $\frac{-51.708\bar{3}}{-1813} \approx 3\%$ of the electron wave function in a silicon 5p orbital. The ^{119}Sn hyperfine interaction matrix for the stronger hyperfine interaction in its principal-axes basis is

$$\begin{aligned}\mathbf{A}^{(2)} \rightarrow \begin{bmatrix} \text{-}1311.4 & 0 & 0 \\ 0 & \text{-}1319.1 & 0 \\ 0 & 0 & \text{-}1362.9 \end{bmatrix} = \\ -1331.1\bar{3}\begin{bmatrix} 1 & 0 & 0 \\ 0 & 1 & 0 \\ 0 & 0 & 1 \end{bmatrix} - 39.708\bar{3}\begin{bmatrix} \text{-}\frac{2}{5} & 0 & 0 \\ 0 & \text{-}\frac{2}{5} & 0 \\ 0 & 0 & \frac{4}{5} \end{bmatrix} + 3.85\begin{bmatrix} 1 & 0 & 0 \\ 0 & -1 & 0 \\ 0 & 0 & 0 \end{bmatrix}\end{aligned} \tag{69}$$

where the signs of the principal values are chosen to give negative signs for A and P. This hyperfine interaction matrix accounts for $\frac{-1331.1\bar{3}}{-43920} \approx 3\%$ of the electron wave function in a silicon 5s orbital and $\frac{-39.708\bar{3}}{-1813} \approx 2\%$ of the electron wave function in a silicon 5p orbital. In total, the ^{119}Sn hyperfine interaction matrices account for approximately 10% of the electron wave function in silicon 5s and 5p orbitals.

The previous analysis accounts for only 11% of the electron wave function on neighboring phosphorus and tin cations. Unfortunately, hyperfine lines from the sulfur anions are not observed because ^{33}S has a low natural abundance of 0.75% [3], making any ^{33}S hyperfine interactions difficult to observe. Setting this aside, it is assumed that the electron wave function is sparingly dispersed among the neighboring sulfur anions as well. Therefore, the electron wave function appears to be highly diffuse like the electron wave functions of many shallow-donor defects.

Since the sample is undoped and apparently only interacts with native atoms, the defect is likely due to an intrinsic defect. An intrinsic donor defect that can possibly have the observed hyperfine interactions is the sulfur vacancy. Since the defect has only one unpaired electron, the sulfur vacancy is likely in the singly ionized state. As described in Appendix D, the two phosphorus cations and six sulfur anions form a hypodiphosphate anion. Therefore, any sulfur vacancy is in close proximity (within 3.4 Å) to two phosphorus nuclei as seen in Table 6. Each sulfur anion is in close proximity (within 3.3 Å) to at least two tin cations. Two sulfur anions have an additional tin cation at about 3.3 Å, two other sulfur anions have an additional tin cation at about 3.5 Å, and the remaining sulfur anions have an additional tin cation at about 3.8 Å. It is the locations of the latter sulfur anions (labeled 1 and 2 in Table 6) that are the most likely candidates for the location of the sulfur vacancy. In Figure 33, one of these sulfur anions is encircled with a circle, and the other is encircled with a square. They are each connected with their nearest neighbor tin cations by a solid black line. Since the *a* direction is a principal axis direction of the *g* matrix with the least amont of shift from the free electon *g* factor, it is interesting to note that the axis formed by these sulfur anions is nearly along the *a* direction.

Table 6. Distances to three nearest tin and two nearest phosphorus neighbors of each sulfur anion in the hypodiphosphate anion of SPS. The distances were calculated from the crystal structure parameters of Dittmar and Schäfer [72], and are in units of Å.

Sulfur	Neighbor (Distance)				
1	P (2.015)	Sn (2.882)	Sn (3.015)	P (3.356)	Sn (3.801)
2	P (2.018)	Sn (2.951)	Sn (2.990)	P (3.414)	Sn (3.853)
3	P (2.026)	Sn (2.802)	Sn (3.307)	P (3.395)	Sn (3.525)
4	P (2.022)	Sn (2.828)	Sn (3.080)	P (3.318)	Sn (3.397)
5	P (2.036)	Sn (2.943)	Sn (3.053)	Sn (3.269)	P (3.357)
6	P (2.023)	Sn (2.876)	Sn (3.171)	Sn (3.296)	P (3.344)

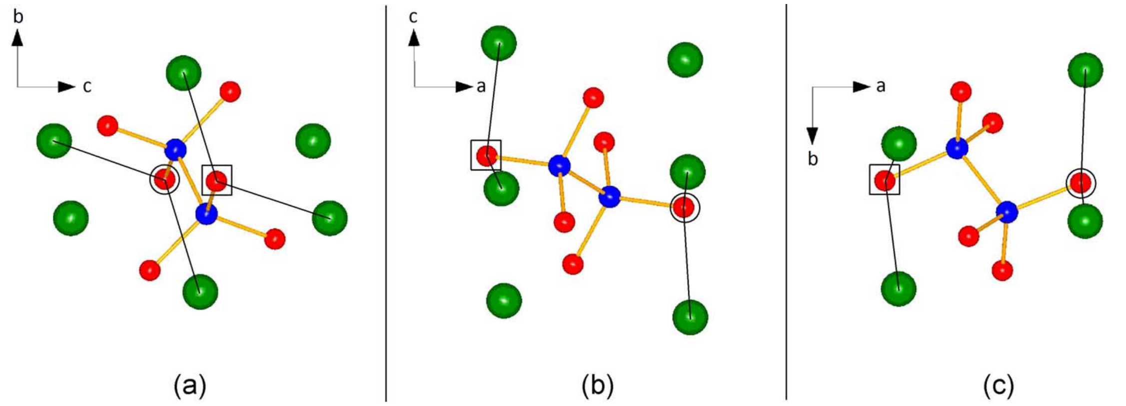

(a) (b) (c)

Figure 33. Possible locations for the sulfur vacancy in SPS. One location is outlined with a square and the other is outlined with a circle. Solid black lines are drawn from each location to their nearest-neighbor tin cations. A hypodiphosphate unit as viewed along the (a) a, (b) b, and (c) c directions is shown with its six nearest neighbor tin cations. Phosphorus cations are blue, tin cations are green, and sulfur anions are red.

VII. Summary and Conclusion

Observations of hyperfine interactions were used to further characterize or identify point defects in three wide-band-gap semiconductors of particular commercial and/or military importance. These wide-band-gap semiconductors are zinc oxide, rutile titanium dioxide, and stannous hexathiohypodiphosphate (SPS). The neutral nitrogen acceptor in zinc oxide was further characterized while the silicon interstitial impurity in rutile titanium dioxide and the singly ionized sulfur vacancy in SPS were identified.

The neutral nitrogen acceptor in zinc oxide was further characterized through the observation of ^{67}Zn hyperfine interactions in the electron paramagnetic resonance spectrum. A study of the angular dependence resulted in ^{67}Zn hyperfine interaction parameters for axial and basal zinc neighbors of the nitrogen substitutional impurity. These ^{67}Zn hyperfine interaction parameters along with the ^{14}N hyperfine interaction parameters provide more information about the physical and electronic structure of the defect. The principal-axis directions of the basal ^{67}Zn hyperfine interaction matix suggest that the nitrogen relaxes away from the axial zinc neighbor and into the plane of the basal zinc neighbors. A better understanding of the electronic wave function provided by the data in this dissertation is expected to aid in the further development or validation of density functional theory models for this important acceptor in zinc oxide.

The silicon interstitial impurity in titanium dioxide was identified through the observation of ^{47}Ti, ^{49}Ti, and ^{29}Si hyperfine interactions in the electron paramagnetic resonance spectrum. A study of the angular dependence resulted in g parameters and two sets of ^{29}Si hyperfine interaction parameters. The hyperfine interaction parameters suggest that the single unpaired electron is tightly bound to two silicon ions. A pulse anneal experiment was performed to determine the thermal stability of paramagnetic defects formed after exposure to near-band-edge light. A sample was reduced by heating in flowing nitrogen to determine the change in charge state between the non-paramagnetic and paramagnetic states of this silicon-related defect.

These experiments suggest that the silicon-related defect is likely a deep donor. The ^{47}Ti and ^{49}Ti hyperfine interactions along with the known crystal structure suggest that one silicon is located at a titanium site and the other is located at a neighboring tetrahedral interstitial site. The distance between the two silicons is very close to the bond length between two silicon atoms in acyclic disilene molecules, suggesting that the silicons may share a double bond. This will have to be confirmed by other experimental methods or through advanced density functional theory modeling.

The singly ionized sulfur vacancy in SPS was identified through the observation of ^{117}Sn, ^{119}Sn, and ^{31}P hyperfine interactions in the electron paramagnetic resonance spectrum. A study of the angular dependence resulted in two sets of ^{117}Sn and ^{119}Sn hyperfine interaction parameters and two sets of ^{31}P hyperfine interaction parameters. The hyperfine interaction parameters suggest that the single unpaired electron wave function is highly diffuse. These data along with the known crystal structure suggest that the defect in its paramagnetic state is a singly ionized sulfur vacancy.

Suggestions for future work follow from the research described in this dissertation. Hyperfine interactions associated with the neighboring ^{67}Zn nuclei should be investigated for the nitrogen molecule in zinc oxide [54]. This effort will complement the present study of ^{67}Zn hyperfine iterations for the isolated nitrogen acceptor in zinc oxide. The silicon interstitial impurity in rutile titanium dioxide needs to be further studied using infrared absorption techniques. The silicon interstitial impurity is expected to give rise to a local vibrational mode in the midinfrared region. This will provide further evidence that the silicon atoms form a bond as described in the proposed model. From here, annealing additional samples at high temperature will determine dissociation energies. Future work in SPS will involve obtaining additional samples from our crystal growth partner at the Uzhgorod State University in Ukraine. A portion of these samples will be annealed in a vacuum to enhance the concentration of sulfur vacancies while others will be annealed in a sulfur atmosphere to eliminate sulfur vacancies. Verifying this ability to modify the concentration of sulfur vacancies in a given sample will allow device engineers to optimize the photorefractive behavior of the crystals.

Electron paramagnetic resonance spectroscopy is an excellent technique for determining the physical and electronic structure of point defects in semiconductors and insulators as long as the defects are paramagnetic and have an appropriate spin-lattice relaxation time. This technique becomes even more powerful if hyperfine interactions are present or when coupled with other spectroscopic techniques. It is a necessary component in any robust materials-characterization capability that guides materials scientists, crystal growers, or systems designers and engineers towards the development of mission critical components and systems.

Appendix A. Angular Momentum and Angular Momentum Operators

For classical mechanical systems [73], angular momentum of a particle is defined as

$$\mathbf{L} = \mathbf{r} \times \mathbf{p}, \tag{70}$$

where $\mathbf{r}$ is the position vector from a specified origin, and $\mathbf{p}$ is the momentum vector. For a system of particles, the total angular momentum is

$$\mathbf{J} = \sum_i \mathbf{r}_i \times \mathbf{p}_i, \tag{71}$$

and the center of mass is defined as

$$\mathbf{R} = \frac{1}{M} \sum_i m_i \mathbf{r}_i \tag{72}$$

where M is the total mass of the particles, and m is the mass of a particle. The position vector of a particle can be defined as the sum of a position vector in the center of mass frame and the position vector of the center of mass,

$$\mathbf{r} = \mathbf{r}' + \mathbf{R} \tag{73}$$

where $\mathbf{r}'$ is the position vector in the center of mass frame. Equation (73) is substituted into Equation (71) to get

$$\mathbf{J} = \sum_i (\mathbf{r}'_i + \mathbf{R}) \times \mathbf{p}_i. \tag{74}$$

Expanding this equation and taking

$$\mathbf{p} = m\frac{d\mathbf{r}}{dt} = m\frac{d}{dt}\left(\mathbf{r}' + \mathbf{R}\right) \tag{75}$$

results in

$$\mathbf{J} = \sum_i \mathbf{r}'_i \times m_i \frac{d\mathbf{r}'_i}{dt} + \sum_i m_i \mathbf{r}'_i \times \frac{d\mathbf{R}}{dt} + \mathbf{R} \times \frac{d}{dt} \sum_i m_i \mathbf{r}'_i + \mathbf{R} \times M\frac{d\mathbf{R}}{dt}. \tag{76}$$

The first term is the sum of the angular momenta of each particle in the center of mass frame. The second and third terms are null vectors, since

$$\frac{1}{M}\sum_i m_i \mathbf{r'}_i \tag{77}$$

is the position of the center of mass in the center of mass frame. The fourth term is the angular momentum of the center of mass. This equation is generalized by grouping particles (i) into multiple centers of mass (j) such that

$$\mathbf{J} = \sum_j \left(\sum_i \mathbf{r'}_{ij} \times m_{ij} \frac{d\mathbf{r'}_{ij}}{dt} \right) + \sum_j \left(\mathbf{R}_j \times M_j \frac{d\mathbf{R}_j}{dt} \right). \tag{78}$$

With this equation, the total angular momentum is viewed as the sum of internal angular momenta from the first term and the sum of external angular momenta around a specified origin from the second term.

For quantum mechanical systems [74], the classical definition defines relations among a set of position and momentum operators,

$$\hat{\mathbf{J}} = \hat{\mathbf{R}} \times \hat{\mathbf{P}}. \tag{79}$$

For this expression to be of use, it is broken up into its component parts,

$$\begin{aligned} \hat{J}_x &= \hat{R}_y \hat{P}_z - \hat{R}_z \hat{P}_y, \\ \hat{J}_y &= \hat{R}_z \hat{P}_x - \hat{R}_x \hat{P}_z, \text{ and} \\ \hat{J}_z &= \hat{R}_x \hat{P}_y - \hat{R}_y \hat{P}_x. \end{aligned} \tag{80}$$

These operators represent measurements of Cartesian components of an angular momentum. Another useful operator is one that represents a measurement of the magnitude of the angular momentum,

$$\hat{J}^2 = \hat{\mathbf{J}} \cdot \hat{\mathbf{J}} = \hat{J}_x^2 + \hat{J}_y^2 + \hat{J}_z^2. \tag{81}$$

With the canonical commutation relations,

$$[\hat{R}_i, \hat{P}_j] = i\hbar\delta_{ij}, \quad [\hat{R}_i, \hat{R}_j] = 0, \quad \text{and} \quad [\hat{P}_i, \hat{P}_j] = 0 \quad \text{where} \quad i, j \in \{x, y, z\}, \tag{82}$$

the angular momentum operators have the following commutation relations.

$$\begin{aligned} &[\hat{J}_x, \hat{J}_y] = i\hbar\hat{J}_z, \\ &[\hat{J}_y, \hat{J}_z] = i\hbar\hat{J}_x, \\ &[\hat{J}_z, \hat{J}_x] = i\hbar\hat{J}_y, \quad \text{and} \\ &[\hat{J}^2, \hat{J}_i] = 0 \quad \text{where} \quad i \in \{x, y, z\}. \end{aligned} \tag{83}$$

These relations indicate that the total angular momentum operator shares eigenstates with each of its component operators and that only one component of the angular momentum can be simultaneously measured with the total angular momentum. Traditionally, the z component is chosen as the component to measure simultaneously with the total angular momentum, and its operator is called an angular momentum projection operator. The focus now is to solve the following eigenvalue equations.

$$\hat{J}^2 \left|n_j, n_z\right\rangle = \lambda_j \left|n_j, n_z\right\rangle, \quad \text{and} \quad \hat{J}_z \left|n_j, n_z\right\rangle = \lambda_z \left|n_j, n_z\right\rangle. \tag{84}$$

This is accomplished by introducing the raising and lowering operators,

$$\hat{J}_+ = \hat{J}_x + i\hat{J}_y, \quad \text{and} \quad \hat{J}_- = \hat{J}_x - i\hat{J}_y, \tag{85}$$

and analyzing the following commutation relationships.

$$\begin{aligned} &[\hat{J}_z, \hat{J}_+] = \hbar\hat{J}_+, \\ &[\hat{J}_z, \hat{J}_-] = -\hbar\hat{J}_-, \quad \text{and} \\ &[\hat{J}^2, \hat{J}_i] = 0 \quad \text{where} \quad i \in \{+, -\}. \end{aligned} \tag{86}$$

The analysis [74] gives the following results.

$$\begin{aligned}
\hat{J}^2 \left|J, m_J\right\rangle &= \hbar^2 J(J+1) \left|J, m_J\right\rangle , \\
\hat{J}_z \left|J, m_J\right\rangle &= \hbar m_J \left|J, m_J\right\rangle , \\
\hat{J}_+ \left|J, m_J\right\rangle &= \hbar\sqrt{J(J+1) - m_J(m_J+1)} \left|J, m_J+1\right\rangle , \quad \text{and} \\
\hat{J}_- \left|J, m_J\right\rangle &= \hbar\sqrt{J(J+1) - m_J(m_J-1)} \left|J, m_J-1\right\rangle
\end{aligned} \tag{87}$$

where $J \in \left\{0, \frac{1}{2}, 1, \frac{3}{2}, \dots\right\}$ is the angular momentum quantum number and $m_J \in \{-J, -J+1, \dots, J-1, J\}$ is the angular momentum projection quantum number.

There are two flavors of angular momentum in quantum mechanical systems. The first is orbital angular momentum, and is analogous to classical angular momentum. This angular momentum is typically annotated in quantum mechanics by **L**. The second is spin angular momentum, and has no classical analogue. It is an intrinsic property of a particle. This angular momentum is typically annotated in quantum mechanics by **S** for an elementary particle and by **I** for a nucleus. Since angular momentum can be seen as a sum of internal and external angular momenta, the total angular momentum is annotated in quantum mechanics by **J** such that

$$\mathbf{J} = \sum_i \mathbf{L}_i + \sum_j \mathbf{S}_j . \tag{88}$$

Since all of the angular momentum operators have a common factor of $\hbar$, it is customary to place angular momentum operators in terms of $\hbar$ such that

$$\hat{\mathbf{J}} \to \hbar \hat{\mathbf{J}} . \tag{89}$$

Appendix B. Crystal Structure of Zinc Oxide

Zinc oxide is a binary metal oxide composed of equal parts zinc and oxygen by atomic composition, and has a hexagonal structure with four basis sites as shown in Figure 34. Hexagonal structures are commonly defined by three coplanar vectors $(\vec{a_1}, \vec{a_2}, \vec{a_3})$ of length a that are separated from each other by 120°, and a vector $(\vec{c})$ of length c that is normal to these coplanar vectors. The plane formed by the coplanar vectors is called the basal plane, and the axis formed by the normal vector is called the c-axis. For zinc oxide, the value of a is 3.250 Å, and the value of c is 5.207 Å [75]. Two of the basis sites are composed of zinc cations, and form a hexagonal quasi-close-pack structure with one basis site at the origin and the other at

$$\frac{1}{3}\vec{a}_x + \frac{2}{3}\vec{a}_y + \frac{1}{2}\vec{c}, \quad \text{where} \quad x, y \in \{1, 2, 3\}, \quad \text{and} \quad x \neq y. \tag{90}$$

A hexagonal close-pack structure has $c/a = 2\sqrt{6}/3 \approx 1.633$, but for zinc oxide $c/a \approx 1.602$. The other two basis sites form the same hexagonal structure except they are composed of oxygen anions that are displaced along the c-axis by $0.3825c = 1.992$ Å [75]. In this structure, the zinc cations are coordinated with four oxygen anions and vice versa forming slightly deformed tetrahedra. A hexagonal close-pack structure forms regular tetrahedra. Since each atom is assigned to two basis sites, there are two sets of tetrahedra that differ by a rotation of 180° in the basal plane. The central atom is coordinated with an atom along the c-axis and three atoms that form a basal plane. The bond angle between the c-axis atom and each of the basal plane atoms is approximately 108° while the bond angle between the basal plane atoms is approximately 110°. A hexagonal close-pack structure has bond angles of approximately 109°. The bond length between the central atom and each basal plane atom is 1.974 Å which is slightly shorter than the bond length along the c-axis.

Hexagonal quasi-close-pack structures are composed of tetrahedral and octahedral interstitial sites as shown in Figure 35. Tetrahedral sites are located a distance

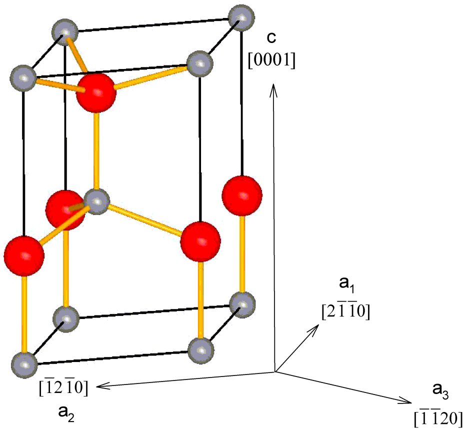

Figure 34. A unit cell of zinc oxide with the zinc nuclei colored gray and the oxygen nuclei colored red.

of

$$\frac{3c^2 + 4a^2}{12c} \tag{91}$$

above and below (along the c-axis) an atom. The four surrounding atoms form the vertices of a deformed regular tetrahedron and are equidistant from the interstitial site. This distance is 1.978 Å in zinc oxide. Three of the surrounding atoms form an equilateral triangle of edge a that is coplanar with the basal plane, and the other site forms a line with the center of this triangle that is collinear with the c-axis. Depending on the c/a ratio, the tetrahedron is deformed along the c-axis by varying the spacing between the basal triangle and the other vertex. Since the c/a ratio for zinc oxide is close to $2\sqrt{6}/3$, the tetrahedra are nearly regular with edge a. With this information, zinc oxide is thought of as a hexagonal close-pack lattice of zinc atoms with half of the tetrahedral sites occupied by oxygen atoms and vice versa. Octahedral sites are located a distance of $c/2$ above and below (along the c-axis) close-pack voids in the unit cell. The six surrounding lattice sites form the vertices of a deformed regular octahedron and are equidistant from the interstitial site by a distance of

$$\frac{1}{4}\sqrt{\frac{16a^2 + 3c^2}{3}}. \tag{92}$$

This distance is 2.284 Å in zinc oxide. Three of the surrounding lattice sites form an equilateral triangle of edge a that is coplanar with the basal plane, and the other three form another equilateral triangle of edge a that is coplanar with the basal plane and is rotated 60° from the other triangle. The line connecting the centers of these equilateral triangles is collinear with the c-axis. Depending on the c/a ratio, the octahedron is deformed along the c-axis by varying the spacing between these two equilateral triangles. Since the c/a ratio for zinc oxide is close to $2\sqrt{6}/3$, the octahedra formed by this lattice are nearly regular with edge a.

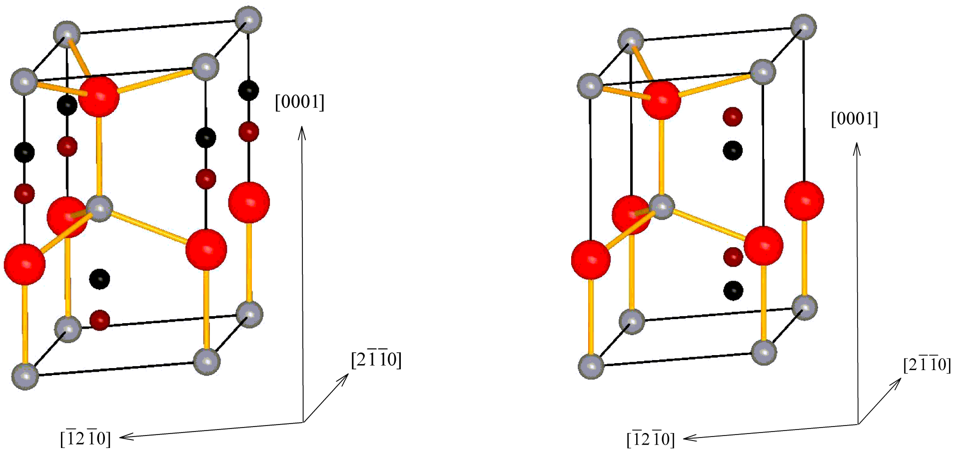

(a) (b)

Figure 35. Unit cells of zinc oxide showing (a) tetrahedral and (b) octahedral interstitial sites. The zinc nuclei are colored gray and the oxygen nuclei are colored red. Interstitial sites surrounded by zinc nuclei are colored in dark red, and sites surrounded by oxygen nuclei are colored in black.

Appendix C. Crystal Structure of Titanium Dioxide

Titanium dioxide is a binary metal oxide composed of one part titanium and two parts oxygen by atomic composition. Anatase, bookite, and rutile are the three polymorphs of titanium dioxide that are stable at standard temperature and pressure. Rutile is the most common naturally occurring and synthetically derived polymorph and is the form of titanium dioxide studied in this dissertation. It has a tetragonal structure with six basis sites as shown in Figure 36. Tetragonal structures are commonly defined by three orthogonal vectors. Two of the vectors ($\vec{a}_1$,$\vec{a}_2$) have length a and one vector ($\vec{c}$) has length c. The plane formed by the vectors of length a is called the basal plane, and the axis formed by the vector of length c is called the c-axis. For titanium dioxide, the value of a is 4.594 Å, and the value of c is 2.959 Å with $c/a = 0.6441$ [76]. Two of the basis sites are composed of titanium cations, and are located at the origin and

$$\frac{1}{2}\vec{a}_1 + \frac{1}{2}\vec{a}_2 + \frac{1}{2}\vec{c}. \tag{93}$$

Four of the basis sites are composed of oxygen anions, and are located at

$$\begin{aligned} u\vec{a}_1 + u\vec{a}_2, \\ (1-u)\vec{a}_1 + (1-u)\vec{a}_2, \\ \left(\frac{1}{2}+u\right)\vec{a}_1 + \left(\frac{1}{2}-u\right)\vec{a}_2 + \frac{1}{2}\vec{c}, \quad \text{and} \\ \left(\frac{1}{2}-u\right)\vec{a}_1 + \left(\frac{1}{2}+u\right)\vec{a}_2 + \frac{1}{2}\vec{c}. \end{aligned} \tag{94}$$

The value of u is 0.306 [76]. The titanium cations are coordinated with six oxygen anions forming a slightly deformed regular octahedron, and the oxygen anions are coordinated with three titanium cations with all four atoms in a $\{110\}$ plane. The octahedron is regular when $u = 1 - \sqrt{2}/2 \approx 0.2929$ and $c/a = 2u \approx 0.5858$. The octahedron is defined by four oxygen anions forming a rectangle in a $\{110\}$ plane, and two oxygen anions forming an axis normal to the rectangle and intersecting the center. Since each titanium cation is assigned to two basis sites, there are two sets of octahedra that differ by a rotation of 90° in the basal plane. The bond length between the titanium cation and the planar oxygen anions is 1.944 Å, and between the titanium cation and the axial oxygen anions is 1.988 Å.

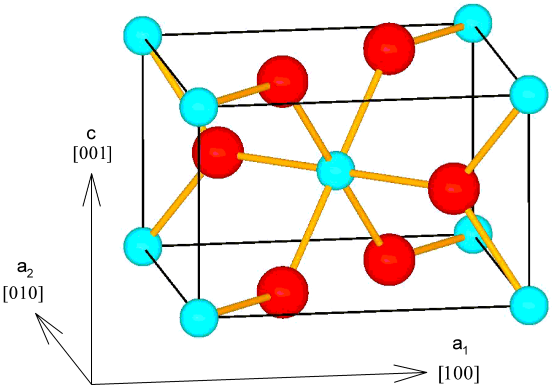

Figure 36. A unit cell of titanium dioxide with the titanium nuclei colored turquoise and the oxygen nuclei colored red.

Titanium dioxide is composed of tetrahedral and octahedral interstitial sites as shown in Figure 37. Tetrahedral sites are located at

$$\begin{aligned} v\vec{a}_1 + v\vec{a}_2 + \frac{1}{2}\vec{c}, \\ (1-v)\vec{a}_1 + (1-v)\vec{a}_2 + \frac{1}{2}\vec{c}, \\ \left(\frac{1}{2}+v\right)\vec{a}_1 + \left(\frac{1}{2}-v\right)\vec{a}_2, \quad \text{and} \\ \left(\frac{1}{2}-v\right)\vec{a}_1 + \left(\frac{1}{2}+v\right)\vec{a}_2, \end{aligned} \tag{95}$$

where

$$v = \frac{1}{2} + \frac{\left(\frac{c}{a}\right)^2 - 2}{16u}. \tag{96}$$

The value of v is 0.176. This site is surrounded by four equidistant oxygen anions which form the vertices of a slightly deformed regular tetrahedron. Two of the oxygen anions form an axis parallel to the c-axis and the other two form an axis parallel to a $\langle 110 \rangle$ direction. The distance to the oxygen anions is 1.703 Å in rutile. This site is also surrounded by three titanium cations which are contained within a $\{110\}$ plane along with the interstitial site. Two of the titanium cations form an axis parallel to the c axis and the other is displaced from the interstitial site along a $\langle 110 \rangle$ direction. The distance to the c axis titanium cations is 1.871 Å, and to the other is 2.104 Å. Octahedral sites are located at

$$\begin{aligned} &\frac{1}{2}(\vec{a}_1 + \vec{c}), \quad \text{and} \\ &\frac{1}{2}(\vec{a}_2 + \vec{c}). \end{aligned} \tag{97}$$

This site is surrounded by six oxygen anions and six titanium cations with each set of atoms forming the vertices of a slightly deformed regular octahedron. These octahedra are similar to the octahedra formed by the nearest-neighbor oxygen anions around the titanium cations, in that they are defined by four atoms forming a rectangle which is perpendicular to an axis formed by the other two atoms and intersecting the center. The oxygen rectangle forms a $\{2, \frac{1-2u}{u}, 0\}$ plane, and the titanium rectangle forms a $\{100\}$ plane. In rutile, the distance to the axial oxygen anions is 1.665 Å, to the planar oxygen anions is 2.227 Å, to the axial titanium cations is 2.297 Å, and to the planar titanium cations is 2.732 Å.

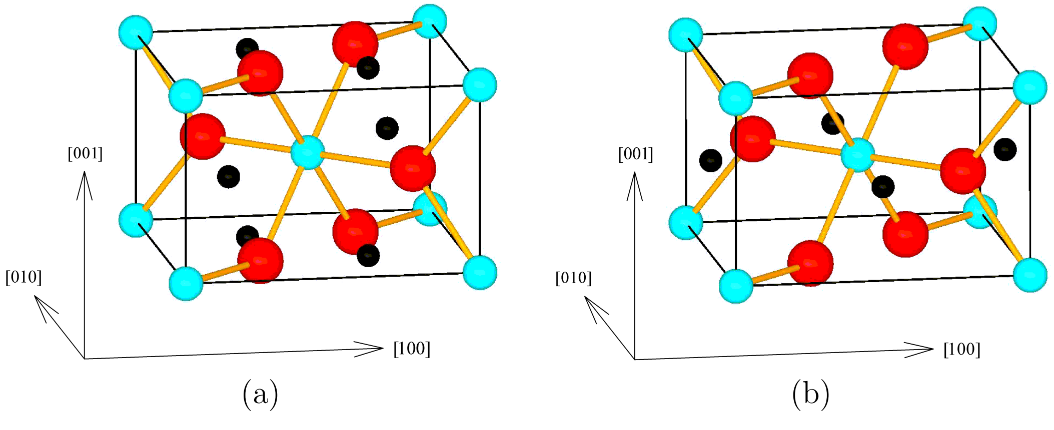

Figure 37. Unit cells of titanium dioxide showing (a) tetrahedral and (b) octahedral interstitial sites. The titanium nuclei are colored turquoise, the oxygen nuclei are colored red, and the interstitial sites are colored black.

Stannous hexathiohypodiphosphate (SPS) is a metal thiophosphate composed of two parts tin, two parts phosphorus, and six parts sulfur by atomic composition. The tin cations have an effective charge state of 2+ while the thiophosphate anions have an effective charge state of 4−. The prototype for the thiophosphate anion is hypodiphosphate. This anion is composed of two phosphorus cations that share a single bond. Each of the phophorus cations have an effective charge state of 4+. Each phosphorus cation also shares single bonds with three chalcogen anions that have an effective charge state of 2−. In the case of hexathiohypodiphosphate, all of the chalcogen anions are sulfur anions. Each set of three sulfur anions roughly forms an equilateral triangle. The plane formed by each triangle is roughly perpendicular to the axis formed by the two phosphorus cations. This axis roughly intersects the center of each triangle. The triangles are rotated from one another by a 180° rotation along this axis. Each set of three sulfur anions is at the periphery of the hypodiphosphate anion at roughly the same distance from their nearest neighbor phosphorus cations. Each hexathiohypodiphosphate anion is surrounded by six tin cations that form a highly distorted regular octahedron as seen in Figure 38.

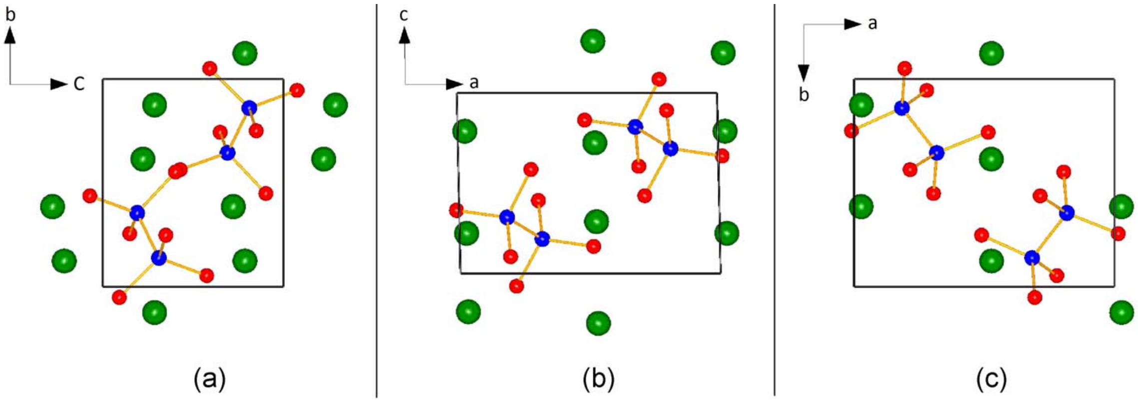

Figure 38. The crystal structure of stannous hexathiohypodiphosphate, showing two hexathiohypodiphosphate anions and their six nearest-neighbor tin cations as viewed along the (a) *a*, (b) *b*, and (c) *c* directions. Phosphorus cations are blue, tin cations are green, and sulfur anions are red. The box outlined in black is a unit cell.

The crystal structure is monoclinic with twenty basis sites as listed in Table 7 [72]. Monoclinic structures are commonly defined by three vectors. The vector $\vec{b}$ is orthogonal to vectors $\vec{a}$ and $\vec{c}$. Vectors $\vec{a}$ and $\vec{c}$ are not orthogonal with an angle of separation β. For SPS the magnitude of vector $\vec{a}$ is 9.378 Å, vector $\vec{b}$ is 7.488 Å, and vector $\vec{c}$ is 6.513 Å. The angle β is 91.15° [72].

Table 7. Basis for the crystal structure of SPS in terms of the lattice vectors [72]. The additional 10 basis sites are found by adding $\frac{1}{2}$ to a and c, and multiplying b by -1.

Element	a	b	c
Sn	0.5270	0.3856	0.7224
Sn	0.0279	0.1245	0.7870
P	0.6836	0.8608	0.8108
P	0.8174	0.6447	0.6908
S	0.4898	0.7511	0.8491
S	0.7788	0.9462	0.0750
S	0.6942	0.0517	0.5921
S	0.0149	0.7437	0.6497
S	0.7147	0.5633	0.4288
S	0.8050	0.4480	0.9025

The angle theta is from the c-axis to the the $[10\bar{1}0]$ direction. The angle phi is from the $[10\bar{1}0]$ direction to the $[2\bar{1}\bar{1}0]$ direction. Calculations use a Plank's constant value of $6.62606957 \times 10^{-34}$ Js [32], a Bohr magneton value of $9.27400968 \times 10^{-24}$ J/T [32], and a g value for the MgO:Cr signal of 1.9800 [38]. The corrected data in bold in the basal zinc table were corrected using the MgO:Cr calibration data in the axial zinc table, since these data were taken with the same experimental setup.

Frequency(MgO:Cr)	9.402031E+009	Hz
Field(MgO:Cr)	0.3392931	T
Correction Factor	0.999930711	
Defect	Basal Zinc	

Frequency (GHz)	Field (G)	Corrected Field (mT)	Theta (Degrees)	Phi (Degrees)
9.394845	3397.497	339.726	90	0
9.394845	3400.837	340.060	90	0
9.394845	3404.281	340.405	90	0
9.394845	3401.426	340.119	90	240,120
9.394845	3404.701	340.447	90	240,120
9.394976	3397.609	339.737	90	5
9.394976	3400.854	340.062	90	5,125
9.394976	3404.188	340.395	90	5,125
9.394976	3401.933	340.170	90	245
9.394976	3404.981	340.475	90	245
9.394853	3397.617	339.738	90	10
9.394853	3400.918	340.068	90	10
9.394853	3404.330	340.409	90	10
9.394853	3402.200	340.196	90	250
9.394853	3405.535	340.530	90	250
9.394853	3400.265	340.003	90	130
9.394853	3403.512	340.328	90	130
9.394948	3397.867	339.763	90	15
9.394948	3401.140	340.090	90	15
9.394948	3404.542	340.431	90	15
9.394948	3402.576	340.234	90	255
9.394948	3405.755	340.552	90	255
9.394948	3399.860	339.962	90	135
9.394948	3403.135	340.290	90	135
9.394895	3398.073	339.784	90	20
9.394895	3401.349	340.111	90	20
9.394895	3402.685	340.245	90	260,140
9.394895	3406.029	340.579	90	260
9.394895	3399.413	339.918	90	140
9.394876	3398.419	339.818	90	25
9.394876	3401.655	340.142	90	25
9.394876	3402.962	340.273	90	265
9.394876	3398.975	339.874	90	145
9.394876	3402.277	340.204	90	145
9.394868	3398.641	339.841	90	30,150
9.394868	3401.885	340.165	90	30,150
9.394868	3402.866	340.263	90	270
9.397276	3320.726	**331.990**	0	0
9.397276	3327.254	**332.643**	0	0
9.397276	3333.549	**333.272**	0	0

Frequency(MgO:Cr)	9.397601E+009 Hz
Field(MgO:Cr)	0.3391937 T
Correction Factor	0.999752459
Defect	Axial Zinc

Frequency (GHz)	Field (G)	Corrected Field (mT)	Theta (Degrees)	Phi (Degrees)
9.397276	3304.348	330.353	0	0
9.397276	3317.319	331.650	0	0
9.397276	3330.418	332.959	0	0
9.397301	3306.702	330.588	10	0
9.397301	3319.553	331.873	10	0
9.397301	3332.499	333.167	10	0
9.397409	3313.662	331.284	20	0
9.397409	3326.092	332.527	20	0
9.397409	3338.522	333.770	20	0
9.397475	3324.812	332.399	30	0
9.397475	3336.970	333.614	30	0
9.397475	3347.962	334.713	30	0
9.397504	3339.088	333.826	40	0
9.397504	3349.683	334.885	40	0

Frequency(MgO:Cr)	9.402031E+009 Hz
Field(MgO:Cr)	0.3392931 T
Correction Factor	0.999930711
Defect	Nitrogen

Frequency (GHz)	Field (G)	Corrected Field (mT)	Theta (Degrees)	Phi (Degrees)
9.394845	3415.959	341.572	90	0
9.394845	3419.242	341.901	90	0
9.394845	3422.672	342.243	90	0
9.394976	3416.012	341.578	90	5
9.394976	3419.286	341.905	90	5
9.394976	3422.729	342.249	90	5
9.394853	3415.983	341.575	90	10
9.394853	3419.221	341.898	90	10
9.394853	3422.660	342.242	90	10
9.394948	3416.002	341.577	90	15
9.394948	3419.280	341.904	90	15
9.394948	3422.678	342.244	90	15
9.394895	3415.980	341.574	90	20
9.394895	3419.259	341.902	90	20
9.394895	3422.661	342.242	90	20
9.394876	3415.965	341.573	90	25
9.394876	3419.240	341.900	90	25
9.394876	3422.674	342.244	90	25
9.394868	3415.937	341.570	90	30
9.394868	3419.199	341.896	90	30
9.394868	3422.670	342.243	90	30

Frequency(MgO:Cr)	9.397601E+009 Hz
Field(MgO:Cr)	0.3391937 T
Correction Factor	0.999752459
Defect	Nitrogen

Frequency (GHz)	Field (G)	Corrected Field (mT)	Theta (Degrees)	Phi (Degrees)
9.397276	3336.950	333.612	0	0
9.397276	3366.036	336.520	0	0
9.397276	3395.089	339.425	0	0
9.397301	3338.913	333.809	10	0
9.397301	3367.606	336.677	10	0
9.397301	3396.271	339.543	10	0
9.397409	3344.702	334.387	20	0
9.397409	3372.185	337.135	20	0
9.397409	3399.672	339.883	20	0
9.397475	3353.746	335.292	30	0
9.397475	3379.272	337.844	30	0
9.397475	3404.691	340.385	30	0
9.397504	3365.129	336.430	40	0
9.397504	3387.927	338.709	40	0
9.397504	3410.726	340.988	40	0

Appendix F. EPR Spectroscopy Data of the Silicon Interstitial in TiO_2

Frequency data is in GHz unless otherwise stated. The data headings label each line with their assigned position in the spectra. “C” stands for center, “H” stands for high field, “L” stands for low field, “I” stands for inner hyperfine, and “O” stands for outer hyperfine. The data in bold in the (001) data were measured with the Hall probe. The magnetic field measured for the MgO:Cr signal with the Hall probe is 3385.69 G. Calculations use a Plank’s constant value of $6.62606957 \times 10^{-34}$ Js [32], a Bohr magneton value of $9.27400968 \times 10^{-24}$ J/T [32], and a g value for the MgO:Cr signal of 1.9800 [38].

Frequency(MgO:Cr)	9.402556E+009 Hz
Field(MgO:Cr)	3.393261E-001 T
Correction Factor	0.999889296
Plane	(100)

NMR Data (G)	LO	LI	C	HI	HO
[001]	3508.433		3525.953		3542.926
10	3506.284		3525.758		3544.479
20	3502.068		3525.141		3547.371
30	3496.916		3523.994		3550.278
40	3491.890		3523.073		3553.462
50	3486.669		3521.752		3555.992
60	3482.045	3508.717	3520.487	3532.105	3558.232
70	3478.785	3506.909	3519.829	3532.646	3560.227
80	3476.590	3505.710	3519.381	3532.899	3561.630
[100]	3476.059	3505.621	3519.541	3533.363	3562.492
Frequency Data	LO	LI	C	HI	HO
[001]	9.562257	9.562257	9.562257	9.562257	9.562257
10	9.562017	9.562017	9.562017	9.562017	9.562017
20	9.561770	9.561770	9.561770	9.561770	9.561770
30	9.561273	9.561273	9.561273	9.561273	9.561273
40	9.561737	9.561737	9.561737	9.561737	9.561737
50	9.561376	9.561376	9.561376	9.561376	9.561376
60	9.561210	9.561210	9.561210	9.561210	9.561210
70	9.562017	9.562017	9.562017	9.562017	9.562017
80	9.562554	9.562554	9.562554	9.562554	9.562554
[100]	9.563654	9.563654	9.563654	9.563654	9.563654
Corrected (mT)	LO	LI	C	HI	HO
[001]	350.804		352.556		354.253
10	350.590		352.537		354.409
20	350.168		352.475		354.698
30	349.653		352.360		354.988
40	349.150		352.268		355.307
50	348.628		352.136		355.560
60	348.166	350.833	352.010	353.171	355.784
70	347.840	350.652	351.944	353.225	355.983
80	347.621	350.532	351.899	353.251	356.124
[100]	347.567	350.523	351.915	353.297	356.210

Frequency(MgO:Cr) 9.402333E+009 Hz
Field(MgO:Cr) 3.393154E-001 T
Correction Factor 0.999897112
Plane (110)

NMR Data (G)	LLO	LLI	L	LHI	LHO	HLO	H	HHO
[001]	3514.267		3531.744		3548.616	3514.267	3531.744	3548.616
10	3508.647		3530.172		3550.894	3515.604	3533.027	3549.895
20	3496.809		3524.290		3550.926		3535.354	3552.176
30	3483.531		3517.268				3540.450	3557.220
40	3467.080	3494.690	3507.256	3519.767		3528.433	3545.655	3562.267
50	3449.467	3480.596	3495.640	3510.535		3532.866	3549.999	3566.414
60	3436.404	3470.493	3487.267	3503.984	3537.878	3539.208	3556.227	3572.545
70	3425.316	3461.754	3479.925	3498.000	3534.449	3544.452	3561.315	3577.489
80	3418.399	3456.187	3475.160	3494.039	3531.936	3546.724	3564.489	3580.559
[110]	3416.261	3454.603	3473.731	3492.854	3531.255	3549.107	3565.826	3581.900
Frequency Data	LLO	LLI	L	LHI	LHO	HLO	H	HHO
[001]	9.576058	9.576058	9.576058	9.576058	9.576058	9.576058	9.576058	9.576058
10	9.576249	9.576249	9.576249	9.576249	9.576249	9.576249	9.576249	9.576249
20	9.573608	9.573608	9.573608	9.573608	9.573608	9.573608	9.573608	9.573608
30	9.573381	9.573381	9.573381	9.573381	9.573381	9.573381	9.573381	9.573381
40	9.570314	9.570314	9.570314	9.570314	9.570314	9.570314	9.570314	9.570314
50	9.563848	9.563848	9.563848	9.563848	9.563848	9.563848	9.563848	9.563848
60	9.563393	9.563393	9.563393	9.563393	9.563393	9.563586	9.563586	9.563586
70	9.562745	9.562745	9.562745	9.562745	9.562745	9.562565	9.562565	9.562565
80	9.561601	9.561601	9.561601	9.561601	9.561601	9.561910	9.561910	9.561910
[110]	9.562010	9.562010	9.562010	9.562010	9.562010	9.562253	9.562253	9.562253
Corrected (mT)	LLO	LLI	L	LHI	LHO	HLO	H	HHO
[001]	351.391		353.138		354.825	351.391	353.138	354.825
10	350.829		352.981		355.053	351.524	353.266	354.953
20	349.645		352.393		355.056		353.499	355.181
30	348.317		351.691				354.009	355.685
40	346.672	349.433	350.690	351.940		352.807	354.529	356.190
50	344.911	348.024	349.528	351.017		353.250	354.963	356.605
60	343.605	347.014	348.691	350.362	353.751	353.884	355.586	357.218
70	342.496	346.140	347.957	349.764	353.409	354.409	356.095	357.712
80	341.805	345.583	347.480	349.368	353.157	354.636	356.412	358.019
[110]	341.591	345.425	347.337	349.249	353.089	354.874	356.546	358.153

Frequency(MgO:Cr) 9.402456E+009 Hz
Field(MgO:Cr) 3.393235E-001 T
Correction Factor 9.99886323E-001
Plane (001)

NMR Data (G)	LLO	LLI	L	LHI	LHO	HLO	HLI	H	HHI	HHO
[100]	3479.352	3508.867	3522.787	3536.656	3565.785	3479.352	3508.867	3522.787	3536.656	3565.785
5	3467.986	3499.270	3514.440		3560.495	3491.658		3531.805	3544.223	3571.356
10	3459.451	3492.380	3508.502	3524.519	3557.212		3530.230	3541.293	3552.256	3577.538
15	3450.247	3484.429	**3493.640**	3518.215		3514.411	3538.744	**3540.310**	3557.465	3581.149
20	3442.277	3477.758	3495.333	3512.803		3524.532		3555.108		3584.789
25	3433.971	3470.455	3488.628	3506.702	3543.094	3532.324		3559.656		3586.185
30	3428.834	3465.969	3484.545	3503.069	3540.212	3539.260		3563.834		3587.512
35	3424.331	3462.171	3481.093	3500.017	3537.810	3546.702		3568.025		3588.450
40	3421.471	3459.562	3478.733	3497.761	3536.006	3551.375		3569.952		3587.720
[110]	3420.730	3458.968	3478.140	3497.266	3535.614	3553.886		3570.602		3586.723
Frequency Data	LLO	LLI	L	LHI	LHO	HLO	HLI	H	HHI	HHO
[100]	9.571588	9.571588	9.571588	9.571588	9.571588	9.571588	9.571588	9.571588	9.571588	9.571588
5	9.572373	9.572373	9.572373	9.572373	9.572373	9.572373	9.572373	9.572373	9.572373	9.572373
10	9.576465	9.576465	9.576465	9.576465	9.576465	9.576465	9.576465	9.576465	9.576465	9.576465
15	9.575892	9.575892	9.575892	9.575892	9.575892	9.575892	9.575892	9.575892	9.575892	9.575892
20	9.576640	9.576640	9.576640	9.576640	9.576640	9.576563	9.576563	9.576563	9.576563	9.576563
25	9.573460	9.573460	9.573460	9.573460	9.573460	9.573776	9.573776	9.573776	9.573776	9.573776
30	9.573281	9.573281	9.573281	9.573281	9.573281	9.573519	9.573519	9.573519	9.573519	9.573519
35	9.573898	9.573898	9.573898	9.573898	9.573898	9.574006	9.574006	9.574006	9.574006	9.574006
40	9.572913	9.572913	9.572913	9.572913	9.572913	9.573474	9.573474	9.573474	9.573474	9.573474
[110]	9.573179	9.573179	9.573179	9.573179	9.573179	9.573352	9.573352	9.573352	9.573352	9.573352
Corrected (mT)	LLO	LLI	L	LHI	LHO	HLO	HLI	H	HHI	HHO
[100]	347.896	350.847	352.239	353.625	356.538	347.896	350.847	352.239	353.625	356.538
5	346.759	349.887	351.404		356.009	349.126		353.140	354.382	357.095
10	345.906	349.198	350.810	352.412	355.681		352.983	354.089	355.185	357.713
15	344.985	348.403	**350.103**	351.782		351.401	353.834	**354.780**	355.706	358.074
20	344.189	347.736	349.494	351.240		352.413		355.470		358.438
25	343.358	347.006	348.823	350.630	354.269	353.192		355.925		358.578
30	342.844	346.558	348.415	350.267	353.981	353.886		356.343		358.710
35	342.394	346.178	348.070	349.962	353.741	354.630		356.762		358.804
40	342.108	345.917	347.834	349.736	353.560	355.097		356.955		358.731
[110]	342.034	345.857	347.774	349.687	353.521	355.348		357.020		358.632

Appendix G. EPR Spectroscopy Data of the Sulfur Vacancy in $Sn_2P_2S_6$

The angle theta is from the c direction towards the a direction. The angle phi is from the a direction towards the b direction. The columns labeled with a g are the center of the spectrum. The columns labeled with a P and a number are phosphorus hyperfine lines where a lower number indicates a lower field. The columns labeled with Sn and a number are the center of a set of lines associated with a tin hyperfine interaction where a lower number indicates a lower field. The columns labeled with Sn, a number, P, and another number are phosphorus hyperfine lines within a set of hyperfine lines associated with a tin hyperfine interaction where lower numbers indicate a lower field. Calculations use a Plank's constant value of $6.62606957 \times 10^{-34}$ Js [32], a Bohr magneton value of $9.27400968 \times 10^{-24}$ J/T [32], and a g value for the MgO:Cr signal of 1.9800 [38].

		MgO:Cr		
Phi	Theta	Frequency	Field	CF
0	90	9.396915	3391.520	0.999802
90	90	9.395018	3390.923	0.999777
0	0	9.396915	3391.520	0.999802

			Field (G)								
Phi	Theta	Frequency	P1Sn1	P1Sn2	P1	P2	g	P3	P4	P4Sn1	P4Sn2
0	90	9.395968	3547.705	3624.740	3399.930	3406.686	3408.336	3410.137	3416.893	3571.718	3651.589
90	90	9.394360	3693.853	3755.879	3533.108	3540.764	3543.162	3545.711	3553.372	3721.462	3785.130
0	0	9.389794	3661.946	3749.389	3519.458	3526.820	3530.130	3533.123	3540.485	3689.560	3780.042

			Corrected Field (mT)								
Phi	Theta	Frequency	P1Sn1	P1Sn2	P1	P2	g	P3	P4	P4Sn1	P4Sn2
0	90	9.395968	354.700	362.402	339.926	340.601	340.766	340.946	341.622	357.101	365.087
90	90	9.394360	369.303	375.504	353.232	353.997	354.237	354.492	355.258	372.063	378.428
0	0	9.389794	366.122	374.865	351.876	352.612	352.943	353.242	353.979	368.883	377.930

MgO:Cr Frequency 9.39691500E+09 Hz
MgO:Cr Field 3.39152000E-01 T
Correction Factor 0.999802

Lowest Field Phosphorus Hyperfine Line

Phi	Theta	Frequency	Field (G)	Field (mT)
90	30	9.389342	3520.415	351.972
90	40	9.389323	3521.824	352.113
90	50	9.389334	3523.428	352.273
90	60	9.389189	3525.815	352.512

MgO:Cr Frequency 9.39553800E+09 Hz
MgO:Cr Field 3.39106400E-01 T
Correction Factor 0.999790

			Field (G)			Corrected Field (mT)		
Phi	Theta	Frequency	g	Sn1	Sn2	g	Sn1	Sn2
90	90	9.394692	3543.691	3709.305	3769.176	354.295	370.853	376.839
80	90	9.394640	3538.295	3702.896	3762.369	353.755	370.212	376.158
70	90	9.394641	3525.455	3687.856	3752.332	352.472	368.708	375.155
60	90	9.394649	3506.559	3668.131	3733.417	350.582	366.736	373.263
50	90	9.394689	3484.470	3642.244	3710.921	348.374	364.148	371.014
40	90	9.394839	3460.426	3617.015	3688.295	345.970	361.626	368.752
30	90	9.395034	3439.389	3592.969	3668.666	343.867	359.222	366.790
20	90	9.395231	3422.223	3573.808	3652.096	342.151	357.306	365.133
10	90	9.395450	3411.785	3563.976	3643.060	341.107	356.323	364.230
0	90	9.395680	3408.773	3561.173	3642.262	340.806	356.043	364.150
0	80	9.390804	3412.567	3565.763	3638.433	341.185	356.502	363.767
0	70	9.390733	3424.000	3576.775	3647.852	342.328	357.602	364.709
0	60	9.390695	3441.224	3592.399	3663.080	344.050	359.165	366.231
0	50	9.390732	3461.428	3612.801	3681.474	346.070	361.204	368.070
0	40	9.390837	3482.982	3633.351	3704.444	348.225	363.259	370.367
0	30	9.390934	3502.629	3651.802	3726.298	350.189	365.104	372.552
0	20	9.391338	3519.184	3666.937	3745.851	351.845	366.617	374.507
0	10	9.391688	3528.910	3675.680	3758.190	352.817	367.491	375.740
0	0	9.392185	3531.125	3677.286	3766.208	353.038	367.651	376.542

Bibliography

1. W. Gerlach and O. Stern, *Das magnetische Moment des Silberatoms*, Zeitschrift für Physik **9**, 353 (1922).
2. G. E. Uhlenbeck and S. Goudsmit, *Ersetzung der Hypothese vom unmechanischen Zwag durch eine Forderung bezüglich des inneren Verhaltens jedes einzelnen Elecktrons*, Naturwissenschaften **13**, 953 (1925).
3. J. K. Böhlke, J. R. de Laeter, P. De Bièvre, H. Hidaka, H. S. Peiser, K. J. R. Rosman, and P. D. P. Taylor, *Isotopic Compositions of the Elements, 2001*, Journal of Physical and Chemical Reference Data **34**, 57 (2005).
4. G. H. Fuller, *Nuclear Spins and Moments*, Journal of Physical and Chemical Reference Data **5**, 835 (1976).
5. G. Breit and I. I. Rabi, *Measurement of Nuclear Spin*, Physical Reveiw **38**, 2082 (1931).
6. I. I. Rabi, J. R. Zacharias, S. Millman, and P. Kusch, *A New Method of Measuring Nuclear Magnetic Moment*, Physical Reveiw **53**, 318 (1938).
7. J. A. Weil, J. R. Bolton, and J. E. Wertz, *Electron Paramagnetic Resonance*, 2nd ed. (John Wiley & Sons, Hoboken, New Jersey, 2007).
8. P. H. Kasai, *Electron Spin Resonance Studies of Donors and Acceptors in ZnO*, Physical Review **130**, 989 (1963).
9. M. Schulz, *ESR Experiments on Ga Donors in ZnO Crystals*, Physica Status Solidi (a) **27**, K5 (1975).
10. C. Gonzalez, D. Block, R. T. Cox, and A. Hervé, *Magnetic Resonance Studies of Shallow Donors in Zinc Oxide*, Journal of Crystal Growth **59**, 357 (1982).
11. C. A. Hampel, ed., *The Encycolpedia of the Chemical Elements* (Reinhold Book Corporation, New York, New York, 1968).

12. Ü. Özgür, Y. I. Alivov, C. Liu, A. Teke, M. A. Reshchikov, S. Doğan, V. Avrutin, S. J. Cho, and H. Morkoç, *A comprehensive review of ZnO materials and devices*, Journal of Applied Physics **98**, 041301 (2005).

13. A. Janotti and C. G. Van de Walle, *Fundamentals of zinc oxide as a semiconductor*, Reports on Progress in Physics **72**, 126501 (2009).

14. V. Srikant and D. R. Clarke, *On the optical band gap of zinc oxide*, Journal of Applied Physics **83**, 5447 (1998).

15. W. Bludau, A. Onton, and W. Heinke, *Temperature dependence of the band gap of silicon*, Journal of Applied Physics **45**, 1846 (1974).

16. S. Pearton, D. Norton, K. Ip, Y. Heo, and T. Steiner, *Recent progress in processing and properties of ZnO*, Progress in Materials Science **50**, 293 (2005).

17. G. H. Reiling and E. B. Hensley, *Fundamental Optical Absorption in Magnesium Oxide*, Physical Review **112**, 1106 (1958).

18. T. Makino, Y. Segawa, M. Kawasaki, A. Ohtomo, R. Shiroki, K. Tamura, T. Yasuda, and H. Koinuma, *Band gap engineering based on* $Mg_xZn_{1-x}O$ *and* $Cd_yZn_{1-y}O$ *ternary alloy films*, Applied Physics Letters **78**, 1237 (2001).

19. F. P. Koffyberg, *Thermoreflectance spectra of CdO: Band gaps and band-population effects*, Physical Review B **13**, 4470 (1976).

20. N. N. Greenwood and A. Earnshaw, *Chemistry of the Elements* (Pergamon Press, Oxford, United Kingdom, 1984).

21. M. Ni, M. K. H. Leung, D. Y. C. Leung, and K. Sumathy, *A review and recent developments in photocatalytic water-splitting using* TiO_2 *for hydrogen production*, Renewable and Sustainable Energy Reveiws **11**, 401 (2007).

22. M. A. Henderson, *A surface science perspective on* TiO_2 *photocatalysis*, Surface Science Reports **66**, 185 (2011).

23. A. K. Rumaiz, B. Ali, A. Ceylan, M. Boggs, T. Beebe, and S. I. Shah, *Experimental studies on vacancy induced ferromagnetism in undoped* TiO_2, Solid State Communications **144**, 334 (2007).

24. S. Zhou, E. Čižmár, K. Potzger, M. Krause, G. Talut, M. Helm, J. Fassbender, S. A. Zvyagin, J. Wosnitza, and H. Schmidt, *Origin of magnetic moments in defective* TiO_2 *single crystals*, Physical Reveiw B **79**, 113201 (2009).

25. K. Szot, M. Rogala, W. Speier, Z. Klusek, A. Besmehn, and R. Waser, TiO_2 *- a prototypical memristive material*, Nanotechnology **22**, 254001 (2011).

26. Z. Yang, D. Choi, S. Kerisit, K. M. Rosso, D. Wang, J. Zhang, G. Graff, and J. Liu, *Nanostructures and lithium electrochemical reactivity of lithium titanites and titanium oxides: A review*, Journal of Power Sources **192**, 588 (2009).

27. K. Z. Rushchanskii, Y. M. Vysochanskii, and D. Strauch, *Ferroelectricity, Nonlinear Dynamics, and Relaxation Effects in Monoclinic* $Sn_2P_2S_6$, Physical Reveiw Letters **99**, 207601 (2007).

28. S. G. Odoulov, A. N. Shumelyuk, U. Hellwig, R. A. Rupp, and A. A. Grabar, *Photorefractive beam coupling in tin hypothiodiphosphate in the near infrared*, Optics Letters **21**, 752 (1996).

29. S. G. Odoulov, A. N. Shumelyuk, U. Hellwig, R. A. Rupp, A. A. Grabar, and I. M. Stoyka, *Photorefraction in tin hypothiodiphosphate in the near infrared*, Journal of the Optical Society of America B **13**, 2352 (1996).

30. S. G. Odoulov, A. N. Shumelyuk, G. A. Brost, and K. M. Magde, *Enhancement of beam coupling in the near infrared for tin hypothiodiphosphate*, Applied Physics Letters **69**, 3665 (1996).

31. J. D. Jackson, *Classical Electrodynamics*, 3rd ed. (John Wiley and Sons, Hoboken, New Jersey, 1999) pp. 184–190.

32. P. J. Mohr, B. N. Taylor, and D. B. Newell, *CODATA Recommended Values of the Fundamental Physical Constants: 2010*, Journal of Physical and Chemical Reference Data **41**, 043109 (2012).

33. E. Fermi, *Über die magnetischen Momente der Atomkerne*, Zeitschrift für Physik **60**, 320 (1930).

34. A. G. Prodell and P. Kusch, *The Hyperfine Structure of Hydrogen and Deuterium*, Physical Review **88**, 184 (1952).

35. J. M. Spaeth, J. R. Niklas, and R. H. Bartram, *Structural Analysis of Point Defects in Solids*, Springer Series in Solid-State Sciences, Vol. 43 (Springer-Verlag, Berlin, Germany, 1992).

36. R. T. Weber, J. Jiang, and D. P. Barr, *EMX User's Manual* (Bruker EPR Division, Billerica, Massachusetts, 1998).

37. S. Yang, *Paramagnetic Resonance Studies of Defects in Titanium Dioxide Crystals*, Ph.D. dissertation, West Virginia University, Morgantown, West Virginia (2010).

38. W. Low, *Paramagnetic Resonance and Optical Absorption Spectra of* Cr^{3+} *in MgO*, Physical Review **105**, 801 (1957).

39. W. E. Carlos, E. R. Glaser, and D. C. Look, *Magnetic resonance studies of ZnO*, Physica B **308-310**, 976 (2001).

40. N. Y. Garces, N. C. Giles, L. E. Halliburton, G. Cantwell, D. B. Eason, D. C. Reynolds, and D. C. Look, *Production of nitrogen acceptors in ZnO by thermal annealing*, Applied Physics Letters **80**, 1334 (2002).

41. D. Pfisterer, J. Sann, D. M. Hofmann, M. Plana, A. Neumann, M. Lerch, and B. K. Meyer, *Incorporation of nitrogen acceptors in ZnO powder*, Physica Status Solidi B **243**, R1 (2006).

42. F. Gallino, C. DiValentin, G. Pacchioni, M. Chiesa, and E. Giamello, *Nitrogen impurity states in polycrystalline ZnO. A combined EPR and theoretical study*, Journal of Materials Chemistry **20**, 689 (2010).

43. S. M. Evans, *Identification and Characterization of Point Defects in Aluminum Nitride and Zinc Oxide Crystals*, Ph.D. dissertation, West Virginia University, Morgantown, West Virginia (2008).

44. J. E. Stehr, D. M. Hofmann, and B. K. Meyer, *Electron paramagnetic resonance and photo-electron paramagnetic resonance investigation on the recharging of the substitutional nitrogen acceptor in ZnO*, Journal of Applied Physics **112**, 103511 (2012).

45. J. L. Lyons, A. Janotti, and C. G. V. de Walle, *Why nitrogen cannot lead to p-type conductivity in ZnO*, Applied Physics Letters **95**, 252105 (2009).

46. S. Lany and A. Zunger, *Generalized Koopmans density functional calculations reveal the deep acceptor state of* N_O *in ZnO*, Physical Review B **81**, 205209 (2010).

47. A. Boonchun and W. R. L. Lambrecht, *Electronic structure of defects and doping in ZnO: Oxygen vacancy and nitrogen doping*, Physica Status Solidi B **250**, 2091 (2013).

48. S. Sakong, J. Gutjahr, and P. Kratzer, *Comparison of density functionals for nitrogen impurities in ZnO*, Journal of Chemical Physics **138**, 234702 (2013).

49. M. C. Tarun, M. Z. Iqbal, and M. D. McCluskey, *Nitrogen is a deep acceptor in ZnO*, AIP Advances **1**, 022105 (2011).

50. S. Lautenschlaeger, S. Eisermann, G. Haas, E. A. Zolnowski, M. N. Hofmann, A. Laufer, M. Pinnisch, B. K. Meyer, M. R. Wagner, J. S. Reparaz, G. Callsen, A. Hoffmann, A. Chernikov, S. Chatterjee, V. Bornwasser, and M. Koch, *Optical signatures of nitrogen acceptors in ZnO*, Physical Review B **85**, 235204 (2012).

51. E. M. Golden, S. M. Evans, L. E. Halliburton, and N. C. Giles, *Neutral nitrogen acceptors in ZnO: The ^{67}Zn hyperfine interactions*, Journal of Applied Physics **115**, 103703 (2014).

52. M. S. Bahramy, M. H. F. Sluiter, and Y. Kawazoe, *First-principles calculations of hyperfine parameters with the all-electron mixed-basis method*, Physical Review B **73**, 045111 (2006).

53. E. D. Hedegard, J. Kongsted, and S. P. A. Sauer, *Optimized Basis Sets for Calculation of Electron Paramagnetic Resonance Hyperfine Coupling Constants: aug-cc-pVTZ-J for the 3d Atoms Sc-Zn*, Journal of Chemical Theory and Computation **7**, 4077 (2011).

54. N. Y. Garces, L. Wang, N. C. Giles, L. E. Halliburton, G. Cantwell, and D. B. Eason, *Molecular nitrogen (N_2^-) acceptors and isolated nitrogen (N^-) acceptors in ZnO crystals*, Journal of Applied Physics **94**, 519 (2003).

55. J. R. Morton and K. F. Preston, *Atomic Parameters for Paramagnetic Resonance Data*, Journal of Magnetic Resonance **30**, 577 (1978).

56. A. T. Brant, N. C. Giles, and L. E. Halliburton, *Insertion of lithium ions into TiO_2 (rutile) crystals: An electron paramagnetic resonance study of the Li-associated Ti^{3+} small polaron*, Journal of Applied Physics **113**, 053712 (2013).

57. H. J. Gerritsen, S. E. Harrison, H. R. Lewis, and J. P. Wittke, *Fine Structure, Hyperfine Structure, and Relaxation Times of Cr^{3+} in TiO_2 (Rutile)*, Physical Reveiw Letters **2**, 153 (1959).

58. H. J. Gerritsen and E. S. Sabisky, *Paramagnetic Resonance of Ni^{2+} and Ni^{3+} in TiO_2*, Physical Review **125**, 1853 (1962).

59. T. C. Ensign, T.-T. Chang, and A. H. Kahn, *Hyperfine and Nuclear Quadrupole Interactions in Copper-Doped TiO_2*, Physical Reveiw **188**, 703 (1969).

60. A. T. Brant, S. Yang, N. C. Giles, M. Z. Iqbal, A. Manivannan, and L. E. Halliburton, *Oxygen vacancies adjacent to* Cu^{2+} *ions in* TiO_2 *(rutile) crystals*, Journal of Applied Physics **109**, 073711 (2011).

61. D. L. Carter and A. Okaya, *Electron Paramagnetic Resonance of* Fe^{3+} *in* TiO_2 *(Rutile)*, Physical Reveiw **118**, 1485 (1960).

62. H. J. Gerritsen and H. R. Lewis, *Paramagnetic Resonance of* V^{4+} *in* TiO_2, Physical Reveiw **119**, 1010 (1960).

63. S. Yang, L. E. Halliburton, A. Manivannan, P. H. Bunton, D. B. Baker, M. Klemm, S. Horn, and A. Fujishima, *Photoinduced electron paramagnetic resonance study of electron traps in* TiO_2 *crystals: Oxygen vacancies and* Ti^{3+} *ions*, Applied Physics Letters **94**, 162114 (2009).

64. A. T. Brant, N. C. Giles, S. Yang, M. A. R. Sarker, S. Watauchi, M. Nagao, I. Tanaka, D. A. Tryk, A. Manivannan, and L. E. Halliburton, *Ground state of the singly ionized oxygen vacancy in rutile* TiO_2, Journal of Applied Physics **114**, 113702 (2013).

65. A. T. Brant, E. M. Golden, N. C. Giles, S. Yang, M. A. R. Sarker, S. Watauchi, M. Nagao, I. Tanaka, D. A. Tryk, A. Manivannan, and L. E. Halliburton, *Triplet ground state of the neural oxygen-vacancy donor in rutile* TiO_2, Physical Review B **89**, 115206 (2014).

66. R. W. G. Wyckoff, *Crystal Structures*, 2nd ed., Vol. 1 (John Wiley & Sons, New York, New York, 1963).

67. M. Kira and T. Iwamoto, *Progress in the Chemistry of Stable Disilenes*, Advances in Organometallic Chemistry **54**, 73 (2006).

68. A. T. Brant, L. E. Halliburton, S. A. Basun, A. A. Grabar, S. G. Odoulov, A. Shumelyuk, N. C. Giles, and D. R. Evans, *Photoinduced EPR study of* Sb^{2+} *ions in photorefractive* $Sn_2P_2S_6$ *crystals*, Physical Reveiw B **86**, 134109 (2012).

69. I. N. Geifman, I. V. Kozlova, U. M. Vysochanski, V. Y. Kofman, and O. A. Mikailo, *Temperature dependence of* Mn^{2+} *EPR in* $Sn_2P_2S_6$ *near the Phase Transition*, Applied Magnetic Resonance **2**, 435 (1991).

70. A. T. Brant, L. E. Halliburton, N. C. Giles, S. A. Basun, A. A. Grabar, and D. R. Evans, *Intrinsic small polarons* (Sn^{3+}) *ions in photorefractive* $Sn_2P_2S_6$ *crystals*, Journal of Physics: Condensed Matter **25**, 205501 (2013).

71. A. Ruediger, O. Schirmer, S. Odoulov, A. Shumelyuk, and A. Grabar, *Studies of light-induced charge transfer in* $Sn_2P_2S_6$ *by combined EPR/optical absorption spectroscopy*, Optical Materials **18**, 123 (2001).

72. G. Dittmar and H. Schäfer, *The Crystal Structure of* $Sn_2P_2S_6$, Zeitschrift für Naturforschung. **29B**, 312 (1974).

73. H. Goldstein, C. Poole, and J. Safko, *Classical Mechanics*, 3rd ed. (Addison Wesley, San Francisco, California, 2002) pp. 8–9.

74. C. Cohen-Tannoudji, B. Diu, and F. Laloë, *Quantum Mechanics*, Vol. 1 (John Wiley & Sons, Singapore, 2005) pp. 643–660.

75. S. C. Abrahams and J. L. Bernstein, *Remeasurement of the Structure of Hexagonal ZnO*, Acta Crystallographica **25B**, 1233 (1969).

76. V. W. H. Baur, *Über die Verfeinerung der Kristallstrukturbestimmung einiger Vertreter des Rutiltyps:* TiO_2, SnO_2, GeO_2 *und* MgF_2, Acta Crystallographica **9**, 515 (1956).

REPORT DOCUMENTATION PAGE

Form Approved
OMB No. 0704-0188

1. REPORT DATE *(DD-MM-YYYY)* 18-09-2014	**2. REPORT TYPE** Dissertation	**3. DATES COVERED** *(From - To)* October 2011 - September 2014

4. TITLE AND SUBTITLE
Hyperfine Interactions in the Electron Paramagnetic Resonance Spectra of Point Defects in Wide-Band-Gap Semiconductors

5a. CONTRACT NUMBER

5b. GRANT NUMBER

5c. PROGRAM ELEMENT NUMBER

6. AUTHOR(S)
Golden, Eric M., Major, USAF

5d. PROJECT NUMBER

5e. TASK NUMBER

5f. WORK UNIT NUMBER

7. PERFORMING ORGANIZATION NAME(S) AND ADDRESS(ES)
Air Force Institute of Technology
Graduate School of Engineering and Management (AFIT/EN)
2950 Hobson Way
Wright-Patterson AFB OH 45433-7765

8. PERFORMING ORGANIZATION REPORT NUMBER
AFIT-ENP-DS-14-S-07

9. SPONSORING/MONITORING AGENCY NAME(S) AND ADDRESS(ES)
Intentionally Left Blank

10. SPONSOR/MONITOR'S ACRONYM(S)

11. SPONSOR/MONITOR'S REPORT NUMBER(S)

12. DISTRIBUTION/AVAILABILITY STATEMENT
Distribution Statement A. Approved for Public Release; Distribution Unlimited

13. SUPPLEMENTARY NOTES
This material is declared a work of the U. S. Government and is not subject to copyright protection in the United States.

14. ABSTRACT

The focus of this research was to acquire definitive experimental data on predominant point defects in three important wide-band-gap semiconductors. Hyperfine interactions in electron paramagnetic resonance spectra were used to characterize the neutral nitrogen acceptor in zinc oxide, to identify a silicon interstitial impurity in titanium dioxide, and to determine the electronic structure of the singly ionized sulfur vacancy in stannous hexathiohypodiphosphate (SPS). Zinc oxide is an electro-optic material with the potential to produce high-performance electronics and also ultraviolet detectors and emitters. Titanium dioxide is an energy-conversion material being developed for hydrogen generation and use as an electrode in lithium-ion batteries. SPS is a high-speed photorefractive material that is being developed for use as a protective element in visible and infrared sensor systems to guard against laser induced damage and/or jamming. Research on the basic properties of these technologically important materials plays a crucial role in the development of advanced optical and electronic systems.

15. SUBJECT TERMS
Electron Paramagnetic Resonance, Zinc Oxide, Titanium Dioxide, Rutile, Stannous Hexathiohypodiphosphate, SPS

16. SECURITY CLASSIFICATION OF:			**17. LIMITATION OF ABSTRACT**	**18. NUMBER OF PAGES**	**19a. NAME OF RESPONSIBLE PERSON**
a. REPORT	**b. ABSTRACT**	**c. THIS PAGE**			Dr. Nancy C. Giles, AFIT/ENP
U	U	U	UU	132	**19b. TELEPHONE NUMBER** *(Include area code)* (937)255-3636x4601 nancy.giles@afit.edu